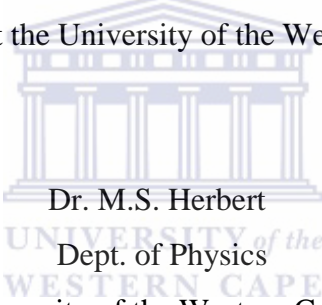# Comparison of neutron fluence spectra measured with NE213 proton recoil spectrometer and NE230 deuteron recoil spectrometer

Vusumuzi Masondo

Thesis presented in fulfillment of the requirements for the degree of Magister Scientiae at the University of the Western Cape.

Supervisor: Dr. M.S. Herbert

Dept. of Physics

University of the Western Cape

Co-supervisor: Dr. M.R. Nchodu

Dept. of Nuclear Physics

iThemba LABS

December 2014

DECLARATION

I, the undersigned, hereby declare that the work contained in this thesis is my own original work and that I have not previously in its entirety or in part submitted it at any university for a degree.

Signature: ………………………………………………………

Date: ………………………………………………………………

KEYWORDS

- Neutron fluence
- NE213
- NE230
- Liquid organic scintillator
- Spectrometer
- Pulse shape discrimination (PSD)
- Response function or Pulse height spectrum
- Response
- Detection efficiency
- Neutron fluence spectra

ABSTRACT

Comparison of neutron fluence spectra measured with NE213 proton recoil spectrometer and NE230 deuteron recoil spectrometer

Vusumuzi Masondo

MSc Thesis, Department of Physics, University of the Western Cape, Private Bag X17, Bellville 7535, South Africa

A (5 cm × 5 cm) cylindrical NE213 liquid organic scintillator and a (2.5 cm × 2.5 cm) cylindrical NE230 liquid organic scintillator were used as spectrometers. A series of measurements was made with both the NE213 and NE230 spectrometers, with the time-of-flight technique used for neutron energy selection. Pulse height spectra for quasi-monoenergetic neutron beams of ~5-64 MeV produced by bombarding either a (1 mm) lithium metal target, or a (10 mm) beryllium target, or a (10 mm) graphite target with 66 MeV proton beam were measured with both spectrometers. Deuteron events identified by pulse shape discrimination were selected for measurements with the NE230 spectrometer while proton events were selected for measurements with the NE213 spectrometer. Response of the scintillator to protons using NE213 and deuterons using NE230 were obtained from the measured pulse height spectra. Detector efficiency of the NE213 spectrometer as a function of neutron energy was determined for n-p elastic scattering. The detector efficiency of the NE230 was determined relative to the well-known efficiency of the NE213 spectrometer, selecting either all or n-d elastic events in the pulse height spectra measured with the NE230 spectrometer. The detection efficiency of the NE230 spectrometer was also determined from the available cross-section for n-d elastic scattering as exploratory work. Neutron fluence spectra could be determined using the appropriate neutron detection efficiency for each spectrometer and were compared with each other. The results showed good comparison and encouragement demonstrating the reliability of neutron fluence spectral measurements with the NE230 spectrometer using the time-of-flight technique.

PREFACE

This thesis presents results for fast neutron measurements using the NE213 spectrometer and the NE230 spectrometer. Experiments for this work were carried at the neutron time-of-flight facility at iThemba LABS in South Africa in August 2000. The main purpose of the experiment was for testing and development of the NE230 spectrometer for measurements inside a water phantom. In air measurements with the NE213 spectrometer and the NE230 spectrometer were ran and served for calibration purposes as highlighted by Herbert [Herbert, 2009]. The experiment was led by Prof F.D. Brooks and was carried in the absence of the author, the data was passed to the author through the permission of Dr. M.S. Herbert (MSc supervisor of the author) who was part of the experiment. Apart from the experimental details and some figures of the experimental details, all analysis of data and results presented in this thesis were carried by the author for the MSc with the permission and guidance of his supervisor. The data analysis was done in part using the computer program GNU available at iThemba LABS and the University of Cape Town Physics Department.
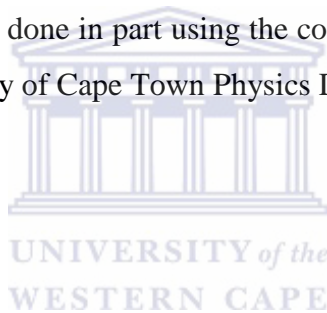
DEDICATION

This work is dedicated to my grandmother who left us to be with the Lord just when her prayers about my life were coming into realization, May her soul rest in peace you will always be in my heart and your ever wise words will serve as my light at all times.

ACKNOWLEDGEMENTS

My friends at home, Simphiwe, Thabo, Bheki, Welcome and Tuis, you guys have been awesome and I know you with me at all times, may God keep you guys.

Most importantly I would like to thank my family, my mother, father and siblings, you have been incredible with your support, love patience although it was not easy and I still hope you will be more patient as there is last mile in this field to travel.

Most importantly I would like to single out my mother, your prayers, confidence in what I do, support, understanding, and the love you have shown I don't think there are words that can fully describe how appreciative I am, may God be with you and keep you and answer all your prayers.

TABLE OF CONTENT

UNIVERSITY *of the*

WESTERN CAPE

LIST OF FIGURES

xiii

LIST OF TABLES

1.   INTRODUCTION

Measurements and calculations of neutron fluence are of interest in both nuclear physics research and applications. The need for neutron fluence measurements arise in areas such as in nuclear reactors where radiation damage is of concern [Thomas, *et al*., 2011] and in materials testing for fusion applications [Peurung, 2000] [Thomas, *et al*., 2011], radiation protection in space [Kinnison, *et al*., 2003], nuclear facilities such as iThemba LABS [Adams, 2010] [Herbert, 2014], and in the atmosphere [Thomas, *et al*., 2011], in calibration of neutron detectors [Herbert, 2014] and in neutron radiotherapy [Alevra, 1999] [Herbert, *et al*., 2007]. Often there is a need to know the neutron fluence energy distribution of a neutron beam, of particular interest in the larger scope of this work, the neutron fluence energy distributions are important in the characterisation of a neutron source in radiotherapy for cancer treatment where the accurate delivery of the dose is essential.

There are various experimental techniques employed in measurements of neutron fluence, namely: recoil spectrometry, methods based on moderation, time-of-flight technique and threshold spectrometry [Alevra, 1999] [Brooks & Klein, 2002]. For neutron fluence measurements and detection of fast neutrons involving time-of-flight technique and recoil spectrometry, organic scintillators have found preference over other detectors (such as inorganic scintillators, etc.). This is due to their excellent pulse shape discrimination capabilities in mixed neutron/gamma fields and their high efficiency for fast neutron counting [Tavernier, 2010] [Karlsson, 1997]. Liquid organic scintillators NE213 and NE230 offer good pulse shape discrimination, good detection efficiency, can be manufactured suitably in size and shape, and are also relatively cheap, thus have been preferred over other organic scintillators such as stilbene and anthracene. In contrast to liquid organic scintillators such as NE213 and NE230, stilbene and anthracene have a disadvantage since they are known to be anisotropic [Leo, 1987], that is, the response is dependent on the orientation of the crystal to radiating particles [Knoll, 2000] [Leo, 1987] [Brooks, 1979].

In liquid organic scintillators secondary charged particles are produced by interactions of neutrons with the detector medium, which can be processed into signals brought about by scintillation resulting from the ionization of charged particles as they stop in the detector medium. The pulse height of the signal together with the available nuclear cross-sections can be used to determine the detector efficiency from which neutron fluence can be determined.

Generally, time-of-flight technique is known to be more accurate for such measurements of fast neutrons in air [Ojaruega, 2009] [Herbert, 2014].

1.1   Previous Work

Measurements and calculations of neutron fluence spectra have been carried out using organic liquid scintillators NE213 and NE230, both in air and in phantom, for examples see references [Adams, *et al*., 2010] [Brooks, *et al*., 2004] [Bohm, *et al*., 1999] [Herbert, 2014] [Taniguchi, *et al*., 2003]. Most of these measurements have been carried out in air [Herbert, 2014] [Brooks, *et al*., 2004] [Makupula, 2003] [Gagnon-Moisan, *et al*., 2012] using NE213 spectrometers and relatively very few measurements and calculations have been carried out in a water phantom, particularly neutron fluence spectra measurements with NE230 spectrometers [Herbert, *et al*., 2007] [Herbert, *et al*., 2014] and Monte Carlo simulations [Benck, *et al*., 2002][Herbert, *et al*., 2007] [Herbert, *et al*., 2014]. For some of the measurements, there have been comparisons with results calculated using Monte Carlo codes, where the source spectrum had been modeled [Bohm, *et al*., 1999], and neutron fluence spectra have been compared with other targets and sources of neutrons [Adams, et al., 2010] [Herbert, 2014] [Gagnon-Moisan, *et al*., 2012] [Taniguchi, et al., 2003]. Calculations using Monte Carlo codes have been able to reproduce experimental results at energies below 20 MeV [Adams, 2010] [Herbert, 2009], this is due to the availability and good knowledge of nuclear reaction cross-sections at this energy range [Herbert, 2014]. At energies greater than 20 MeV the challenge arise with the multiple breakup of carbon, thus cross-sections are either not accurate enough or not well-known, as a result it is challenging to carry out experiments in this range [Adams, 2010] [Herbert, 2009] and experimental results are not well reproduced by means of Monte Carlo simulations [Meigo, 1997].

In air measurements of energy spectra are shown in figure 1.1, (a) and (b) shows neutron fluence spectra of lithium and graphite targets measured by Brooks *et al.* [Brooks, et al., 2004] using stacked liquid scintillators. The experiment was carried out at the neutron time-of-flight facility at iThemba LABS in South Africa. This work was aimed at showing calibration of stacked liquid scintillators (S3N) with pulsed beam and how it can be used for neutron fluence spectra measurements [Brooks, *et al*., 2004]. The neutron fluence spectrum in (a) and (b) were produced by time-of-flight method (histogram) and unfolding the S3N pulse height spectrum (points) [Brooks, *et al*., 2004].
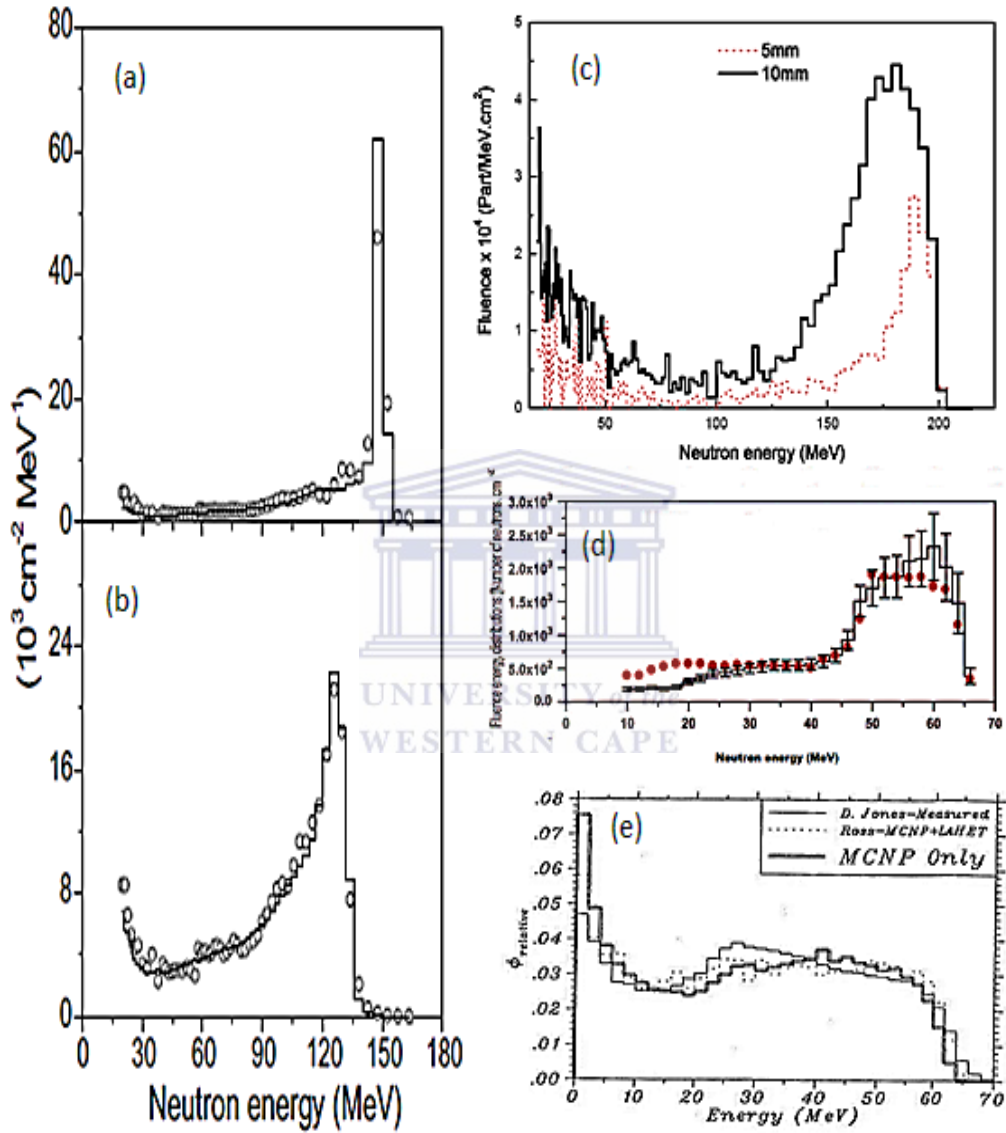
Figure 1. 1: *Neutron fluence spectra of, (a) lithium and (b) graphite targets measured with the stacked liquid scintillator [Brooks, et al., 2004], (c) 5mm and 10mm thick ⁹Be targets simulated using FLUKA [Adams, 2010], (d) 10mm ⁹Be target measured compared to simulated with MCNPX [Herbert, 2014], and (e) comparison of measured results and simulated relative neutron fluence spectra with MCNP+LAHET and MCNP only [Bohm, et al., 1999].*

Figure 1.1 (c) shows the work carried out by Adams, where the effect of target thickness was shown for neutron fluence spectra of ^{9}Be [Adams, 2010], neutron fluence spectra were simulated using FLUKA code, simulating the interaction of 200 MeV proton beam with the ^{9}Be of different thickness. The neutron fluence spectrum for a thicker target (10 mm) was found to have a broader distribution compared to the 5 mm thick ^{9}Be target. A comparison of Monte Carlo calculations and experimental measurements are shown in (d) [Herbert, 2014] and (e) [Bohm, *et al*., 1999]. Both work carried out by Herbert and Bohm *et al.* showed agreement between experiments and simulations, with a small difference arising due to how the proton beam was simulated in (d) where NE213 was used as a spectrometer for fluence spectra measurements and with the difference in (e) being inconclusive since the dimensions of the detector and modeled results were different, thus more work needs to be done to conclude on differences in neutron fluence.

For in-phantom measurements of neutron fluence spectra, as mentioned earlier very few measurements are reported [Benck, et al., 2002], with some of the work on neutron energy spectra reported using NE230 [Herbert, *et al*., 2007] [Herbert, *et al*., 2014] and NE213 [Crout, *et al*., 1989]. One of the challenges with the proton recoil spectrometers such as NE213 for in-phantom (water) measurements, is the difficulty of discriminating between protons from water (when water is used to simulate the human tissue) and those arising from the detector medium [Herbert, 2009].

1.1   Aims and Scope of the Present Work

Both the NE213 and NE230 spectrometers have been used as neutron spectrometers [Herbert, *et al*., 2007] [Zimbal, *et al*., 2006], with NE213 used as a proton recoil spectrometer and NE230 as a deuteron recoil spectrometer. The NE230 spectrometer has an advantage for neutron flence spectral measurements inside a water phantom, because deuteron events may be selected, thus overcoming the challenge of discimination of elastically scattered protons mentioned earlier (refer to section 1.1). In addition the NE230 spectrometer has an advantage over the NE213 spectrometer because deuterons have a shorter range compared to protons at the same energy, thus less particles escapes [Herbert, 2009]. However one of the challenges for measurements with the NE230 spectrometer is the determination of the neutron detection efficiency as a function of neutron energy due to unavailable cross-sections for n-d elastic sccattering.

This work was carried out with an aim to make comparisons between neutron fluence spectra measured with the NE213 (5 cm × 5 cm) and the NE230 (2.5 cm × 2.5 cm) spectrometers. At this stage the objective was to investigate the reliability of the NE230 spectrometer to reproduce results measured with the widely used NE213 spectrometer in air. In addition, this work serves towards the calibration for in water phantom measurements with both the NE213 and the NE230 spectrometers.

Experiments were carried out at the neutron time-of-flight facility at iThemba LABS in South Africa. Neutrons were produced by bombarding either a (1 mm) lithium metal, or a (10 mm) beryllium, and or a (10 mm) graphite target with pulsed beam of 66 MeV protons from the separated sector cyclotron to produce up to ~64 MeV neutrons, the motivation on the choice of these targets is further discussed in section 4.1.1. These measurements were carried out in air using a time-of-flight technique with recoil spectrometry. The data obtained allowed up to 29 neutron energies to be selected (10-66 MeV). The data were used to generate response functions for these particular energies (10-66 MeV) depending on the target. This was done by setting a time window at suitable energies for each target in the offline analysis. Neutron detection efficiency of the NE230 spectrometer could be determined from the response functions and the efficiency of the NE213 spectrometer (determined for n-p elastic scattering). Using the appropriate efficiency and response functions measured with each respective spectrometer (NE213 and NE230), neutron fluence spectra for each target were determined.

In addition to the scope of this work, an exploratory work was undertaken to determine the neutron detection efficiency of the NE230 spectrometer using the available cross-sections for n-d elastic scattering. The unavailable cross-sections for n-d elastic scattering within the energy range of interest were estimated. Neutron fluence results calculated using the detection efficiency of the NE230 spectrometer using cross-sections for n-d elastic scattering were compared with the results measured with the NE213 spectrometer.

2. NEUTRON DETECTION AND MEASUREMENTS

2.1   Neutron detection with liquid organic scintillators

The quality of neutron fluence measurements is dependent on the detection system used for measurements. Liquid organic scintillators (NE213 and NE230) have been used for such measurements [Brooks & Klein, 2002] [Buffler, et al., 2002] [Herbert, et al., 2014] with the NE213 widely known to be more reliable [Zimbal, et al., 2006] [Baba, et al., 1999] [Sanami, et al., 2009]. The NE213 is used as a proton based scintillator, this is since the scintillation medium is a normal hydrocarbon (C:H), whilst the NE230 is normally used as a deuteron based scintillator, this is since the scintillation medium is comprised of deuterium and carbon (C:D). Since neutrons are not charged, they can only be detected indirectly. The mechanism of detection is that a neutron interacts with nuclei of the scintillating medium resulting in a release of charged particles. The recoiling particles excite the scintillation medium causing emission of light (scintillation), electrical signals from the scintillator due to recoiling charged particles are then processed by the detector system [Tavernier, 2010] [Crane & Baker, 1991]. The electrical signal produced is related to the energy and type of the particle responsible for the scintillation.

Charged particles resulting from the neutron interactions with the scintillation medium deposit their energy to the scintillation medium as they slow down [Buffler, 1991] [Knoll, 2000], causing excitation of the organic molecules (Scintillation medium). The excitation is basically due to that organic molecules used as a scintillation medium have electrons which occupy what is known as π-molecular orbitals, these valence electrons are delocalised and do not have any association with any atom [Knoll, 2000] [Leo, 1987] [Brooks, 1979]. The deposited energy is absorbed and excites these electrons to what is known as excited and vibrational states, scintillation light is emitted as electrons decay to ground state (detailed discussion on the scintillation process can be found in [Birks, 1964] [Knoll, 2000] [Leo, 1987]).

Scintillation light in organic scintillators is known to be made up of two components, namely, the fast exponential component corresponding to the prompt emission and a slow non-exponential component corresponding to the delayed emission as shown in figure 2.1. The scintillation is the sum of the two components. The two components have different lifetimes, with the fast component in the order of less than 30 ns [Craun & Smith, 1970], and

the slow component in the order of few hundreds of nanoseconds [Craun & Smith, 1970] [Klein, 2003] [Buffler, 1991].

Pulse shape discrimination is based on that the fraction of light in the slow non exponential component is dependent on ionising particle that caused the scintillation, for instance heavier particles produce more delayed light emission than light particles as shown in figure 2.2. A further discrimination by ionising particle is possible due to the difference in response of liquid organic scintillators to different secondary charged particles produced by neutrons [Buffler, 1991].
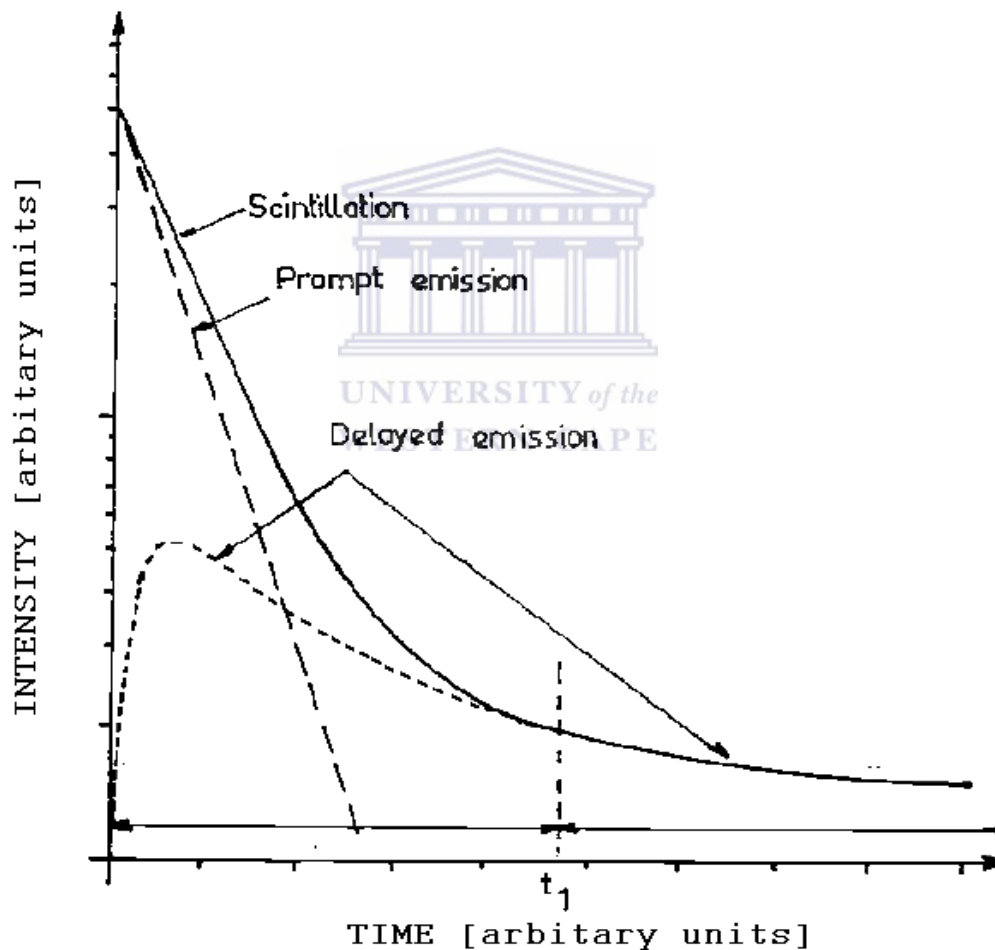
Figure 2. 1*: Schematic representation of the scintillation decay with time, also shown are the components (prompt emission and delayed emission) of the scintillation decay* [Laustriat, 1968].

7
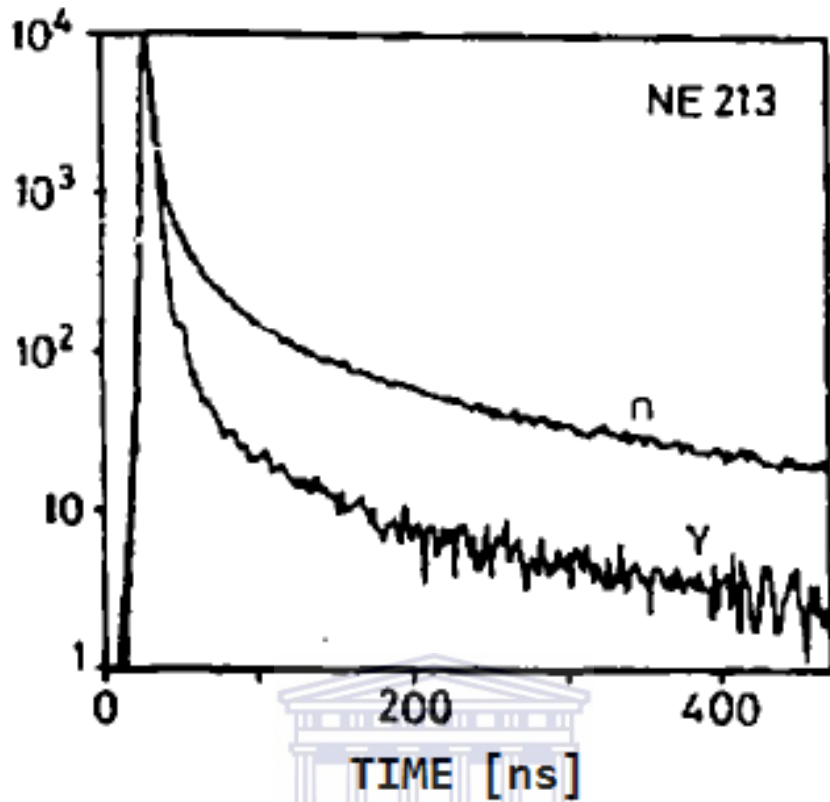
Figure 2. 2: *Measured scintillation pulses versus time (nanoseconds) in NE213 when excited by neutrons and gamma rays* [Leo, 1987].

2.2   Detector Response

Scintillators have a direct response to charged particles, the response,$L(E)$, of liquid organic scintillators to charged particles is known to be linear for electrons and non-linear for heavier charged particles and is well understood. Birks proposed that the non-linearity is caused by quenching effects in the scintillator and showed that the non-linear response can be modelled by the following relation [Birks, 1964]:

$$\frac{dL}{dx} = \frac{S\frac{dE}{dx}}{\left(1 + kB\frac{dE}{dx}\right)} \tag{2.1}$$

by high ionizing density along the particle track for protons and heavier charged particles. A number of models and different relations of these parameters have been proposed and are able to explain experimental data, with some models covering broader energy range of ionising particles [Klein & Brooks, 2006].

The scintillator response is also known to be different for different ionising particles as shown in figure 2.3. This is due to the fact that the specific ionisation density of the charged particle along the scintillation path is governed by the Bethe-Bloch relation, thus scintillation response depends on the type of the ionising particle at a particular energy, resulting in a more non-linearity for heavier ionizing particles [Buffler, 1991]. It can also be seen in figure 2.3 that for the same particle energy, the heavier charged particles produce less light output.
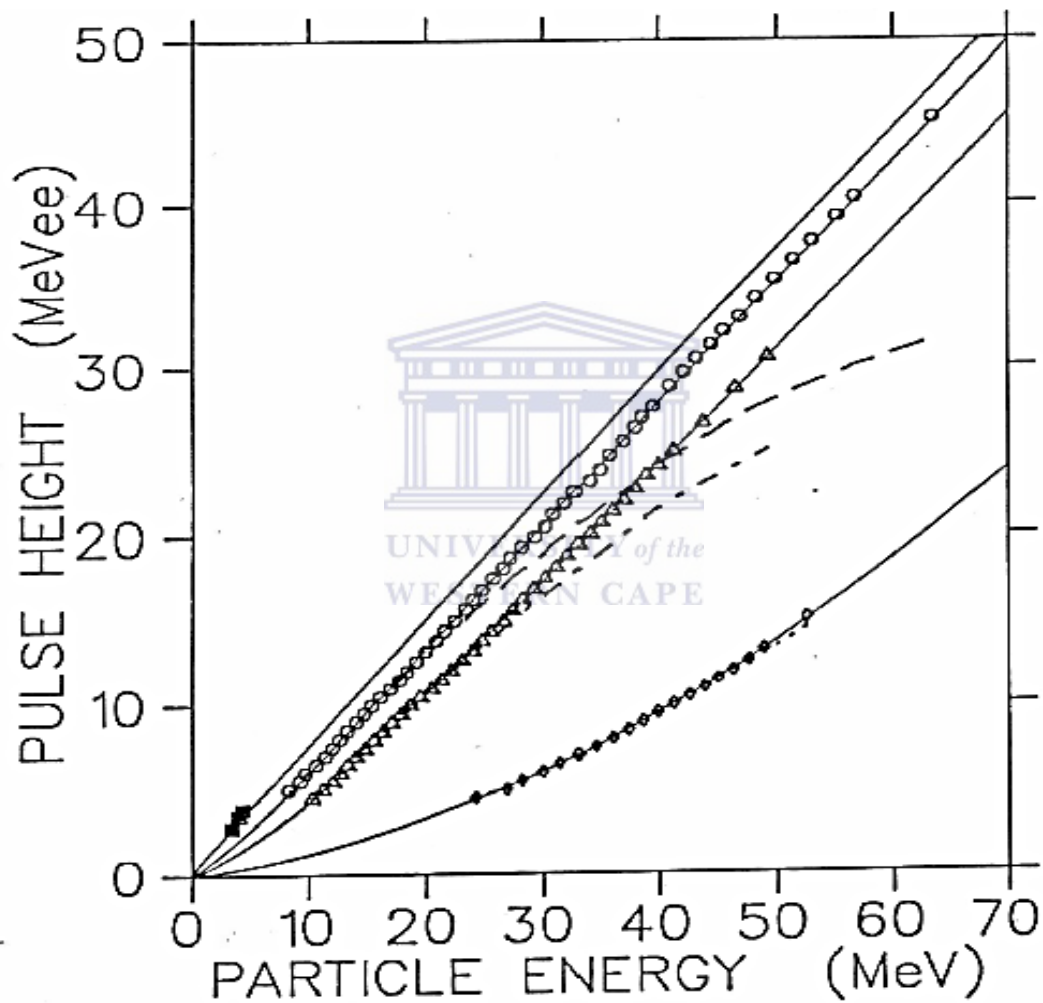
Figure 2. 3: *Measured scintillator response as a function of particle energy, shown measurements for (■) electrons, (○) protons, (Δ) deuterons, (◊) alpha particles, the solid line curves show response functions calculated using the Birks relation, and the dashed curves are the response functions without correction to the data [Buffler, 1991].*

Most measurements of the response of organic scintillators reported are at neutron energies less than 20 MeV, see references. [Bildstein, et al., 2013] [Craun & Smith, 1970] [Gagnon-Moisan, et al., 2012]. Most of these measurements have been carried out using the NE213 spectrometer [Gagnon-Moisan, et al., 2012] [Makupula, 2003] [Bildstein, et al., 2013] and few reported for the NE230 spectrometer [Craun & Smith, 1970] [Bertl, et al., 1972] [Bildstein, et al., 2013]. Shown in figure 2.4 are the semi-empirical fits by Craun *et al*. to the response data of the NE230 spectrometer to electrons and deuterons [Craun & Smith, 1970]. The response data to the NE230 spectrometer were measured by Smith *et al.* [Craun & Smith, 1970]. Without discussing the results obtained in detail, the two parameter fit was found to be better than the one parameter fit as shown in figure 2.4.
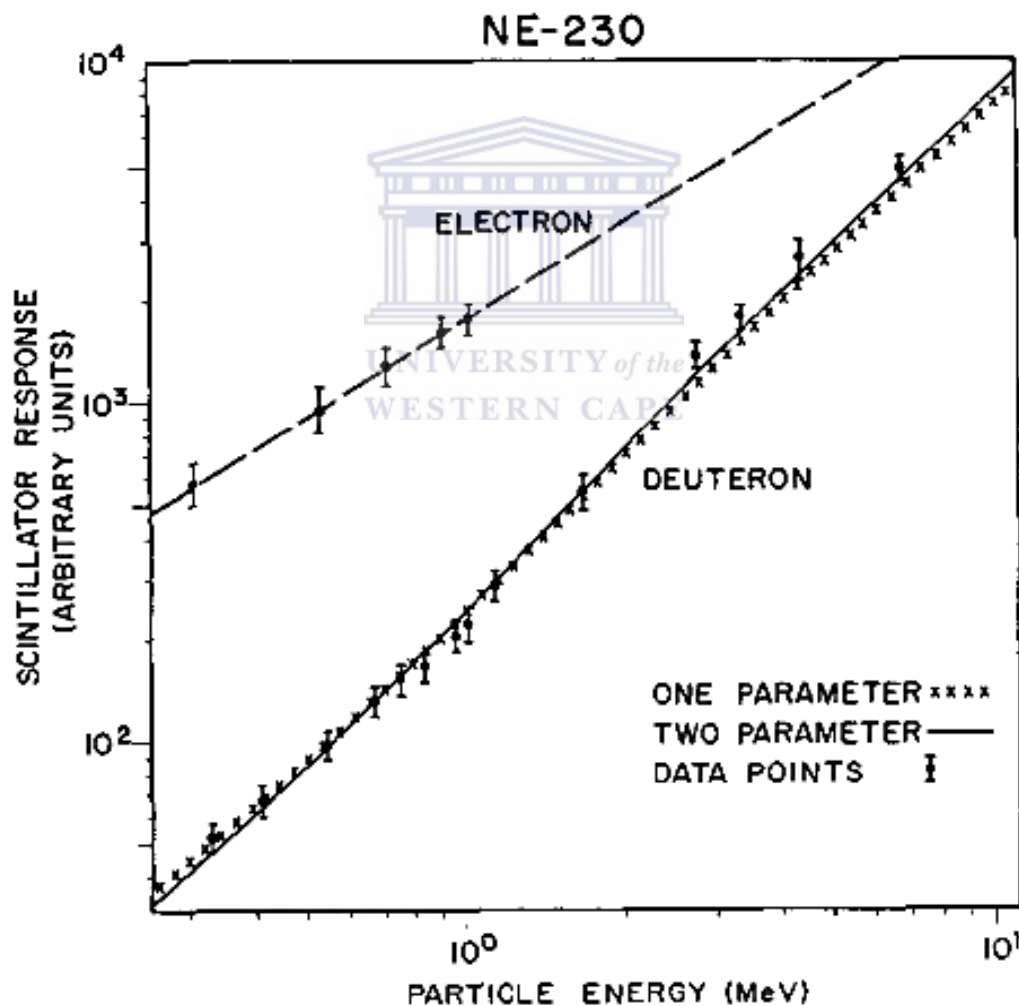
Figure 2. 4: *Semi empirical fits to the response data of the NE230 liquid organic scintillator to electrons and deuterons [Craun & Smith, 1970].*

2.3   Detector response function

The detector response function (pulse height spectrum) is a result of all interactions in the scintillation medium at specific energies. The simplest form of interaction with the scintillation medium is the n-p and n-d elastic scattering in proton based and deuteron based liquid organic scintillators respectively. This form of interaction tends to have a significant contribution at neutron energies less than 20 MeV [Buffler, 1991] [Meigo, 1997]. Neutrons can also undergo elastic scattering with carbon nuclei, however only about 28% of the neutron energy can be transferred to the recoiling carbon nuclei, as opposed to the maximum of 100% and about 89% of the energy transferred to protons and deuterons respectively (see appendix C). As the energy increases, interaction of neutrons with carbon nuclei producing protons, deuterons, tritons, and alpha particles become more competitive [Buffler, 1991].

The response function depends on the energy of the radiation incident on the detector, the type of the particle that caused the scintillation, and the detector geometry, size and shape [Buffler, 1991]. In addition, a number of factors such as non-linearity of the light output, particle escape (i.e. protons in NE213 and deuterons in NE230), multiple scattering of proton or deuteron depending on the scintillator, and carbon effects play a role in the measured response function [Karlsson, 1997]. To discuss but some effects:

- In cases were the detector size is small or at high neutron energies, particles such as protons or deuterons tend to leave the detector without depositing all their energies thus shifting high pulse height events to low pulse height events in the spectrum [Knoll, 2000][Buffler, 1991].

- A neutron may undergo multiple scattering with primary particles (protons or deuterons) before escaping the detector, resulting in addition of events to high pulse heights, this is due to that the multiple scattering is faster than the time taken for pulse shaping, thus all events from the recoiling primary particles are summed up, this effect generally occurs in large detectors [Buffler, 1991] [Knoll, 2000].

A resulting spectrum due to all effects with reference to hydrogen nucleus (proton) as a primary recoil particle is shown in figure 2.5, including non-linearity effects. Measured response function have additional factors such as photomultiplier statistics, collection of light

11

which is not uniform, and other factors contributing to noise which contribute to the spread in measured response function [Buffler, 1991] [Knoll, 2000]. Shown in figure 2.6 is the response function of 5 cm × 5 cm cylindrical the NE213 spectrometer [Buffler, 1991], also showing component spectra identified by pulse shape discrimination making up the sum spectrum labelled (All), the effects of detector resolution (spread) can clearly be seen in the measured spectrum, resulting in the spread at high pulse height as shown in figure 2.6.
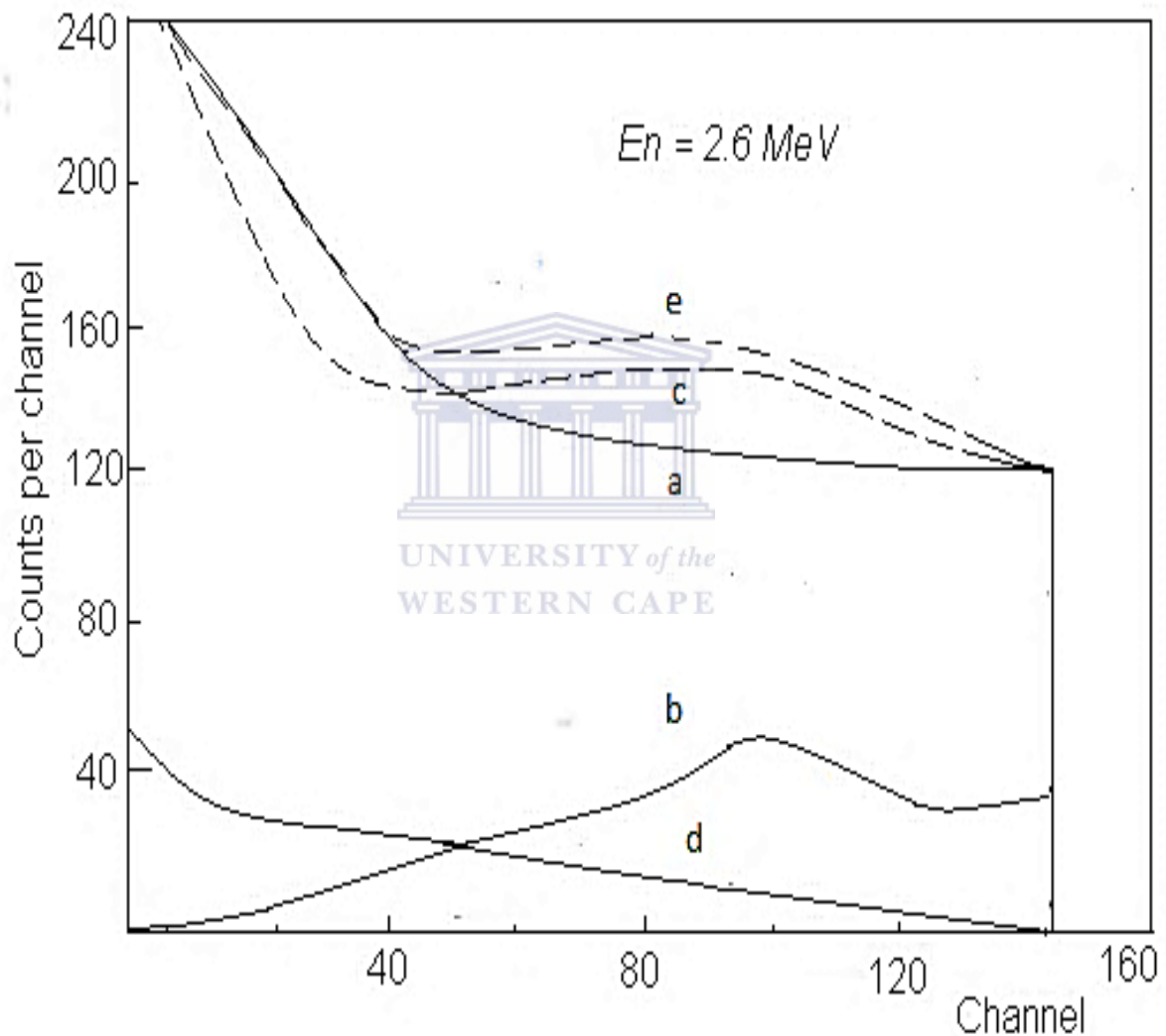
Figure 2. 5: *Different factors affecting the response function calculated for a cylindrical stilbene crystal at neutron energy 2.6 MeV, showing (a) single scattering with non-linearity of the detector and edge effects (b) multiple hydrogen nucleus scattering, (c) a sum of single and multiple hydrogen nucleus scattering, (d) protons recoiling from neutron initially scattered by carbon, (e) sum spectra of c and d [Knoll, 2000]*
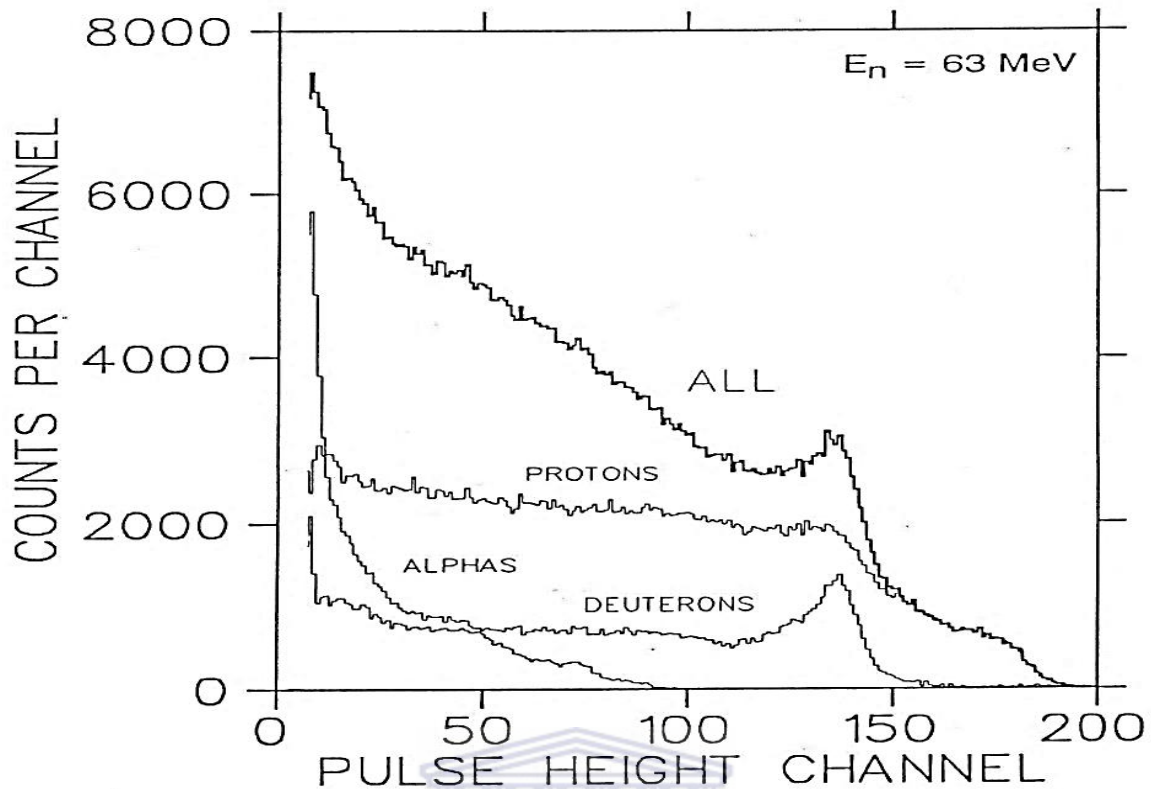
Figure 2. 6: *Response function measured at neutron energy of 63 MeV by 5 cm × 5 cm NE213 liquid scintillator, also shown are proton, deuteron, alpha particles response function components making up the sum response function (ALL) [Buffler, 1991].*

For measurements of response function with deuterated scintillators such as NE230, the differential cross sections for n-d elastic scattering are not symmetric about 90 degrees in the centre of mass frame at neutron energy range 2-20 MeV [Ojaruega, 2009]. There is a sharp backward peak at this angle, this results in a forward deuteron recoil peak in the response function. Shown in figure 2.7 are the differential cross-section for n-d elastic scattering for three energies (12.17 MeV, 14.1 MeV, and 20.57 MeV respectively), there is a dip at about centre of mass angle 120^0 which is consistent even at higher energies [Howard, et al., 1974], thus there is a pronounced peak in the response functions measured with NE230 above 1 MeV [Ojaruega, 2009]. The response function measured with the NE230 spectrometer for 22 MeV is shown in figure 2.8 [Pauletta, 1973], proton events (a) and deuteron events (b) were identified by means of pulse shape discrimination in figure 2.8. The pronounced deuteron peak can be clearly seen (fig 2.8 (b)).

Measurements [Buffler, et al., 2002] [Herbert, 2014] [Brooks & Klein, 2002] [Pauletta, 1973] and calculations of response functions with codes such as CECIL

13

[Cecil, et al., 1979], SCINFUL [Meigo, 1997], PRESTA [Takada, et al., 2011] and MCNPX [Tajik, et al., 2013] and etc. which are based on Monte Carlo methods have been reported. Most of these codes mentioned were designed to calculate and improve calculation of response functions for proton based scintillators such as NE213. Calculations of response functions measured with deuteron based scintillators such as NE230 may however be carried out using MCNPX and Geant4 subject to availability of cross-sectional data. The calculated response functions are fairly well reproduced at neutron energies $E_n < 20$ MeV, however there are discrepancies at neutron energies higher than 20 MeV [Meigo, 1997]. The discrepancies between measured and calculated response functions are primarily due to that most of the cross-sections for higher energies (above 20 MeV) for carbon breakup in proton based scintillators are not well known or are not accurate enough [Brooks & Klein, 2002] [Buffler, et al., 2002]. For deuteron based scintillators, both n-d and carbon break up cross-sections are not well known thus making code calculations more challenging to determine response function for deuterated scintillators such as NE230.
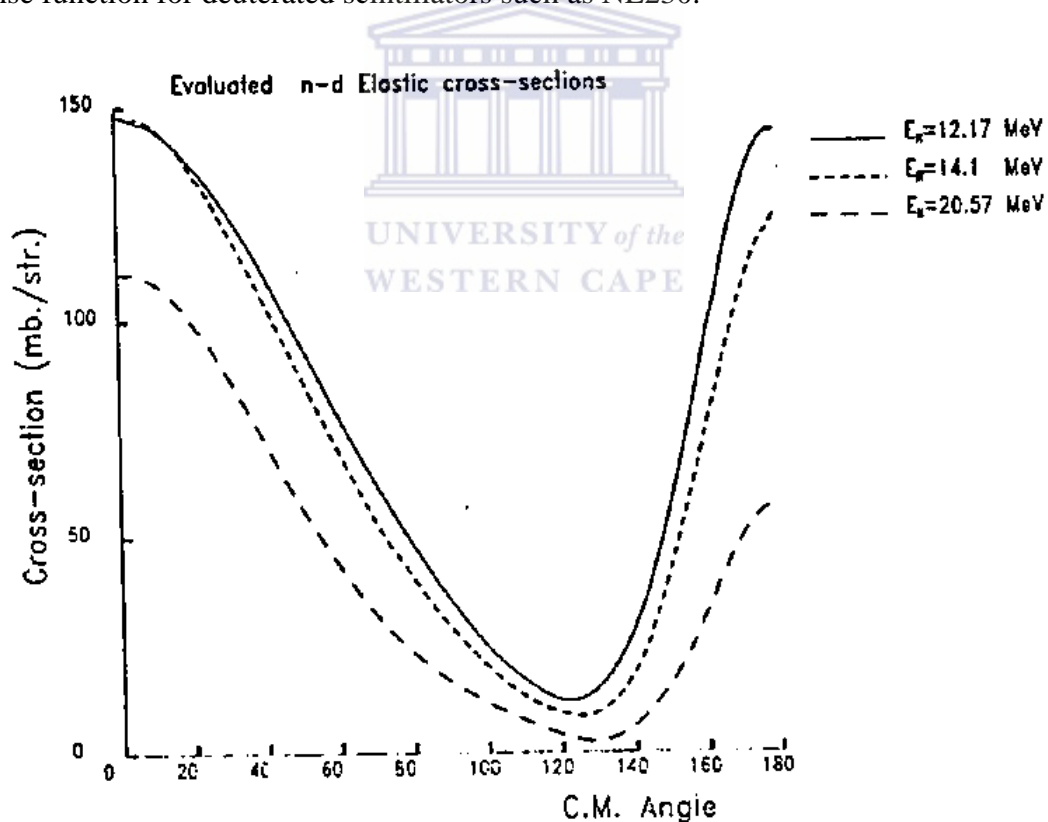
Figure 2. 7: Differential cross-sections for n-d elastic scattering for 12.17 MeV, 14.1 MeV, and 20.57 MeV respectively [Ojaruega, 2009].
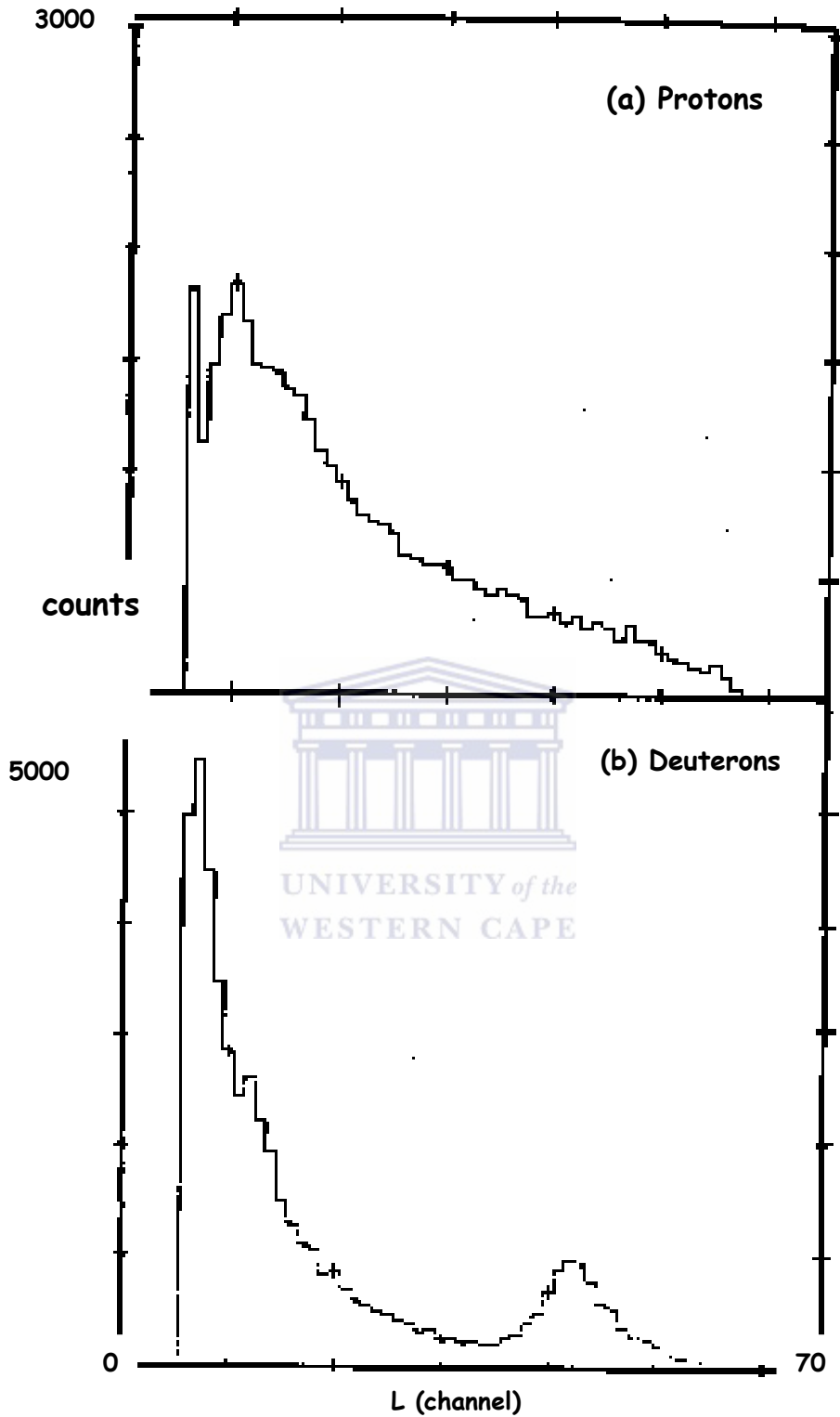
Figure 2. 8: *Adopted response function measured with The NE230 spectrometer for 22 MeV neutrons. Only deuteron events were selected by means of pulse shape discrimination (PSD) [Pauletta, 1973].*

2.4   Detector efficiency

The neutron detection efficiency may be understood as the probability of a neutron being detected by the detection system. The detection efficiency depends on the energy of the incident neutron, cross-sections (total and differential) for particular interaction in the scintillation system, size, shape and geometry of the scintillator, and the electronic threshold set by the detection system [Makupula, 2003]. Accurate knowledge of neutron detection efficiency is required for measurements of neutron fluence. There have been challenges over the years in measurements and calculations of neutron detection efficiency, primarily due to complexities of the response functions and unavailability of reaction cross-sections at energies greater than 20 MeV. There has however been a steady development in improving the accuracy of detection efficiency more specifically for proton based scintillators.

Calculations of neutron detection efficiencies are reliant on the accuracy of response functions amongst other quantities [Cecil, *et al.*, 1979] [Verbinski, *et al*., 1968]. Below 20 MeV response functions using Monte Carlo based codes can be reproduced [Meigo, 1997], this is due to that at this low neutron energy the n-p elastic scattering events are predominant, and the cross-sections are well known. As the neutron energy increases, response functions calculated using Monte Carlo codes are less reliable, this is due to the contribution of particles resulting from interactions with carbon, as mentioned above the n-^{12}C reaction cross-sections are not well known [Meigo, 1997]. Codes such as CECIL [Cecil, et al., 1979] and SCINFUL [Dickens, 1988] were developed to calculate response functions and detection efficiency above 20 MeV.

The detection efficiency of the NE213 spectrometer adopted from Meigo is shown in figure 2.9 for ^{60}Co and Am-Be biases [Meigo, 1997], the experimentally measured detection efficiencies are compared to the results measured by Verbinski *et al.*, calculated using codes CECIL and SCINFUL [Meigo, 1997]. The calculated results reproduced the experimental results well, however there was an overestimation at higher neutron energies (above 20 MeV) due to contribution from n-^{12}C interactions [Meigo, 1997]. The work showed that there seems to be great contribution due to n-^{12}C reactions above 30 MeV with the significant contribution due to n-p elastic scattering below 15 MeV [Meigo, 1997].

Most experimental work on the detection efficiency has been reported for the NE213 spectrometer, see references. [Meigo, 1997] [Verbinski, *et al*., 1968] [Brooks, *et al*., 2004]. Since the n-p elastic scattering cross-sections are well known even at neutron energies greater

than 20 MeV, some recent work on the detection efficiency have been reported for the detection efficiency of the NE213 spectrometer for n-p elastic scattering [Brooks, *et al.*, 2004] [Herbert, 2014]. Relatively less work on the calculations and measurements of detection efficiency of the NE230 spectrometer has been reported [Herbert, *et al.*, 2007] [Ojaruega, 2009] [Bildstein, *et al*., 2013]. The challenges involving the detection efficiency of the NE230 spectrometer is the unavailability of both n-d elastic scattering and n-^{12}C reaction cross-sections. To overcome this challenge Herbert *et al.* have reported work with the experimental neutron detection efficiency determined relative to the detection efficiency of the NE213 spectrometer [Herbert, *et al*., 2007]. The detection efficiency of the NE230 spectrometer simulated using MCNP-Polimi at different Photomultiplier Tube (PMT) thresholds adopted from Ojaruega [Ojaruega, 2009] is shown in figure 2.10. The humps were understood to be due to resonant states in the ^{12}C(d,n) reaction [Ojaruega, 2009].
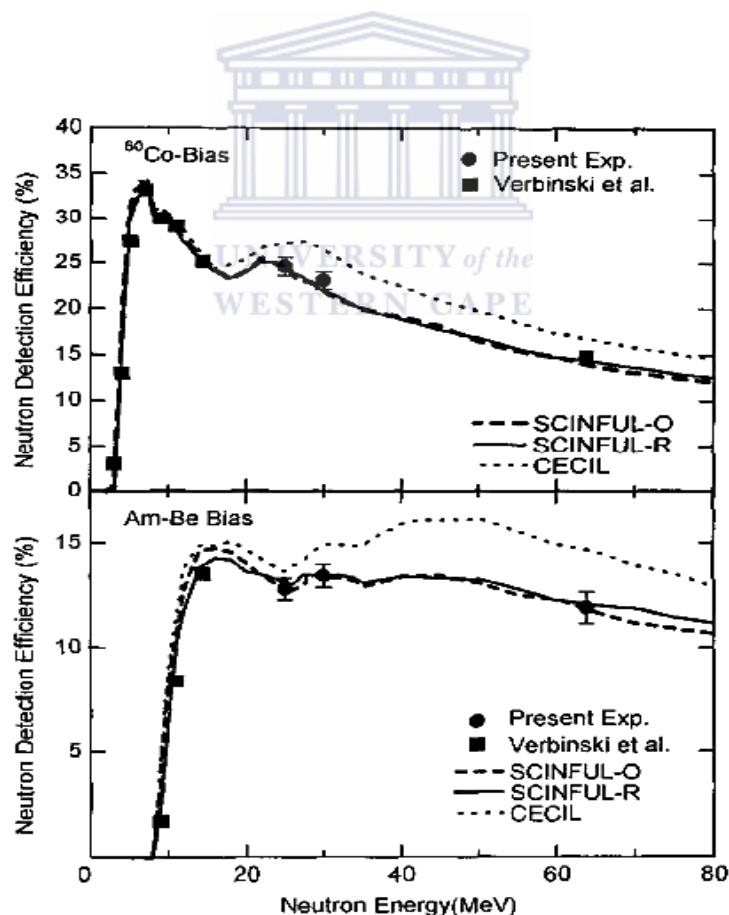
Figure 2. 9: *Detection efficiency of the 12.7 cm × 12.7 cm NE213 detector for ^{60}Co bias calculated using Monte Carlo codes CECIL and SCINFUL for H(n,p) and C(n,z) reactions [Meigo, 1997].*

17
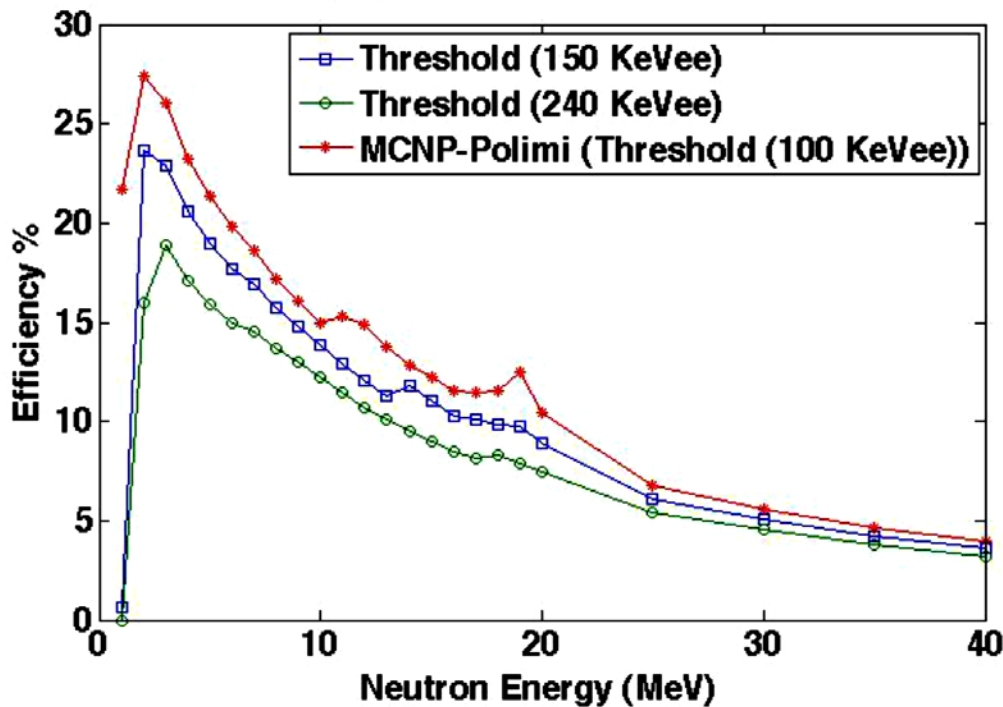
Figure 2. 10: *Total detection efficiency of the (2 inch × 2 inch) NE230 spectrometer simulated with MCNP-Polimi at different PMT thresholds [Ojaruega, 2009].*

2.5 Determination of Neutron Fluence Spectra

Neutron fluence spectra can be determined by means of calculations or experimental measurements. Calculations are widely carried out using codes based on Monte Carlo methods. Experimental measurements involve a number of varying techniques such as recoil spectrometry, threshold spectrometry, methods based on moderation and Time-of-Flight (ToF) method [Adams, 2010] [Herbert, 2009] [Alevra, 1999] [Brooks & Klein, 2002]. Both calculations and experimental measurements in determination of neutron fluence spectra present their own challenges which some will be highlighted in further discussions below.

2.5.1 Monte Carlo Calculations

Calculations of neutron fluence spectra involve the use of codes based on Monte Carlo methods as mentioned above, these codes have found uses in both application and research in nuclear physics. This includes codes developed such as FLUKA, MCNPX or MCNP6, and Geant4 [Adams, et al., 2010] [Herbert, 2014] [Herbert, *et al*., 2014] [Stepan & Bull, 2014]. FLUKA is useful in energy deposition studies involving very high statistics for particle transport [Adams, 2010]. A well-known code MCNPX which is a combination of MCNP and

LAHET [Hughes, *et al*., 1997] is used to calculate neutron fluence, MCNPX provides advantages in that it is capable of transporting and tracking up to nearly all particles and energies [Adams, 2010]. As a result MCNPX has found use in many areas of application such as medical physics where it can be used to characterize source spectrum in radiotherapy facilities [Bohm, *et al*., 1999], which is of particular interest to this present work. One of the codes that is still an open source and has found use in neutron fluence spectra calculations is GEANT4. This code was developed for elementary particle transportation and tracking [Adams, 2010] [Apostolakis, *et al*., 2009], it has however drawn interests and found use in other areas such as medical physics and nuclear physics [Agostinelliae, *et al*., 2003] [Cornelius & Rosenfeld, 2004].

Monte Carlo codes mentioned above have had success in reproducing experimental results [Adams, *et al*., 2010] [Herbert, 2014] [Alevra, 1999], as a result it have been used to benchmark experiments and in feasibility studies. However, as mentioned in sections 2.2 and 2.4, the challenge with carrying calculations of neutron fluence using these codes comes through the unavailability and lack of accuracy of some nuclear reaction cross-sections for energies above 20 MeV.

2.5.2 Neutron fluence measurements

As mentioned above there are various experimental methods in measurements of neutron fluence, depending on the neutron energy range and information of interest, either of the methods may be employed. In this section some of the methods will be briefly discussed, of these methods, recoil spectrometry and ToF method is of interest in the present work.

Recoil spectrometry involves observation of the recoiling nucleus [Tavernier, 2010], acceptable measurements can be for recoiling nucleus at all angles or a particular angle. Generally hydrogen nucleus is the preferred recoiling nucleus as it can undergo elastic scattering receiving up to all of the neutron energy, however other light nuclei such as of deuterium and helium can be of interest [Knoll, 2000]. Spectrometers such as organic scintillation spectrometers, proton recoil proportional counters, and recoil proton telescopes can all be used for this purpose [Brooks & Klein, 2002] [Alevra, 1999] [Knoll, 2000]. Organic spectrometers such as the NE213 and NE230 spectrometers are widely used as recoil spectrometers owing to their pulse shape discrimination for measurements in mixed fields such as in this present work and are suitable for in-phantom neutron fluence measurements [Herbert, 2009].

Methods based on moderation involve a slow neutron detector medium surrounded by a hydrogen containing moderator. Normally paraffin or polyethylene is used as a moderator surrounding the detector which can be LiI scintillator or a small ^{3}He counter [Alevra, 1999] [Tavernier, 2010] [Knoll, 2000]. The underlying principle for the method is that the detector have high efficiency for slow neutron detection, thus the surrounding moderator slows down high energy neutrons and then they are detectable by the detector [Brooks & Klein, 2002] [Alevra, 1999] [Knoll, 2000]. Bonners spheres form a class of these detectors and can be used as spectrometers known as the Bonner sphere spectrometer (BSS) [Brooks & Klein, 2002], BSS can cover a wide neutron energy range, however they have poor resolution [Brooks & Klein, 2002].

Neutron fluence measurements can also be carried out by means of Threshold methods, in these methods certain materials are exposed to a flux of neutrons for a period of time, for which the radiating particle can interact with some of the atoms in the materials, resulting in a radioactive isotope of the element or different elements [Brooks & Klein, 2002] [Knoll, 2000] [Negoita, 2004]. The radioactive products can be removed from the flux to count the radioactivity which can be used to determine neutron fluence. Radioactive products indicate that the threshold of the nuclear reaction is exceeded by the neutron energy responsible for the reaction [Brooks & Klein, 2002].

2.5.2.1 ToF method

The ToF method is one of the widely used techniques in neutron fluence measurements and has a long history [Copley & Udovic, 1993], see references. [Satoh, *et al.*, 2011] [Baba, *et al.*, 1999] [Mosconi, *et al.*, 2010] [Meigo, 1997] [Herbert, 2014] [Becchetti, *et al.*, 2013]. This method involves deduction of neutron energy from the flight time over a well-defined distance [Brooks & Klein, 2002]. This is done by taking the difference in time the neutron takes from the production point to the point of detection [Adams, 2010] [Ojaruega, 2009]. The point of detection can be triggered by recoiling particle in the detector, where the detector is placed over a well-known distance. In order to achieve this a start pulse and a stop pulse and a time to amplitude converter (TAC) or time to digital converter (TDC) are generally needed [Karlsson, 1997]. In cases where the neutron source is not pulsed, detectors may be used to record both the start and stop pulses of neutron flight [Karlsson, 1997] [Brooks & Klein, 2002]. One of the disadvantages of ToF is that the neutron time resolution is better with longer flight path, which then limits the technique to large

experimental area, usually at the expense of the solid angle [Ojaruega, 2009]. It is however important to note that due to different speed of neutrons and gamma rays, discrimination of neutrons and gamma rays is possible. The discrimination of gamma rays and neutron events is due to that gamma rays are located as a different group which can be easily identified in the ToF spectrum, however cosmic rays tend to contribute to the background since their speeds are random, thus cannot be discriminated against as gamma rays from neutrons in the spectrum [Karlsson, 1997] [Ojaruega, 2009].

An example of a ToF spectrum measured by Makupula is shown in the figure 2.11 [Makupula, 2003]. The spectrum was obtained from measurements with a stacked scintillator consisting of NE213 scintillator and a plastic veto detector. Neutrons were produced by bombarding 3 mm thick lithium target with a 99.21 MeV pulsed beam of protons [Makupula, 2003]. The features which are of interest to highlight is the predominant peak at 1546 ADC channels which is attributed to most energetic neutrons of energies 97.1 MeV, and the gamma ray group which, as discussed above, can be clearly distinguished at ADC channels 1776, 1864, 1972, these gamma rays have the same speed but different energies, ToF spectra will be further discussed in section 4.1.
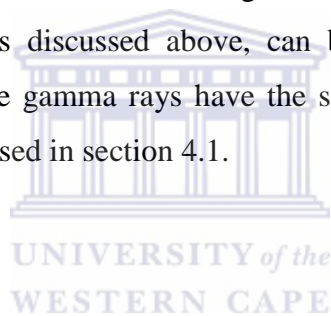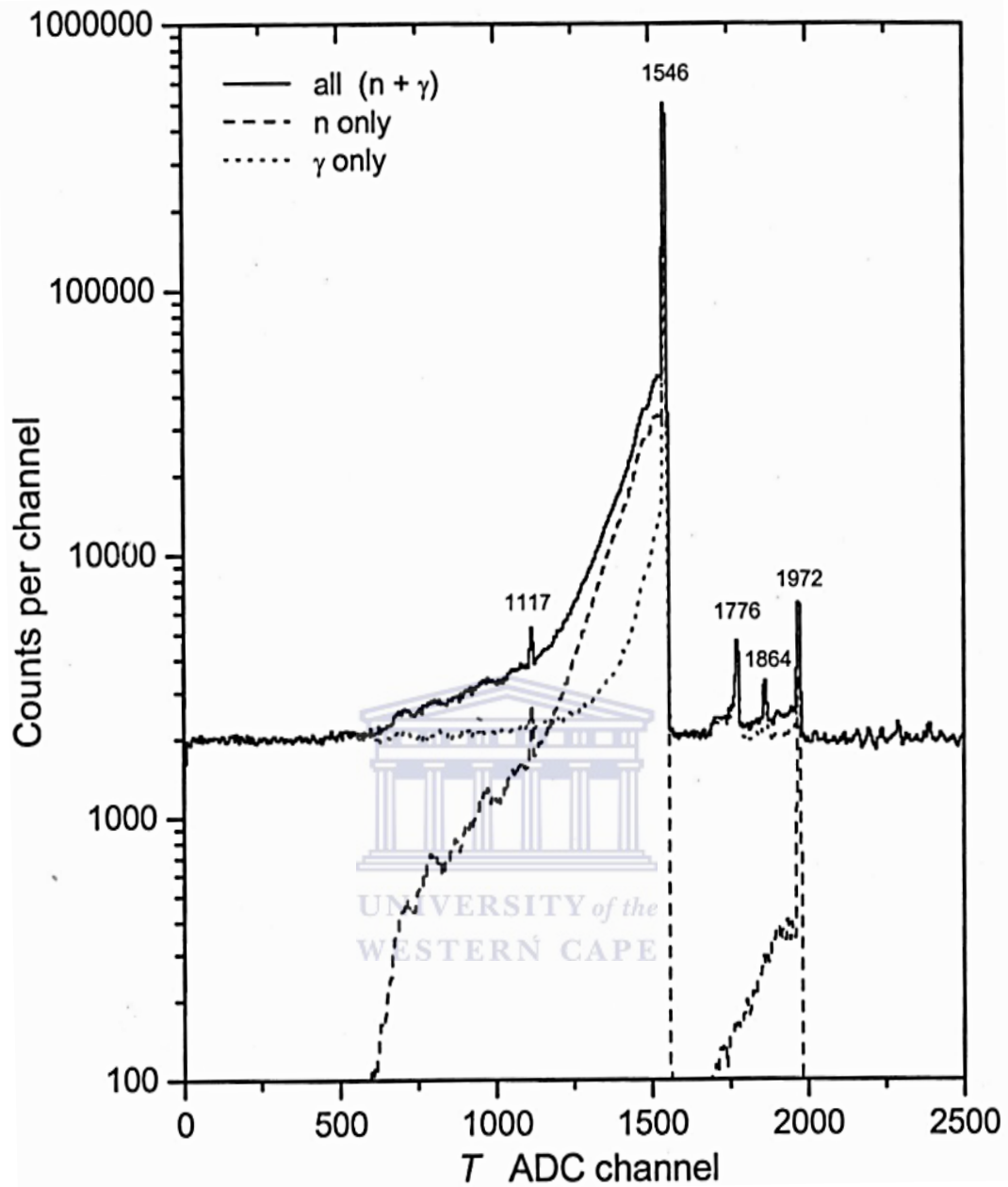
Figure 2. 11: *An example of the ToF spectrum adopted from Makupula using a lithium target, the spectrum was measured with a stacked scintillator [Makupula, 2003].*

3.   EXPERIMENTS AND DETAILS

3.1   Production of neutrons

Experiments were carried at the neutron ToF facility at iThemba LABS in South Africa. The layout of the experimental set up is shown in figure 3.1, this includes shielding from radiation, position of detectors used in the experiments, collimation for neutrons, the beam dump for protons, and different beam directions. A pulsed beam of 66 MeV protons from the separated cyclotron was projected to either a (1 mm) Lithium metal target, or (10 mm) Beryllium metal target, and or (10 mm) graphite target.
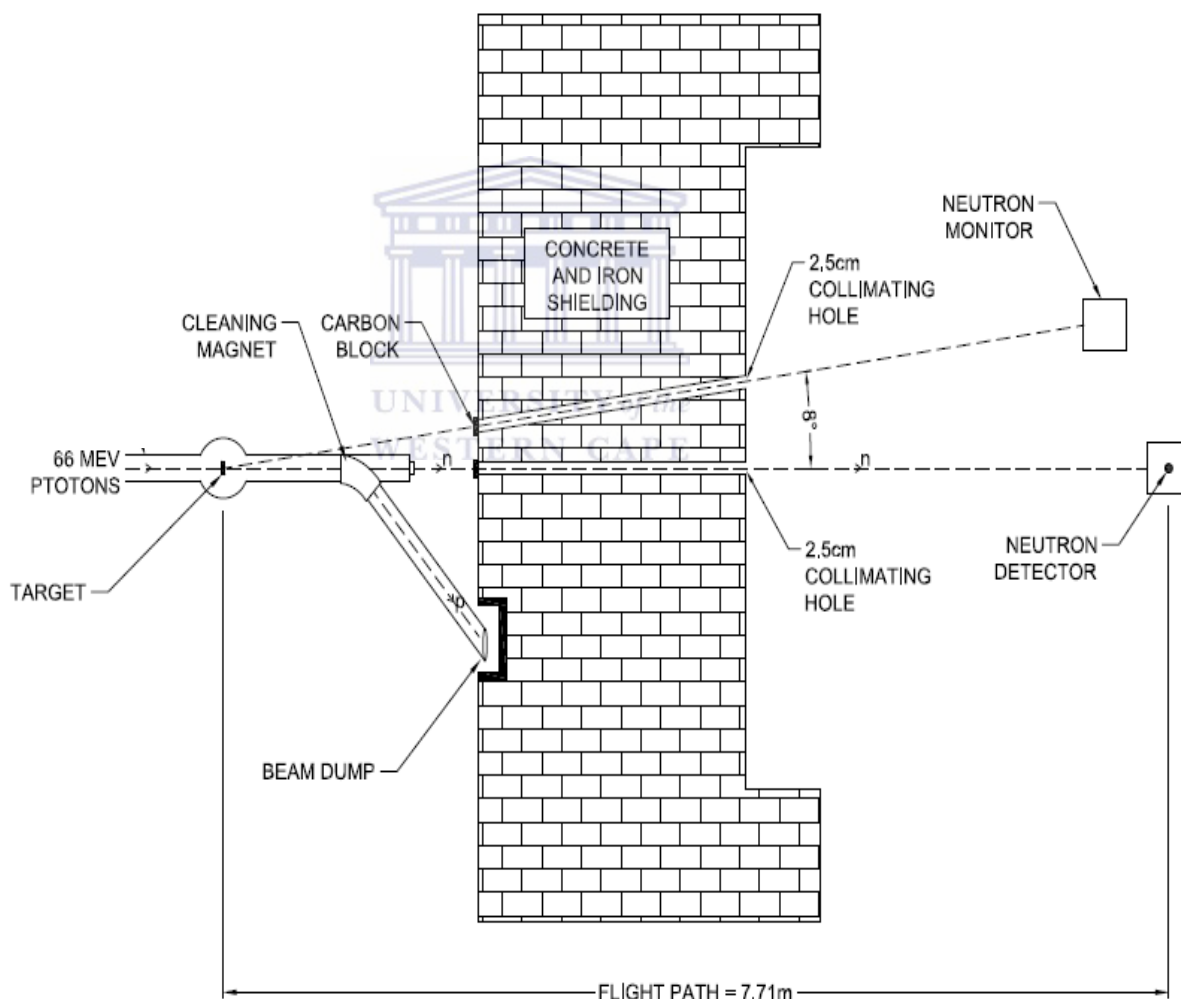
Figure 3. 1: *Schematic diagram of the experimental setup and the neutron beam line in the vault [Herbert, 2014].*

Neutrons were produced from each target via nuclear reactions; $^{7}Li(p,n)^{7}Be$, $^{9}Be(p,n)^{9}B$, and $^{12}C(p,n)^{12}N$. Collimation of neutrons beams produced was provided by circular apertures of

23

25 mm diameter. Neutron detectors were placed at an angle of 0^0 to the proton beam 7.71 ± 0.005 m away from the target, and the neutron monitor was placed at an angle of 8^0 to the proton beam 8.05 ± 0.005 m away from the target. A 2 m concrete and iron wall separated the target and the experimental area. Proton beam that passed through either of the targets was swept away by means of a clearing/dipole magnet to the Faraday cup, 6.5 cm thick graphite blocks placed in front of the collimator wall facing the target served to stop protons which were not swept away by the clearing magnet.

3.2   Beam profile measurements

Beam profile measurements were carried out by Herbert [Herbert, 2009], a cylindrical anthracene organic crystal of 10 mm diameter $\times$ 20 mm coupled to a RCA8850 photomultiplier using silicone jelly was used. The crystal was placed 7.71 ± 0.01 m away from the target, and horizontally mounted with its axis parallel to the 0^0 neutron beam. Figure 3.2 shows the horizontal and vertical scans made across the neutron beam, from the scans, events for fixed integrated proton charge were recorded.
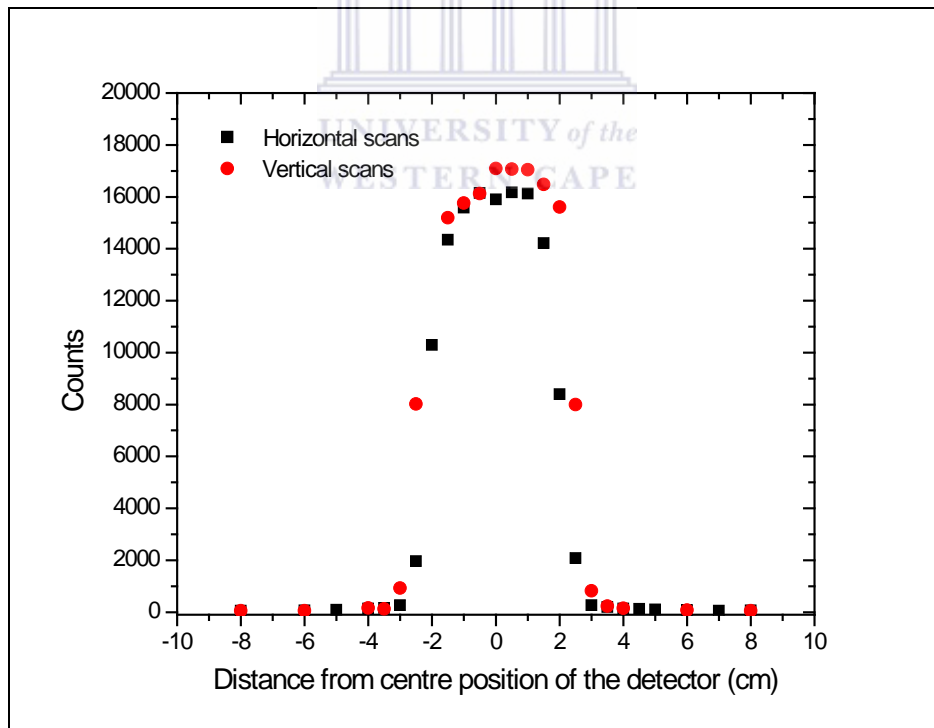
Figure 3. 2: *Horizontal and vertical measurements of the beam profile as a function of distance from the centre measured with an (10 mm diameter × 20 mm) anthracene organic crystal [Herbert, 2009].*

24

Recorded scans were as a function of distance from the centre at which neutron detectors NE213 and NE230 were to be positioned afterwards. The beam profile intensity was found to be uniform over a circular area of 5 cm diameter, from this it was concluded that the beam completely illuminated organic liquid scintillators NE213 (5 cm diameter × 5 cm) and NE230 (2.5 cm diameter× 2.5 cm).

3.3   Neutron detectors

Two neutron detectors used for measurements. The first detector was a (5 cm × 5 cm) cylindrical cell of NE213 organic liquid scintillator. The main components of NE213 was xylene ($C_6H_4(CH_3)_2$) with naphthalene ($C_{10}H_8$) added to reduce quenching effects [Buffler, 1991]. The scintillator cell was optically coupled with silicone jelly to an RCA8850 photomultiplier.

The second neutron detector was a (2.5 cm × 2.5 cm) cylindrical cell of NE230 organic liquid scintillator, the main component of the NE230 was deuterated benzene (C_6D_6) [EJ-315]. The cell was optically coupled with silicone jelly to an RCA8850 photomultiplier. To ensure that the NE230 organic liquid scintillator was water tight, the scintillator was inserted into a thin latex sheath, and the photomultiplier in a thin walled PVC tube. Table 3.1 shows some physical properties of NE213 and The NE230 spectrometers.

Table 3. 1: Physical properties of organic liquid scintillators NE213 and NE230 [EJ-301] [EJ-315] [Knoll, 2000].

	NE213	NE230
Light output % anthracene	78	60
Wavelength of maximum emission	425 nm	425 nm
Decay time (short component)	3.2 ns	3.5 ns
Refractive index	1.505	1.498
Density	0.874 g.cm^{-3}	0.945 g.cm^{-3}
Mass % of D	0	14.2
Mass % of C	92.3	85.7
Mass % of H	7.7	0.1
H:C atomic ratio	1.212	0.984

3.4 Electronics

Figure 3.3 shows details of the pulse processing electronic circuit used for measurements [Herbert, 2009]. For each event three parameters were mainly recorded, namely, the scintillation pulse height, L, fast integral of the anode pulse, F, and the timing parameter, T, which is the neutron ToF. In addition an independent parameter, D, generated from the dynodes of the photomultiplier tube of either NE213 or NE230, and the neutron monitor were recorded. For pulse processing, two independent chains of the electronic circuits were set up. Sources of pulse signals were either NE213 or NE230 detector assembly, the neutron beam monitor, and the time reference pulse from the RF cycle cyclotron.

Time reference pulse from the RF cycle cyclotron was taken 61 ns apart for 66 MeV protons produced from the cyclotron, to avoid overlapping of events from successive beam pulses, every fifth pulse was selected, thus making an interval of 305 ns between pulses. To stop time to amplitude converters TAC_A and TAC_M, a stop pulse T_{stop} synchronised to the pulse from the RF cycle cyclotron was used.

Four parameters L, F, T_{start} ,and logic pulse n were produced by the modified Link System Model 5010 pulse shape discriminator unit ($LINK_A$), which received an output from the anode of either NE213 or NE230 photomultiplier tube. The pulse height, L, was generated by integrating scintillation pulse over 500 ns, the fast integral, F, was generated by integrating over 30 ns. The timing output signal T_{start} was used to start TAC_A for neutron ToF measurements. The logic pulse used for discrimination between neutron and gamma events was produced by the discrimination circuitry, logic pulse n_γ could be selected during calibration runs to allow all events, associated with both neutron and gamma ray events. In addition an output from the dynode of either NE213 or NE230 photomultiplier tube was directed to the pre-amplifier and amplifier chain to produce an independent pulse height parameter D. The electronic threshold for neutron detectors was set at neutron energy of 5 MeV.

An output from the anode of the photomultiplier tube of the neutron monitor was fed to the $LINK_M$ unit, which produced the timing signal T_{start} used to start TAC_M for neutron ToF measurements. The logic pulse n was used for neutron event identification by pulse shape discrimination.
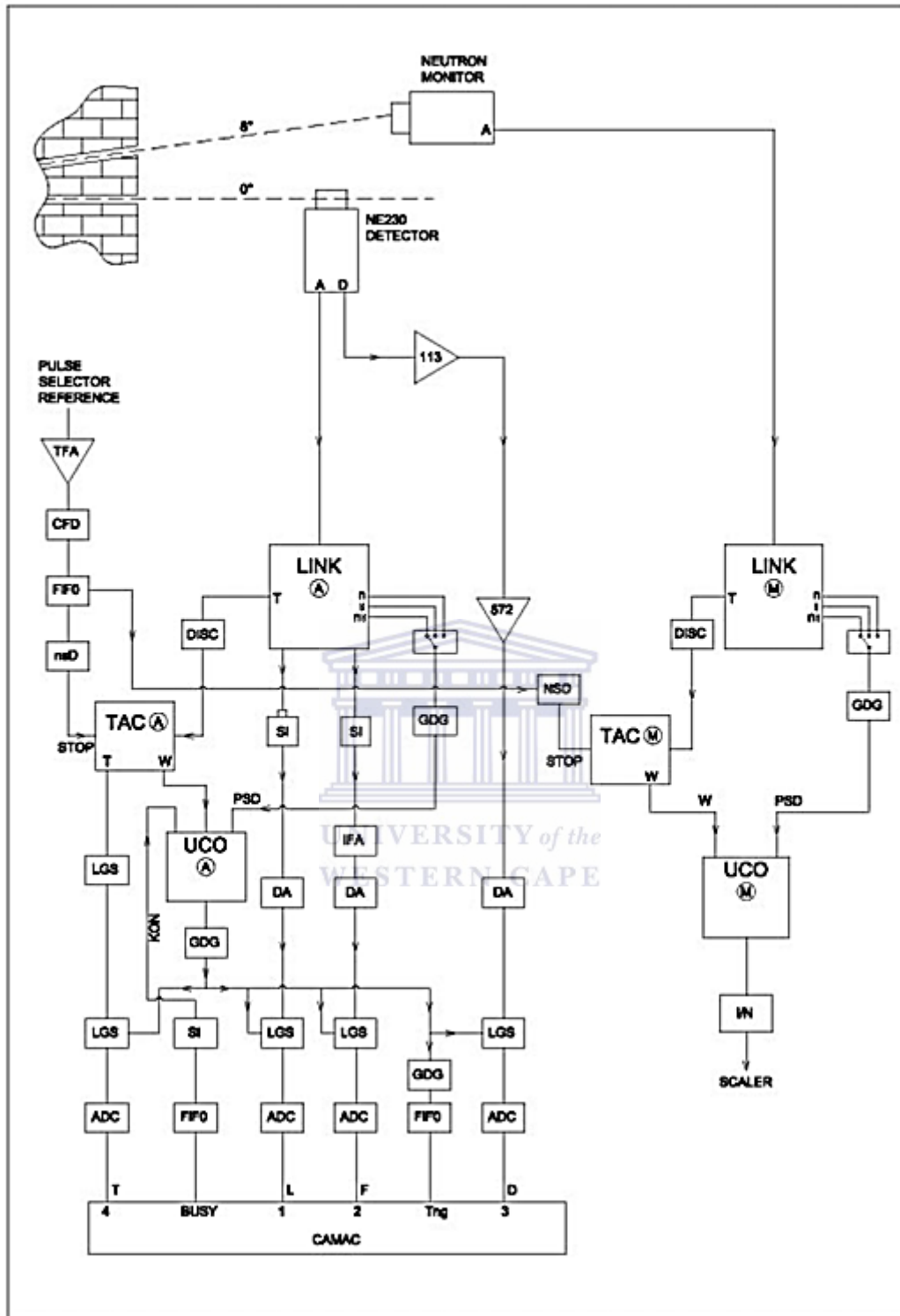
Figure 3. 3: *Detailed electronic circuit diagram used for pulse processing, taken from Herbert [Herbert, 2009].*

Two universal coincidence units (UCO) were used, namely, UCO_A and UCO_M, with UCO_A used for processing events for coincidence for either NE213 or The NE230 spectrometer, and UCO_M used for processing events associated with the neutron monitor. An output pulse was produced by UCO_A whenever time window (w) from TAC_A and PSD (n) were present at the same time. A pulse indicating the busy logic level was fed from the UCO_A, from which the UCO was used to allow data to be passed to the ADC's for conversions of analogue to digital signals by gating the linear gate and stretchers (LGS) units.

An output pulse was produced by the UCO_M whenever the time window (w) from TAC_M and PSD (n) from $LINK_M$ were present at the same time, the output pulse produced by UCO_M was directed into the scalar and recorded. Outputs produced by the ADC's were fed into the CAMAC interface linked to VAX 730 computer running XSYS data acquisition software via a Micro Branch Driver. Event by event data was recorded in memory and buffered in 4k blocks to magnetic tape to be analysed off-line. The off-line analysis was performed using a computer program GNU, available at iThemba LABS.

3.5 Measurements

Measurements were carried out in air with detectors NE213 and NE230. Either the NE213 or the NE230 spectrometer was mounted at 0^0 to the neutron beam with its axis perpendicular to the 0^0 neutron beam, 7.71 m away from respective targets. A series of measurements were made with either (1 mm) lithium metal target, or (10 mm) beryllium metal target, and or (10 mm) graphite target, the summary of the measurements is shown in table 3.2. During measurements neutrons were counted with an NE213 neutron monitor placed at an angle of 8^0 with respect to the proton beam (see figure 3.1), 8.05 m away from respective targets, neutron counts were obtained are also presented in table 3.2.

Table 3. 2: *Series of measurements with each detector placed at 0^0 with respect to the proton beam and target used for neutron production.*

Measurement	Detector used	Target	Target thickness (mm)	Run times (s)	Events
1	NE213	Li	1	600	814
2	NE213	Be	10	1500	25828
3	NE213	C	10	1680	9022
4	NE230	Be	10	1800	33303
5	NE230	C	10	2820	45103
6	NE230	Li	1	5280	10760

4   DATA REDUCTION

4.1   ToF measurements

4.1.1   ToF spectra

As discussed in section 3.1, three targets were used to produce neutron beams, namely, Lithium metal target (1 mm) or a Beryllium metal target (10 mm), and or a graphite target (10 mm), this was to achieve a broad distribution of neutron energies and good statistics across the range of interest (10-64 MeV). For a proton beam of 66 MeV, a 10 mm ^{12}C target produced neutrons of about 48 MeV maximum energy, this is owing to the high Q-value (-18.12MeV, see table 4.1) [NNDC], up to 64.15 MeV neutrons were produced from a 10 mm ^{9}Be target with Q-value (-1.85 MeV) [NNDC], and the ^{7}Li target produced most energetic neutrons of 64.356 MeV with Q-value (-1.644 MeV) [NNDC].

Figure 4.1 shows ToF spectra T (in ADC channel) for neutrons produced from ^{7}Li, ^{9}Be, and ^{12}C, measured with (a) the NE213 spectrometer and (b) the NE230 spectrometer. The effect of the Q-value for each neutron producing nuclear reaction for each respective target in the ToF spectra can be clearly seen, resulting in a shift to the lower ToF channels for lower neutron energy producing targets (i.e. ^{12}C and ^{9}Be targets). The energy loss (ΔE_p) of the proton beam in each target due to target thickness was calculated using the program ELOSS. The average energy of the proton beam in each target prior to production of neutrons was taken as the average of maximum proton energy (66 MeV) and minimum proton beam energy (after energy loss) in each target and is given by Eq. 4.1. Using the Q-values for each neutron producing target reaction (refer to table 4.1) and the average proton energy, the mean energies of neutrons produced from the unresolved ground state and first excited states in nuclear reactions ^{7}Li(p,n)^{7}Be$_{gs}$, ^{9}Be(p,n)^{9}B$_{gs}$, and ^{12}C(p,n)^{12}N for each target were calculated and are shown in table 4.1. Also shown in the table are the nuclear reactions.

$$\overline{E}_p = \frac{E_{p(incident)} + (E_{p(incident)} - \Delta E)}{2} \tag{4.1}$$

Table 4. 1: *Maximum neutron energies with Q-values produced from nuclear reactions for different target used in these experiments.*

Target	Nuclear reaction	Q-value (MeV)	ΔE_p (MeV)	$\bar{E}_p$ (MeV)	$E_{n(mean)}$ (MeV)
Li	$^7Li(p,n)^7Be$	-1.644	0.439	65.78	64.14
Be	$^9Be(p,n)^9B$	-1.850	16.41	57.80	55.95
C	$^{12}C(p,n)^{12}N$	-18.12	23.81	54.10	35.98

Figure 4.1 (a) and (b) shows ToF spectra for lithium target, these spectra are made of two components, the prominent peak at high ToF channels and a continuum at lower ToF channel numbers [Sisterson, et al., 2005]. The most energetic neutrons of ~64 MeV lie within a prominent peak in each spectrum, these neutrons arise from the unresolved ground and first excited states in ^7Be in the $^7Li(p,n)^7Be$ reaction. The width of the peak in each spectrum is a characteristic feature of the detector due to timing resolution of the detector, and may also be attributed to the energy loss of the proton beam prior to neutron production in the target, thus producing slightly lower energy neutrons falling within this peak. The Maxwell-like tail (continuum) at lower T (ADC channel) in each spectrum [Buffler, 1991], is attributed to neutrons produced from higher excited states in ^7Be and from breakup reactions resulting in multiple particles in the final state [Baba, et al., 1999] [Meigo, 1997] [Buffler, 1991].

The neutron ToF spectra using the (10mm) ^9Be target, see fig 4.1 (a) and (b) have a broad peak. Most energetic neutrons produced from the unresolved ground and first excited states in ^9B in the $^9Be(p,n)^9B$, with the mean neutron energy of ~56 MeV (refer to table 4.1) lie within this broad peak. The lower energy neutrons arising from the higher excited states in ^9B, breakup reactions and multiple scattering of neutrons before leaving the target lie in the tail as in the case of ^7Li target ToF spectra.

Most energetic neutrons in the neutron ToF spectra using the (10 mm) ^{12}C target, see fig 4.1 (a) and (b) produced from the unresolved ground and first excited states in ^{12}N in the $^{12}C(p,n)^{12}N$, lie within a peak which is unresolved by the energy resolution of the detectors. The peak in each of these spectra, see fig 4.1 (a) and (b) is much broader compared to ^7Li and ^9Be neutron ToF spectra, most neutrons produced from this ground and first excited states in ^{12}N lie within this broad peak with the mean calculated to be ~36 MeV.
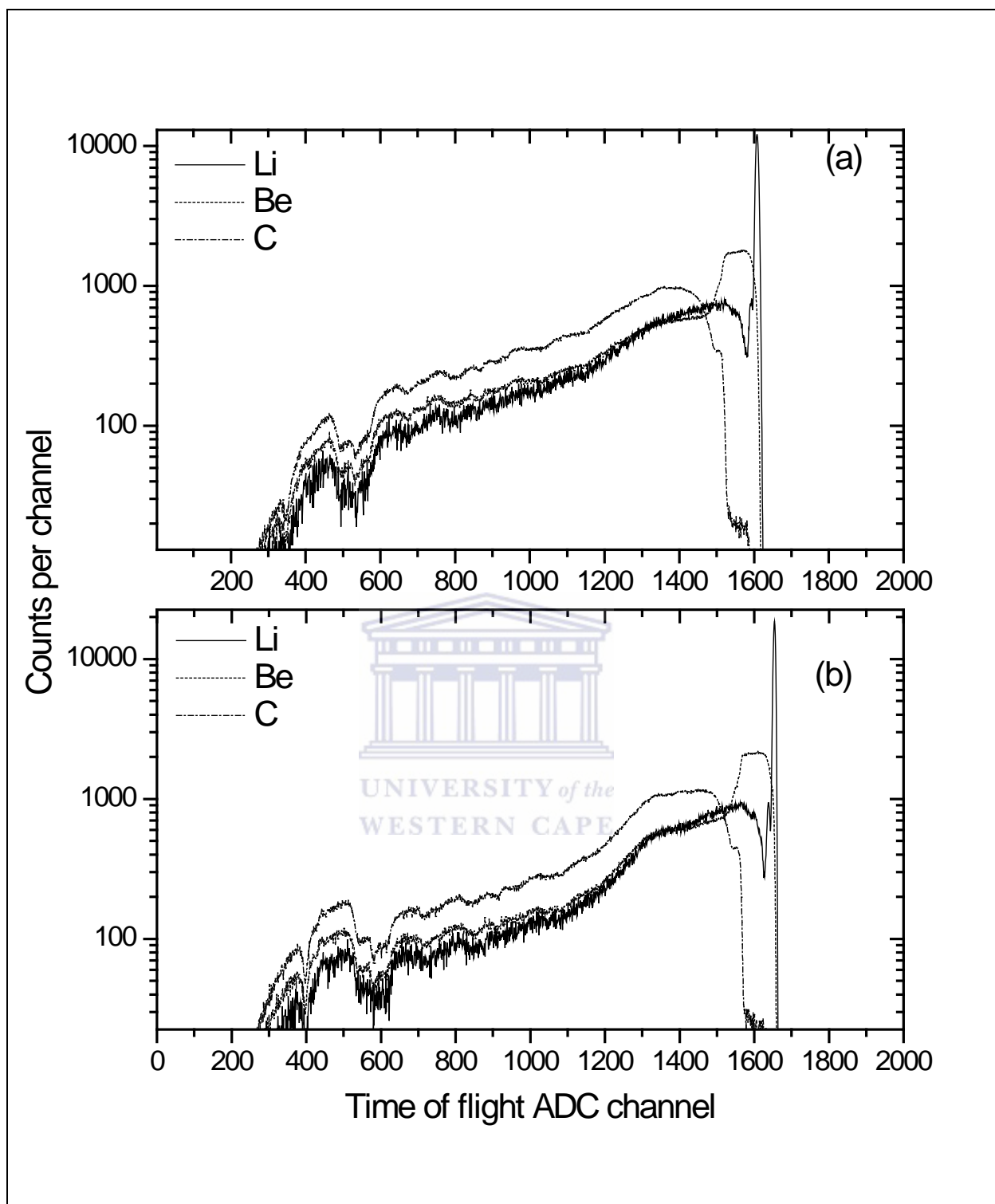
Figure 4. 1: *ToF spectra for ^{7}Li, ^{9}Be, and ^{12}C targets measured with (a) The NE213 spectrometer and (b) The NE230 spectrometer with counts plotted in log scale.*

There is evidence of the effect of target thickness with thicker targets exhibiting much broader peaks (^{9}Be and ^{12}C targets). The humps observed in the neutron ToF spectra between T=300-900 ADC channels (refer to fig 4.1 for clear observation) may be attributed to ^{12}C resonances associated with 6.5 cm thick graphite blocks placed at the face of the collimation wall facing the target (see section 3.1) [Herbert, 2009].

4.1.2   ToF to neutron energy calibration

Figure 4.2 shows neutron ToF spectra for ^{7}Li target measured with (a) the NE213 and (b) the NE230 spectrometers respectively. Events associated with neutrons and gamma rays were selected by means of Pulse shape Discrimination (PSD) for calibration purposes. As discussed in section 4.1.1, most energetic neutrons lie within the prominent peaks, the peaks were fitted using standard Gaussian functions, and were calculated to be 1607 and 1654 ADC channels for each spectrum measured using the NE213 and the NE230 spectrometers respectively. To the right of the neutron peaks are small gamma ray peaks, these peaks are attributed to gamma rays produced in or around the target in the proton beam line and are propagating at the speed of light c. The gamma ray peak at 1980 ADC channels is produced from the 6.5 cm thick graphite blocks, with the prominent gamma ray peaks at 2004 and 2051 ADC channels in each spectrum are produced in the target, respectively.

For calibration of neutron ToF to neutron energy, a calibration constant k was calculated using Eq. 4.2 from the prominent neutron and gamma ray peaks (2004 and 2051 ADC channel), and was found to have a magnitude of 8.37 ± 0.40 channels/ns.

$$k = \frac{T_{max} - T_{\gamma}}{t_{max} - t_{\gamma}}$$
(4.2)

The energies at the center of the peaks were estimated and taken to be 64 MeV. The neutron flight time for these most energetic neutrons was calculated to be 73.14 ns using Eq. 4.4. Over a flight path of 7.71 m, neutron energy can be calculated using the relativistic relationship:

$$E = m_n c^2 \left[\frac{1}{\sqrt{1 - (d/tc)^2}} - 1 \right]$$
(4.3)

with

$$t = \frac{d}{c\sqrt{1 - \left(\dfrac{m_n c^2}{E + m_n c^2}\right)^2}}$$

(4.4)

The relationship between ADC channels and flight time (t) was obtained by rearranging Eq. 4.2 (with the calibration constant taken as $k < 0$ in all calibration data reduction calculations) and was given by:

$$t = t_{\max} - \frac{(T_{\max} - T)}{k}$$

(4.5)

Using Eq. 4.3 and 4.5, neutron ToF (in ADC channels) were calibrated to neutron energy by the relationship:

$$E = m_n c^2 \left[\frac{1}{\sqrt{1 - \left(\dfrac{d}{\left(t_{\max} - \left(\dfrac{T_{\max} - T}{k}\right)\right)c}\right)^2}} - 1 \right]$$

(4.6)

where

T : The ToF in ADC channels

T_{max} : The ToF in ADC channel for the most energetic neutrons (64 MeV)

T_γ : The ToF in ADC channel for gamma rays (prominent peaks 2004 and 2051 ADC channels)

t_{max} : Neutron flight time for most energetic neutrons

t_γ : Flight time for gamma rays (25.73 ns)

k : Time calibration constant in channels/ns (8.37 channels/ns)

c : Speed of light (0.30 m/ns)

m_n : Rest mass of neutron (939.565 MeV/c^2)
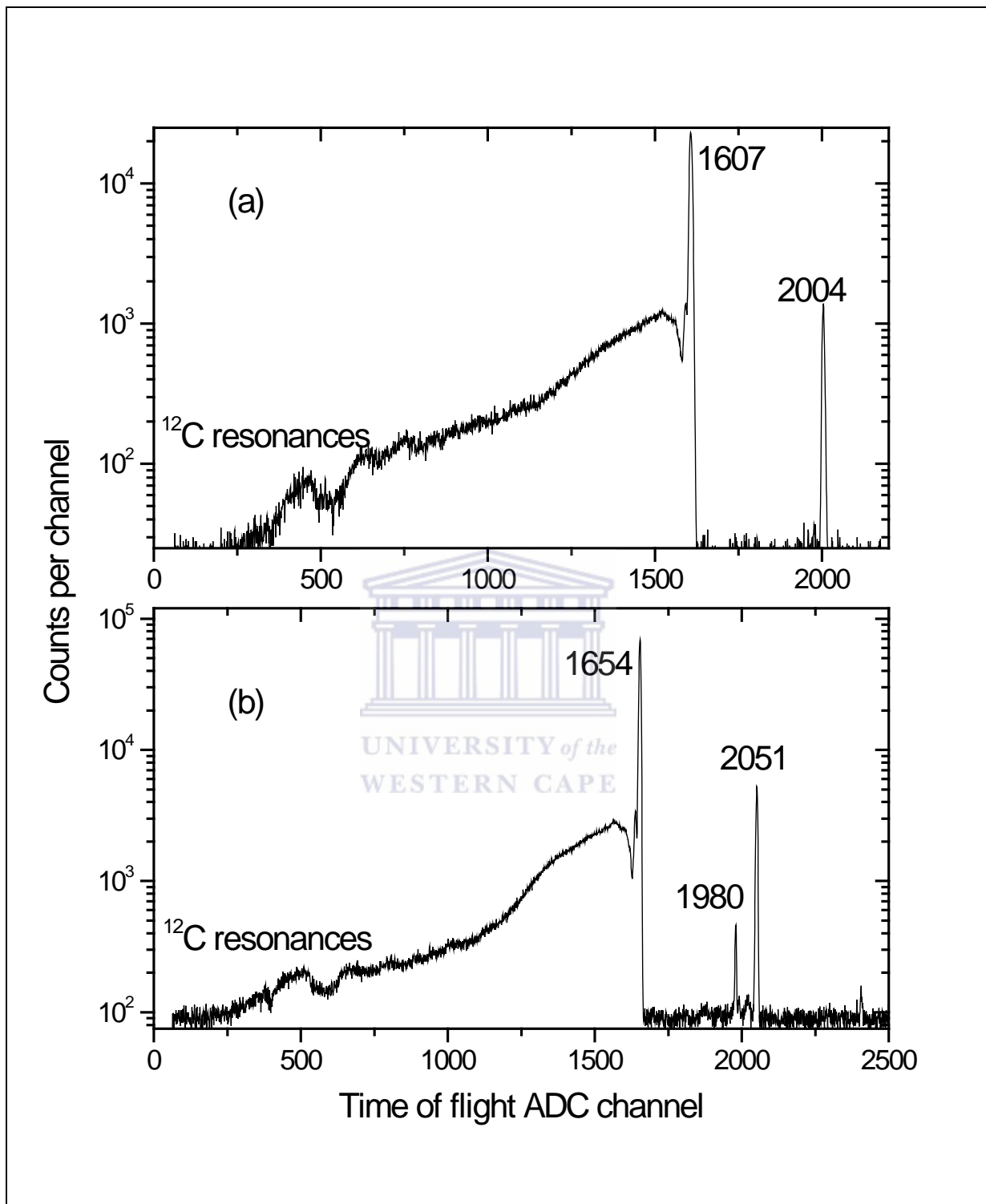
Figure 4. 2: *Neutron ToF spectra for neutrons produced by bombarding* ⁷*Li with 66 MeV proton beam, measured with (a) NE213 and (b) The NE230 spectrometers. Also shown are gamma rays produced in or around the target in the proton beam line.*
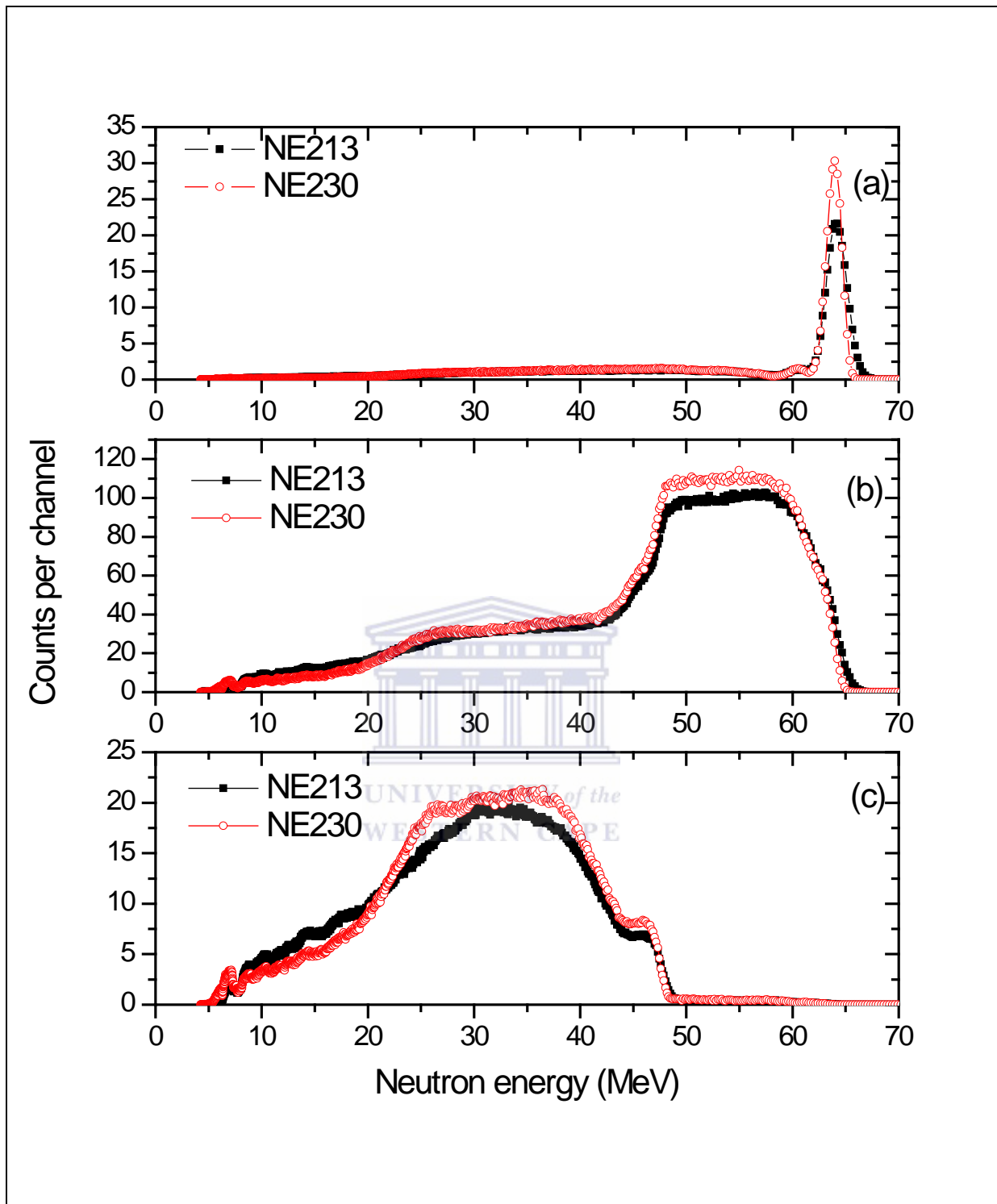
Figure 4. 3 : *Comparison of energy spectra obtained by converting ToF channels into neutron energies measured using the NE213 spectrometer (black solid histograms) and the NE230 spectrometer (red circle histograms).*

A comparison of energy spectra for each target with the ToF parameter calibrated to neutron energy is shown in figure 4.3. Each spectrum was normalized to the number of events measured by the neutron monitor during measurements with the NE213 spectrometer (refer to section 3.5). The spectra show satisfactory agreement with each other, however the ^{7}Li energy spectra measured using the NE213 and the NE230 spectrometers show better agreement compared to energy spectra for ^{9}Be and ^{12}C measured with the two spectrometers. Disagreements in the measured energy spectra may be attributed to characteristics of each detector (NE213 and NE230 spectrometers), these include mainly the efficiency and resolution of each detector.

The energy resolution of the detection system ΔE (which is the uncertainty associated with the neutron energy) is dependent on the ToF resolution of the detection system Δt_{γ} (i.e. NE213 and the NE230 spectrometers), the uncertainty in flight path Δd, and the spread in the mean proton energy in the Li target. The FWHM of the gamma ray peak gives the intrinsic ToF resolution measured to be 0.92 ns and 0.77 ns for NE213 and NE230 (fig 4.4 (a) and (b)) respectively. In the limit $\frac{\Delta t_{\gamma}}{t_{\gamma}} \gg \frac{\Delta d}{d}$, the energy resolution ΔE is given by:

$$\Delta E = \left[\left(1 + \frac{E_{n}}{m_{n}c^{2}} \right) \left(2 + \frac{E_{n}}{m_{n}c^{2}} \right) E_{n} \right] \frac{\Delta t_{\gamma}}{t} \qquad (4.7)$$

Figure 4.5 shows the energy resolution of (a) NE213 and (b) NE230, with energy resolution at 64 MeV calculated to be 1.8 MeV and 1.5 MeV respectively. Time windows to select neutron energies in the offline analysis were set to be of equal width of 2 MeV above the energy resolution at 64 MeV for each detector resolution, and this improved the counting statistics in the pulse height spectra used in this work and will be discussed in details in section 4.3.
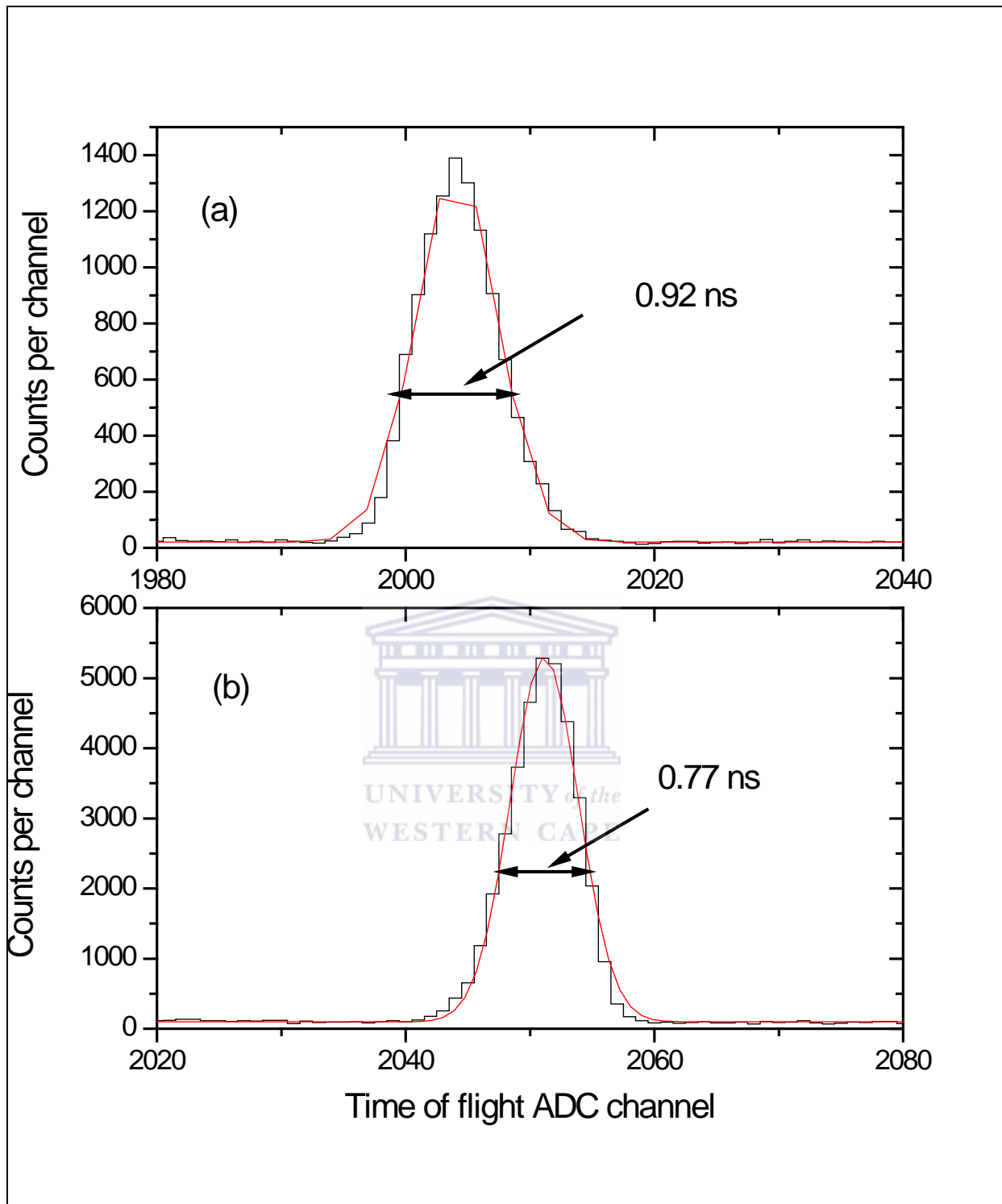
Figure 4. 4: *A Gaussian fit (solid line) to the gamma ray peaks at (a) 2004 ADC channels and (b) 2051 ADC channels, measured with NE213 and The NE230 spectrometers respectively with FWHM shown in the diagram*

38
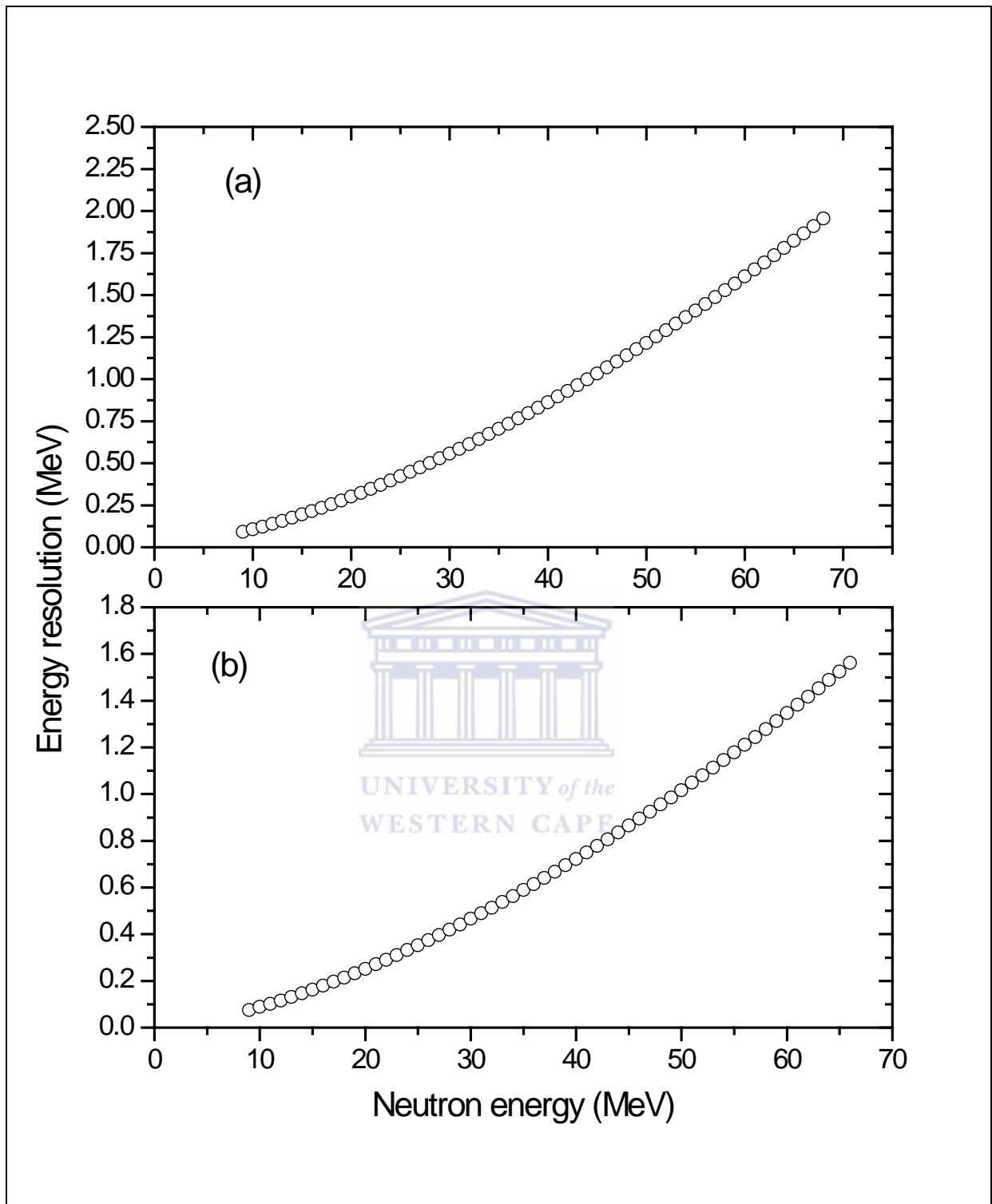
Figure 4. 5: Energy resolution as a function of neutron energy in the range of 10-64MeV for (a) The NE213 spectrometers and (b) The NE230 spectrometer.

4.2   Particle Identification

Organic liquid scintillators NE213 and The NE230 spectrometers offer good Pulse Shape Discrimination (PSD), the principles of PSD were discussed in section 2.1. Events associated with gamma rays (identified by Compton electrons) were suppressed during measurements using a PSD function from the LINK described in section 3.4, this allowed only events associated with neutrons for measurements. For further particle identification offline, a pulse shape parameter, S, was computed using L and F parameters and was given by:

$$S = L + kF + C \tag{4.8}$$

where L is the pulse height output, F is the fast integral, k and C are arbitrary constants set on the data to optimize the difference between the particle loci on the LS display, k gives the angle on the loci and C gives the position of the data on the S-axis. Figures 4.6 and 4.7 show the perspective view of counts (vertical) as a function of pulse height and pulse shape measured with the NE213 and the NE230 spectrometers respectively for neutrons of up to 64 MeV produced from the ^{7}Li (1 mm). Neutron detection of events via recoiling charged particles responsible for the scintillation form well defined ridges in the LS-plot (figs 4.6 and 4.7). Ridges are well separated at higher pulse height (L) in the LS-plane, however the difficulty to separate ridges at lower L values increases due to poor photomultiplier statistics.

For the NE213 detection system (fig 4.6), events are associated with escape protons (ep) at the far left ridge, which are due to protons that leave the detector without depositing all their energy onto the scintillation medium, this trend to increase with increasing particle energy (proton), protons (p) from both elastic scattering and n-C reactions, deuterons (d) and (α) alpha particles arising from n-C reactions (Buffler, 1991) (Brooks, 1979). For measurements with the NE230 detection system (fig 4.7), events are associated with charged particle escape (ep) (both proton and deuteron), protons (p) from both n-C reactions and deuteron breakup reaction (^{2}H(n,p)2n), deuterons (d) from n-d elastic scattering and n-C reactions, and (α) alpha particles from n-C reactions.

Pulse shape discrimination cuts C_1, C_2, C_3 and C_4 used to separate and select charged particle events of interest are also shown in figures 4.6 and 4.7. PSD cuts were obtained using a computer program GNU in the offline analysis. The program allows the user to define a limit (upper and lower) on the region of interest for a series of points on the LS spectrum   [Buffler,

40

1991], the program fits a smooth curve through these points, and events bounded within these curves by the program (e.g. C_1 and C_2) can be selected as events of interest [Buffler, 1991]. PSD cuts C_1 and C_2 were used to select only proton events on the *LS*-plot measured with the NE213 spectrometer (fig 4.6). PSD cuts C_3 and C_4 were used to select only deuteron events measured with the NE230 spectrometer (fig 4.7).

The cuts were set where at least ridges of different charged particles overlapped. Figure 4.8 and 4.9 show pulse shape spectra measured with NE213 and NE230 respectively. The pulse shape spectra were obtained by projecting events in the LS-spectrum onto the S-axis. It can be seen that cut C_1 and C_2 will not separate all proton events from escape proton and deuteron events respectively (fig 4.8), with escaping protons and deuterons leaking through to proton events calculated to be about 1% and 5% respectively.
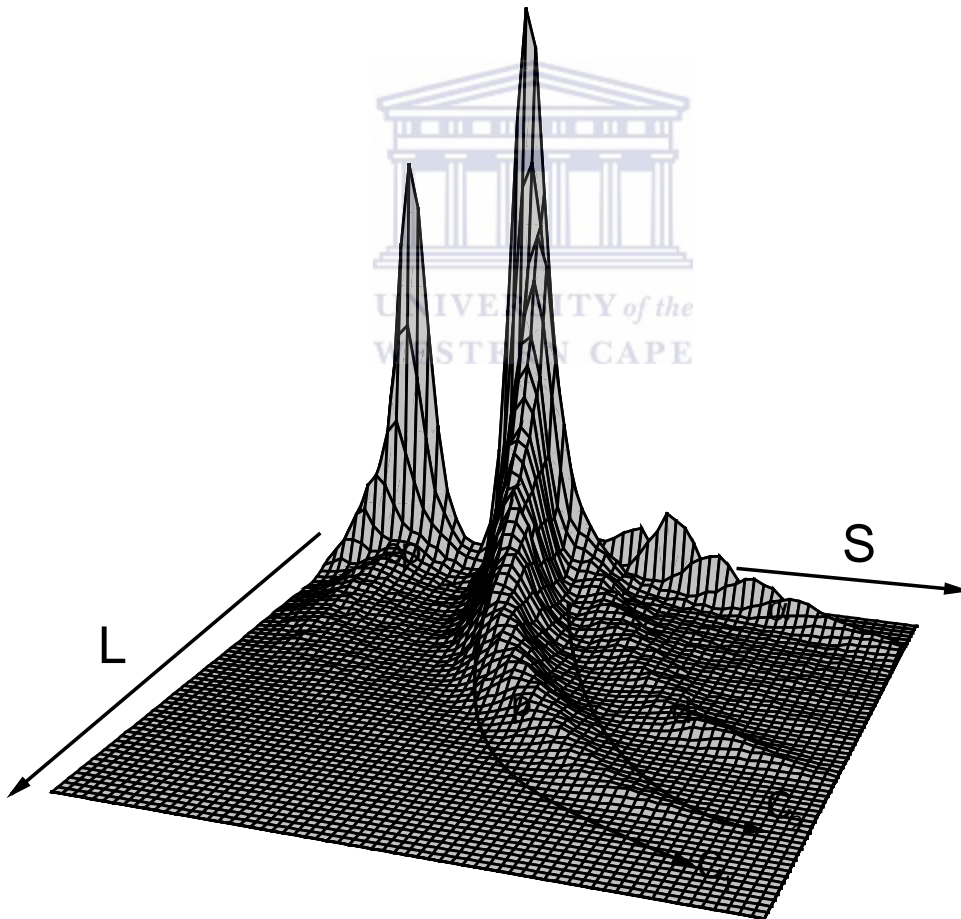
Figure 4. 6: *Perspective view of counts (vertical) as a function of pulse height and pulse shape, measured with the NE213 spectrometer for 66MeV proton beam incident on (1 mm) ^{7}Li, also shown are identified particles by PSD, escape protons (ep), protons (p), deuterons (d), and alpha particles (α) together with PSD cuts used in this work.*
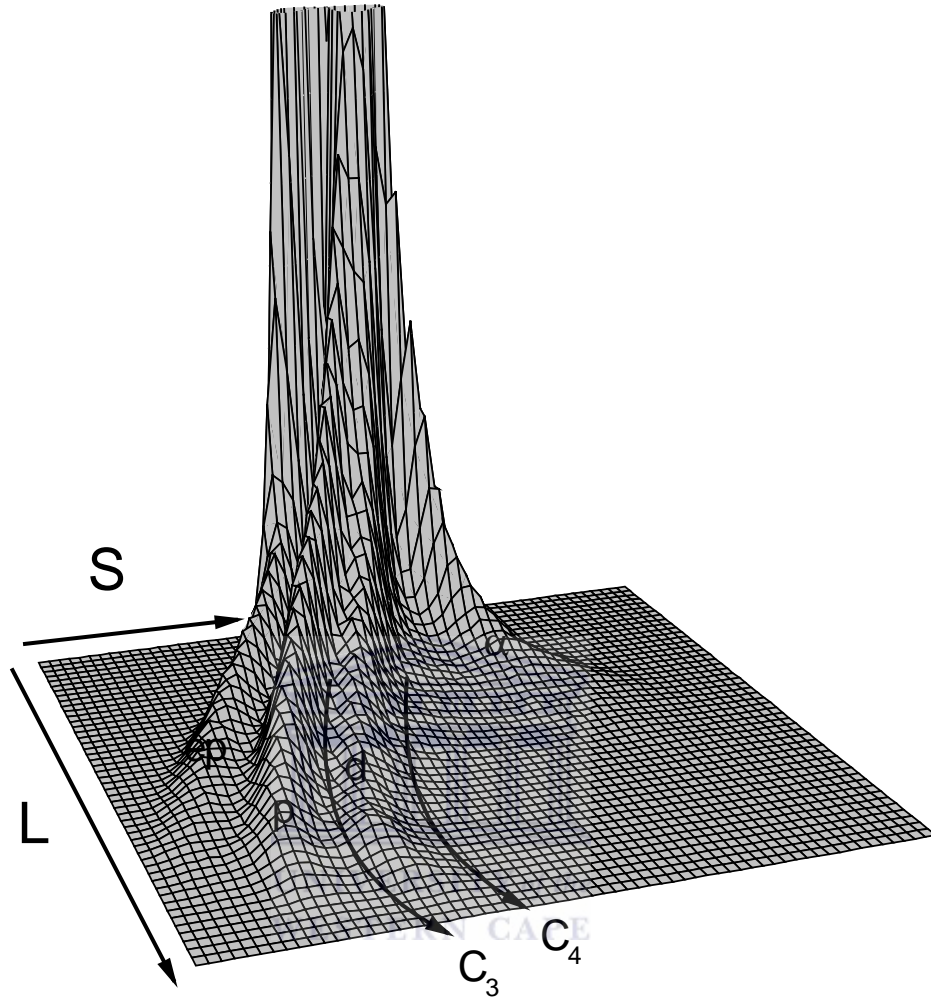
Figure 4. 7: *Perspective view of counts (vertical set to 10000 counts) as a function of pulse height and pulse shape, measured with the NE230 spectrometer for 66MeV proton beam incident on (1 mm) ^{7}Li, also shown are identified particles by PSD, charged particle escape (ep), protons (p), deuterons (d), and Alpha particles (α) together with PSD cuts used in this work.*

Similarly cuts C_3 and C_4 will not separate all deuteron events from proton and alpha particles events (fig 4.7). Proton events leaking through to deuteron events were calculated to be about 40% overall at low pulse heights and 6% at intermediate and to be about 2% at higher pulse heights, less than 1% of alphas leaked to the deuteron events. In both pulse shape spectra measured with the NE213 and the NE230 spectrometers, the ridge due escaping particles

diminishes at higher pulse height, as mentioned this is primarily due to that particle escape increases with particle energy.
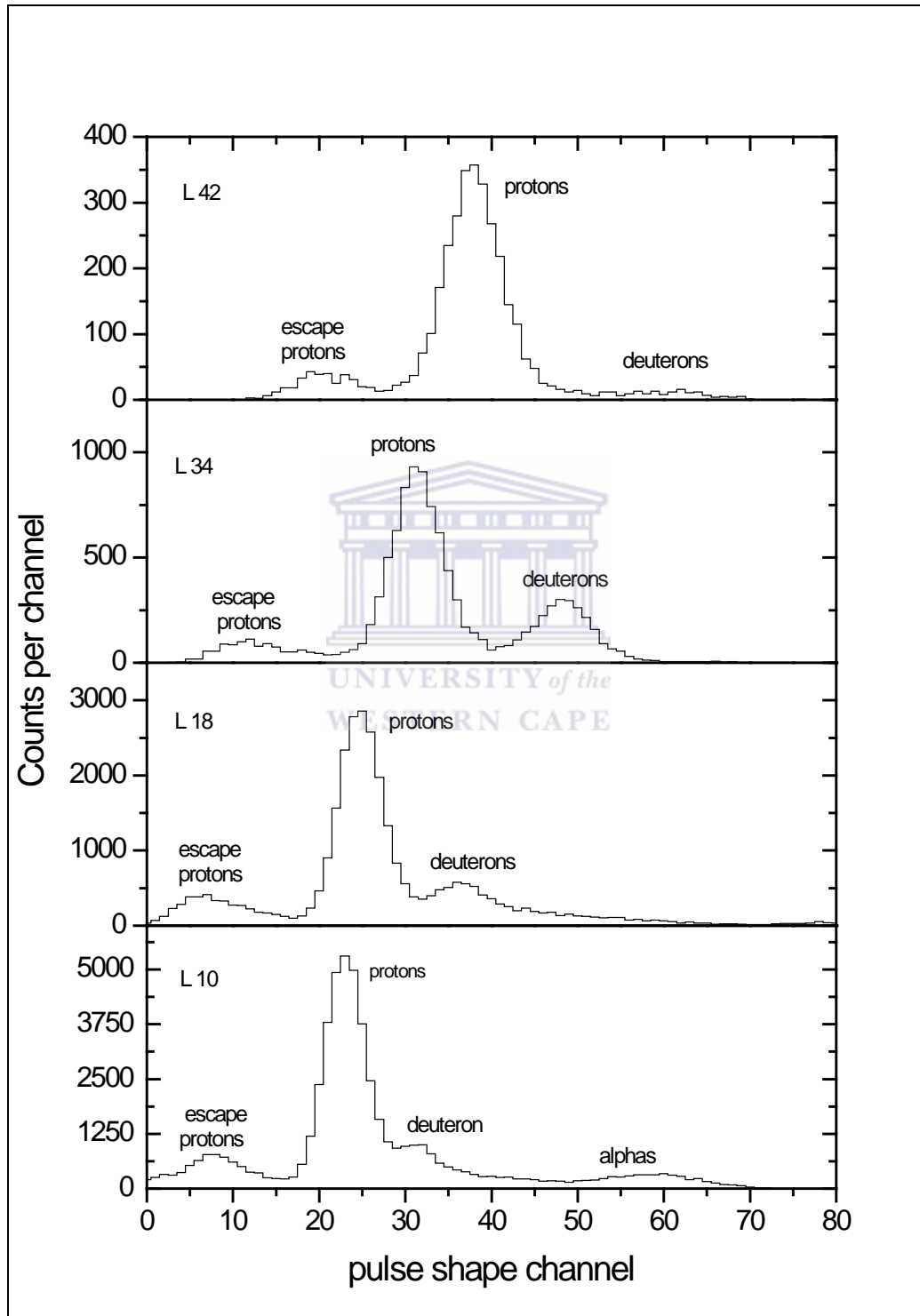
Figure 4. 8: *Pulse shape spectra measured with the NE213 spectrometer for neutrons produced by bombarding a (1 mm) ^7Li with 66 MeV protons, pulse shape spectra collected at different pulse height bins.*

43
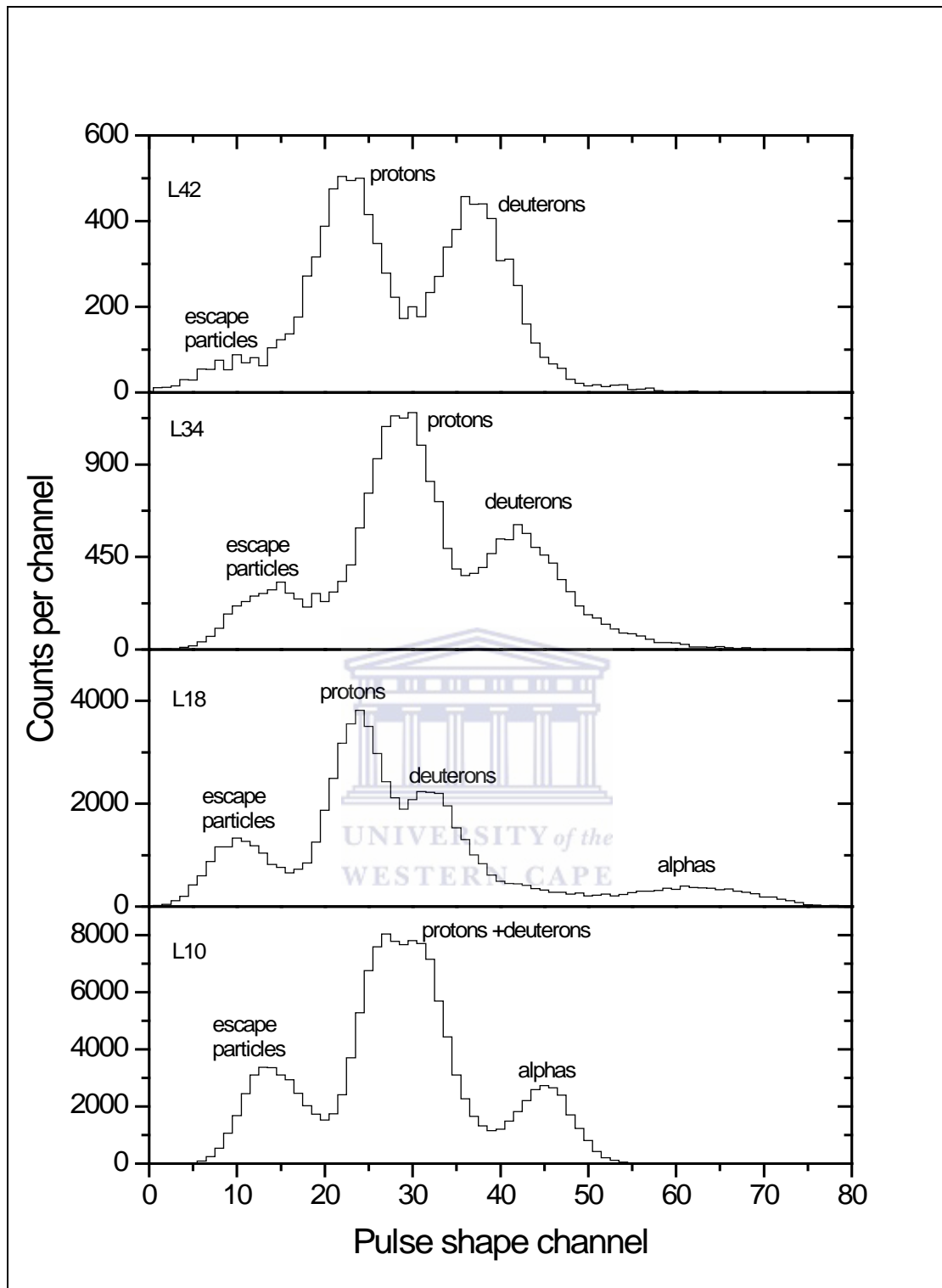
Figure 4. 9: *Pulse shape spectra measured with the NE230 spectrometer for neutrons produced by bombarding a (1 mm) ^7Li with 66 MeV protons, pulse shape spectra collected at different pulse height bins.*

4.3   Pulse height spectra

Figure 4.10 shows a perspective plot of counts (vertical) as a function of neutron ToF T (ADC channel) and pulse height L (ADC channel) for all neutron energy range (5-64 MeV) produced by bombarding Li-target with 66 MeV proton beam. The ToF parameter T relates to neutron energy (as discussed in 4.1.2), while pulse height parameter L relates to the energy of the recoiling charged particle in the scintillator. Main features shown in fig 4.10 (a) are the ridges at lower time-of-flight, marking proton events from n-p elastic scattering events in the scintillator, the pulse height limit can be clearly seen at the left of the LT-plot. The maximum energy of these recoiling protons is equal to that of incident neutron energy. With an increasing time-of-flight, the contribution of protons from n-C reactions increase and can be seen more to the right of the LT plot, the second ridge at lower pulse height is associated with the pulse height limit for protons produced in the n-C reactions. The sharp ridge at the far right corresponds to neutrons of energy 64 MeV produced from ^{7}Li(p,n)^{7}Be$_{gs}$ reaction. Ridges from n-p and n-C events are distinguishable at lower ToF, however due to escaping protons the ridges become less distinguishable at higher ToF channels.

Main features in fig 4.10 (b) are the ridges at lower pulse height and clearly seen at lower neutron ToF, marking recoiling deuterons from n-d elastic scattering events in the scintillator, the maximum energy of these deuterons is eight-ninth of the incident neutron energy (see appendix C). As in the case with measurements using the NE213 spectrometer, the contribution due to n-C reactions increases with increasing neutron time-of-flight, with the second ridge associated with deuterons produced from n-C reactions at lower pulse height. The ridges due to n-d elastic scattering and n-C reactions events are distinguishable at lower neutron ToF, however tend to be less distinguishable at higher ToF due to deuteron escape. The sharp ridge corresponds to 64 MeV neutrons produced from ^{7}Li(p.n)^{7}Be$_{gs}$ reaction.

Energy bins that could resolve both, the structures attributed to ^{12}C resonances associated with 6.5 cm graphite blocks placed in front of the collimator facing the target, and the peak at 64 MeV in the lithium energy spectrum, were chosen. Equation 4.6 was solved for ToF channel corresponding to both upper and lower limit for the bins centered at incident neutron energies of interest and are presented in table 4.2.
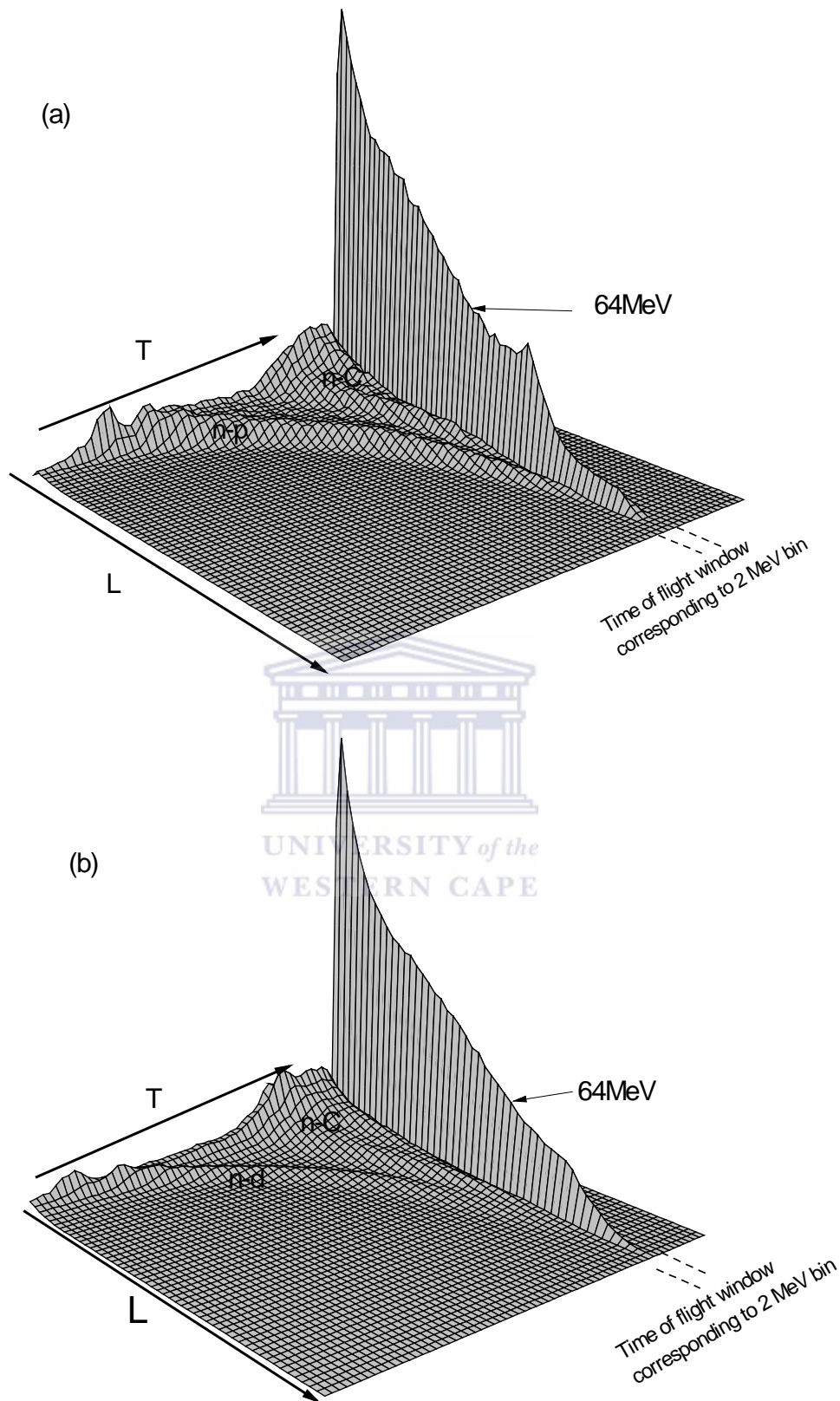
Figure 4. 10: Perspective plot of counts (vertical) as a function of ToF T (ADC channels) and pulse height L (ADC channel), measured with (a) the NE213 spectrometer and (b) the NE230 spectrometer, for neutrons produced by bombarding a ^{7}Li target with 66 MeV proton beam.

Table 4. 2: Incident neutron energy bin width with their corresponding neutron ToF windows used in this work for pulse height spectra measured with the NE213 spectrometer.

Centre energy E_n (MeV)	Energy bin limit (MeV)		Neutron ToF window (ADC channels)	
	Lower	Upper	Lower	Upper
10	9	11	654	801
12	11	13	801	913
14	13	15	913	1001
16	15	17	1001	1073
18	17	19	1073	1133
20	19	21	1133	1185
22	21	23	1185	1229
24	23	25	1229	1268
26	25	27	1268	1303
28	27	29	1303	1334
30	29	31	1334	1361
32	31	33	1361	1386
34	33	35	1386	1409
36	35	37	1409	1430
38	37	39	1430	1450
40	39	41	1450	1467
42	41	43	1467	1484
44	43	45	1484	1499
46	45	47	1499	1514
48	47	49	1514	1527
50	49	51	1527	1540
52	51	53	1540	1552
54	53	55	1552	1563
56	55	57	1563	1574
58	57	59	1574	1584
60	59	61	1584	1594
62	61	63	1594	1603
64	63	65	1603	1611
66	65	67	1611	1620

As an example of energy bins used in this work to obtain pulse height spectra, a ToF window (corresponding to 2 MeV energy bin) set at the sharp peak in the *LT*-plot for 64 MeV neutrons produced from the ^{7}Li(p,n)^{7}Be$_{gs}$ reaction is shown in figure 4.10 (a). Pulse height spectra for up to 29 neutron energies depending on the target were obtained by projecting events in each ToF window of equal energy bins (2 MeV) on the *LT*-plot onto the *L*-axis,

with LS-cuts (C_1 and C_2) imposed on the data to select only proton events. A pulse height spectrum measured with the NE213 spectrometer is shown in figure 4.11.

There are two main contributions in the pulse height spectrum, scintillation pulses resulting from charged particles produced from n-C reactions and protons resulting from n-p elastic scattering. Also shown in figure 4.11 are the upper pulse height limits for both protons from n-C reactions and most energetic protons (n-p elastic scattering). Shown in figures 4.12-4.15 are all proton pulse height spectra at incident neutron energies used in this work, measured with NE213 for the sum of all targets (sum target).

The peak labelled P_{np} is attributed to forward recoiling protons from n-p elastic scattering events, and the peak labelled P_c is attributed to protons from n-^{12}C reactions. Only protons from n-p elastic scattering are associated with the peak P_{np} at energies 10-20 MeV, this is since protons produced from n-C reactions in this range have the energy less than the electronic threshold of 5 MeV which was set for measurements. As the energy increases the peak P_{np} shifts towards the right (higher pulse heights), due to the relation of pulse height to particle energy.

The peak P_c resulting from protons produced from the ^{12}C(n,p)^{12}B reaction becomes more visible as the incident neutron energy increases. The peak P_c tends to shift to the right (higher pulse heights) which is consistent with kinematics of the reaction. As the incident neutron energy increase the event counts associated with both peaks tends to decrease. This is attributed to the range of protons which increases with neutron energy, thus increasing the proton escape. For proton energies 20 MeV, 40 MeV, and 60 MeV the range of protons in the NE213 scintillator were calculated to be 0.478 cm, 1.678 cm, and 3.491 cm respectively, which implies 12%, 42%, and 81% of protons will escape the scintillator before depositing all their energy (refer to table 5.2). The proton escape factor was corrected for in the calculation of neutron fluence in section 5.1.2.
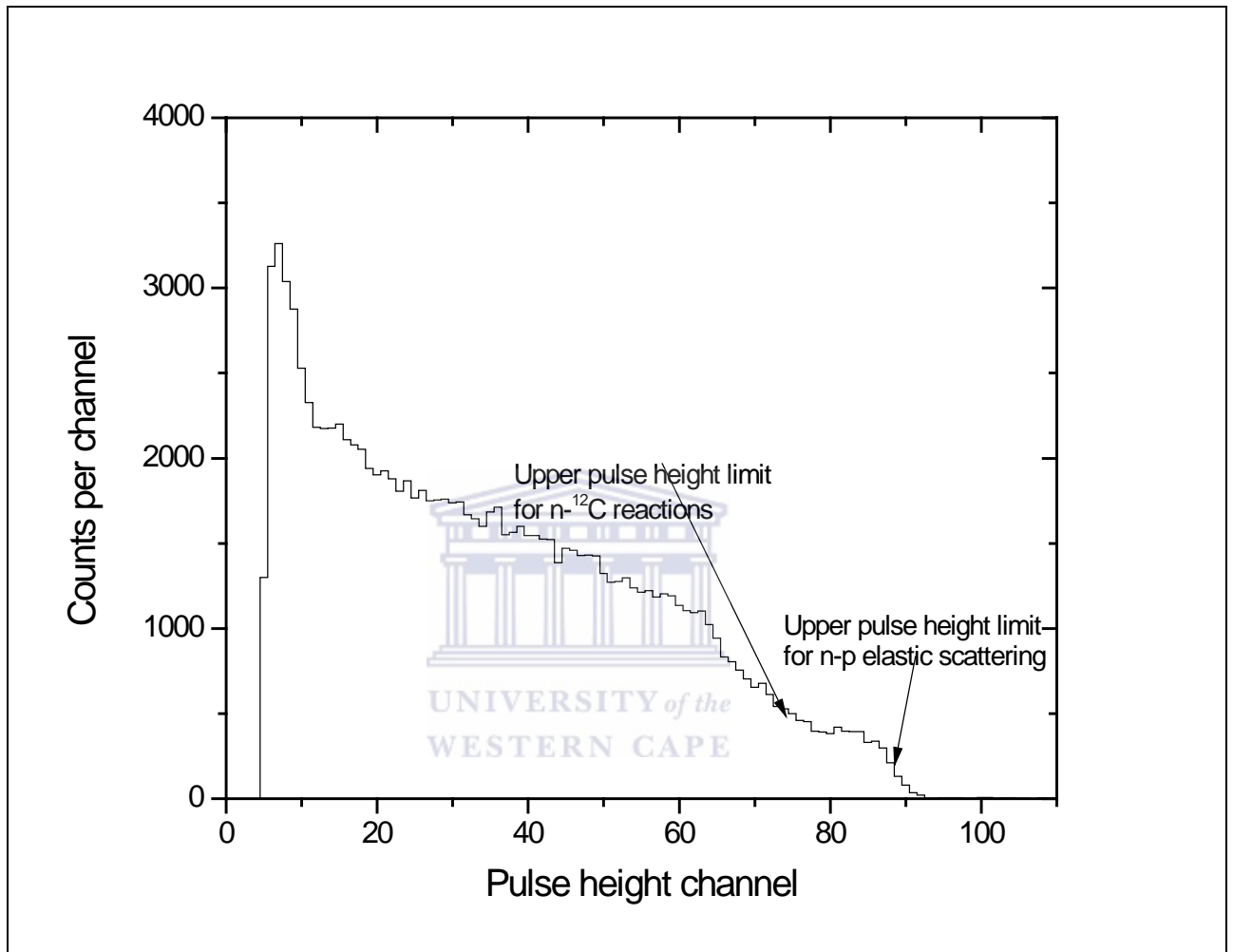
Figure 4. 11: *Pulse height spectrum with its proton component used for measurements in this work, for incident neutron energy of 64 MeV for sum target (Li, Be, and C) measured with The NE213 spectrometer.*
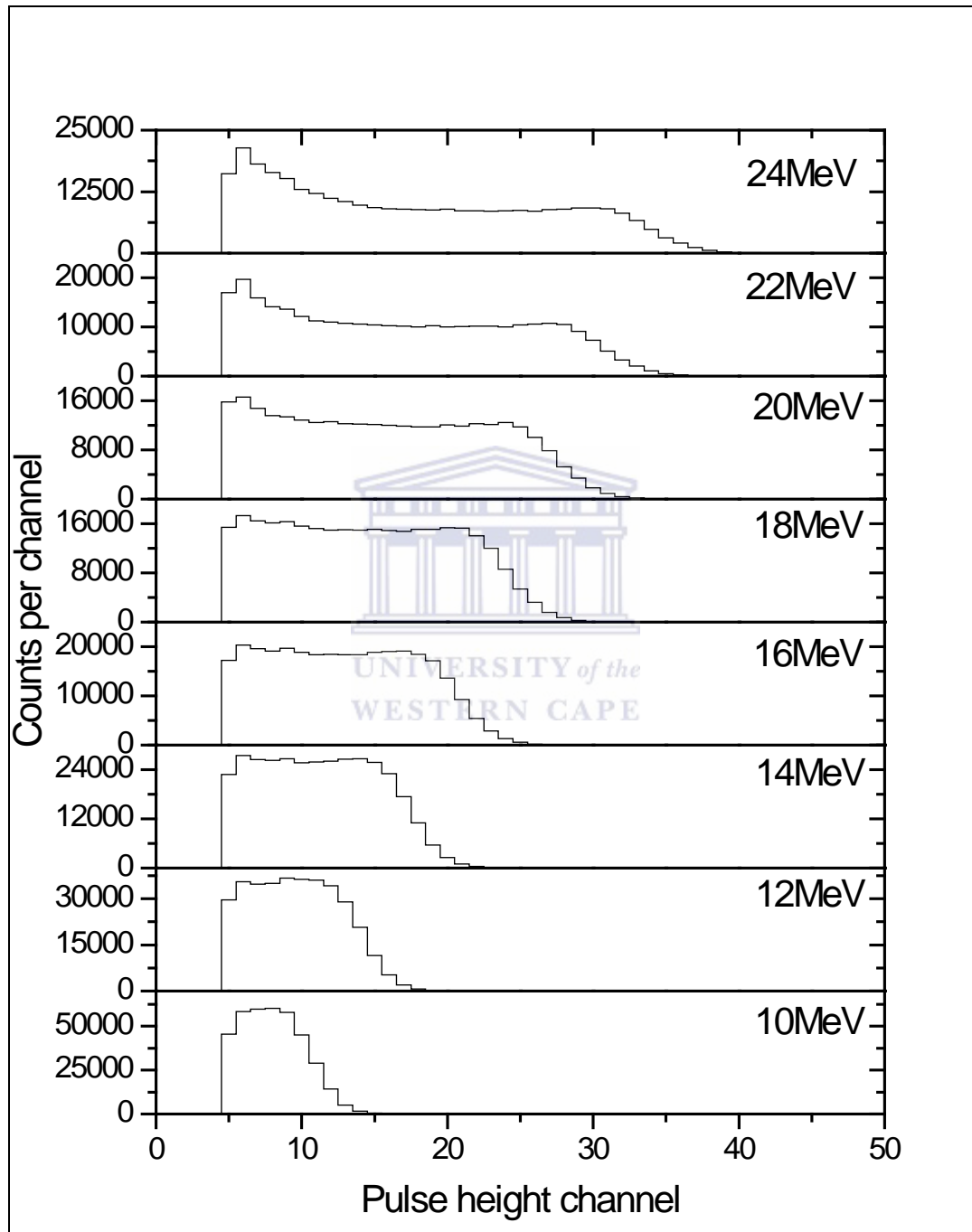
Figure 4. 12: *Pulse height spectra for proton events of incident neutron energy 10-24 MeV measured with the NE213 spectrometer, spectra produced for a sum target (Li, Be, and C).*
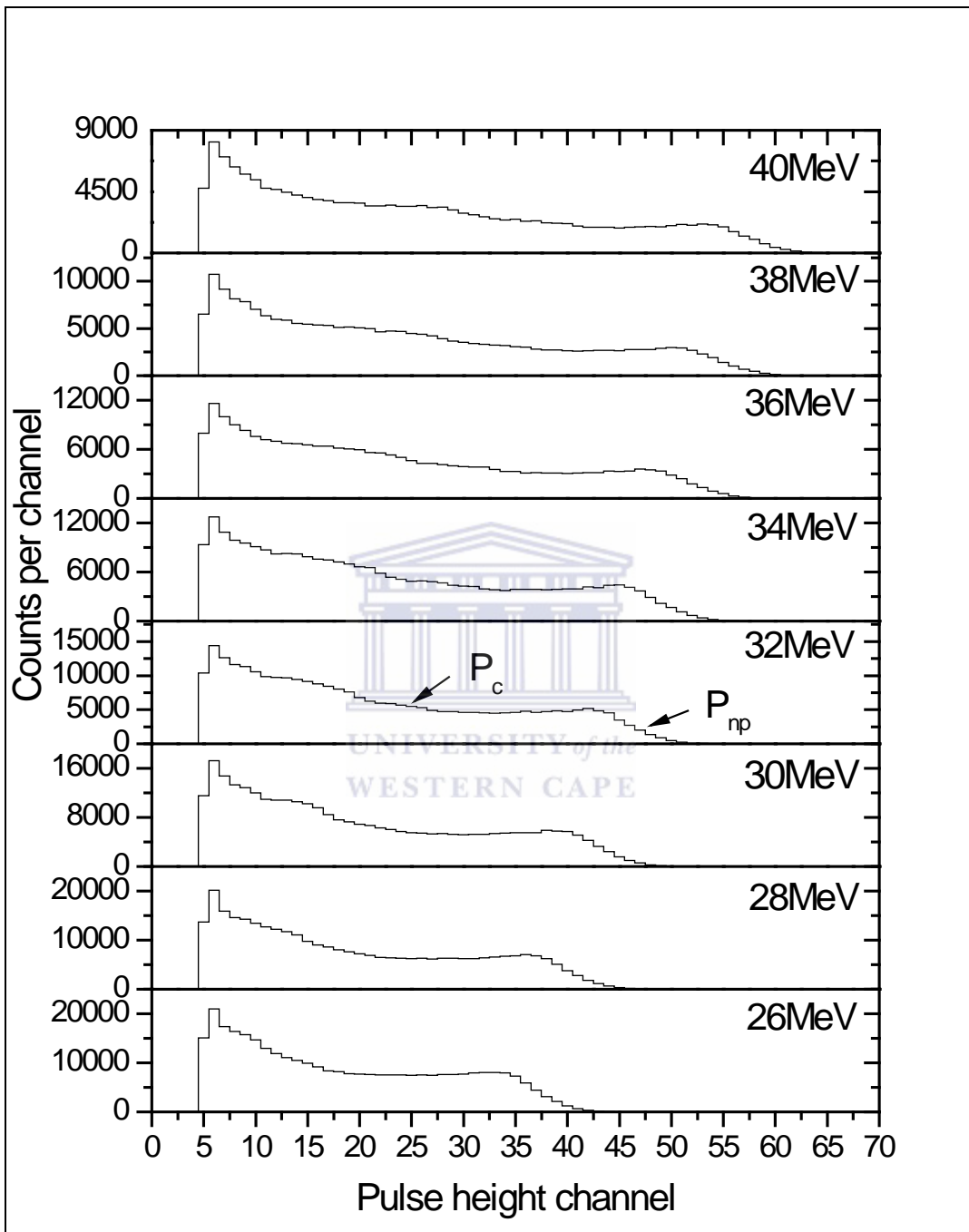
Figure 4. 13: *Pulse height spectra for proton events of incident neutron energy 26-40 MeV measured with the NE213 spectrometer, spectra produced for a sum target (Li, Be, and C).*
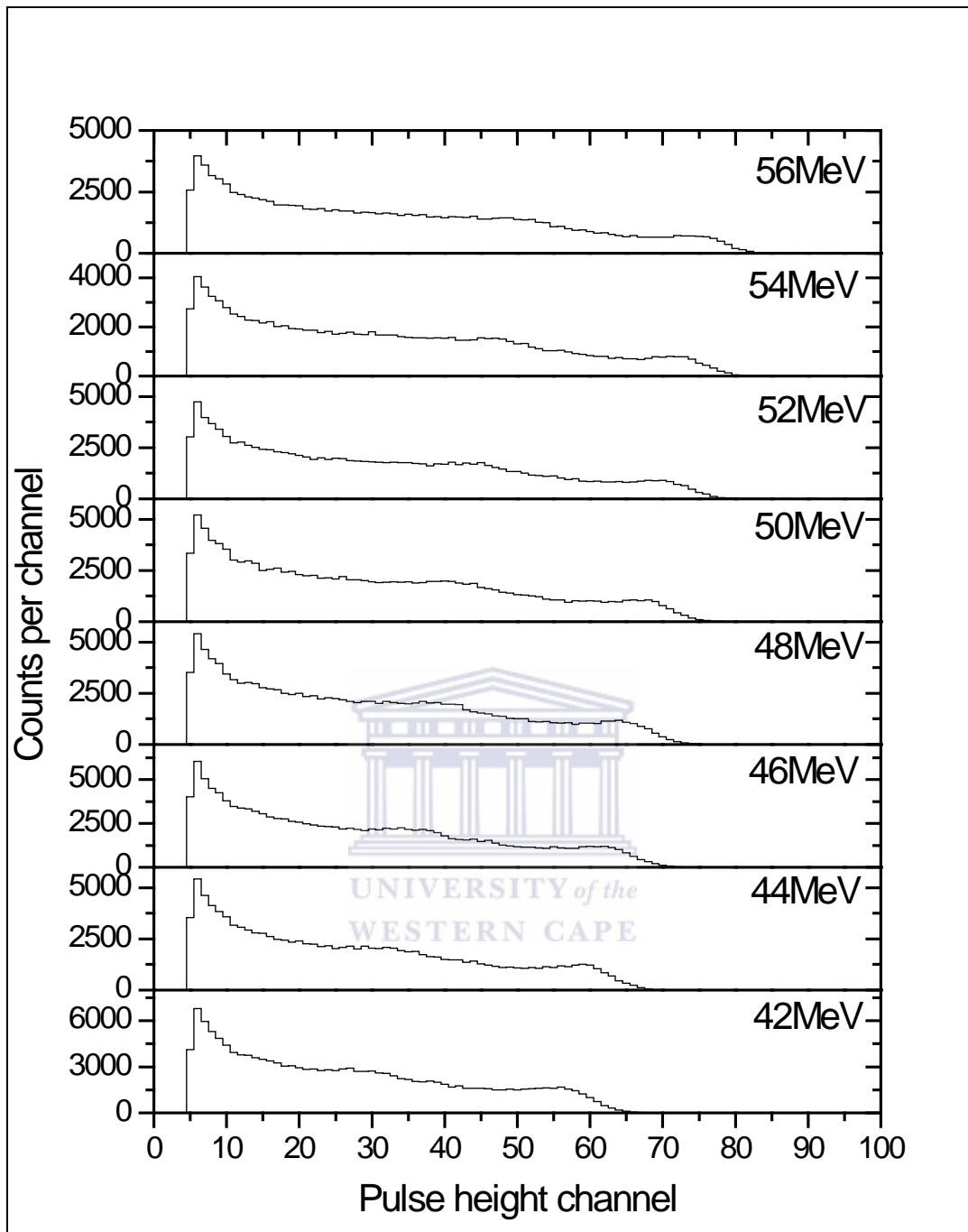
Figure 4. 14: *Pulse height spectra for proton events of incident neutron energy 42-56 MeV measured with the NE213 spectrometer, spectra produced for a sum target (Li, Be, and C).*

52
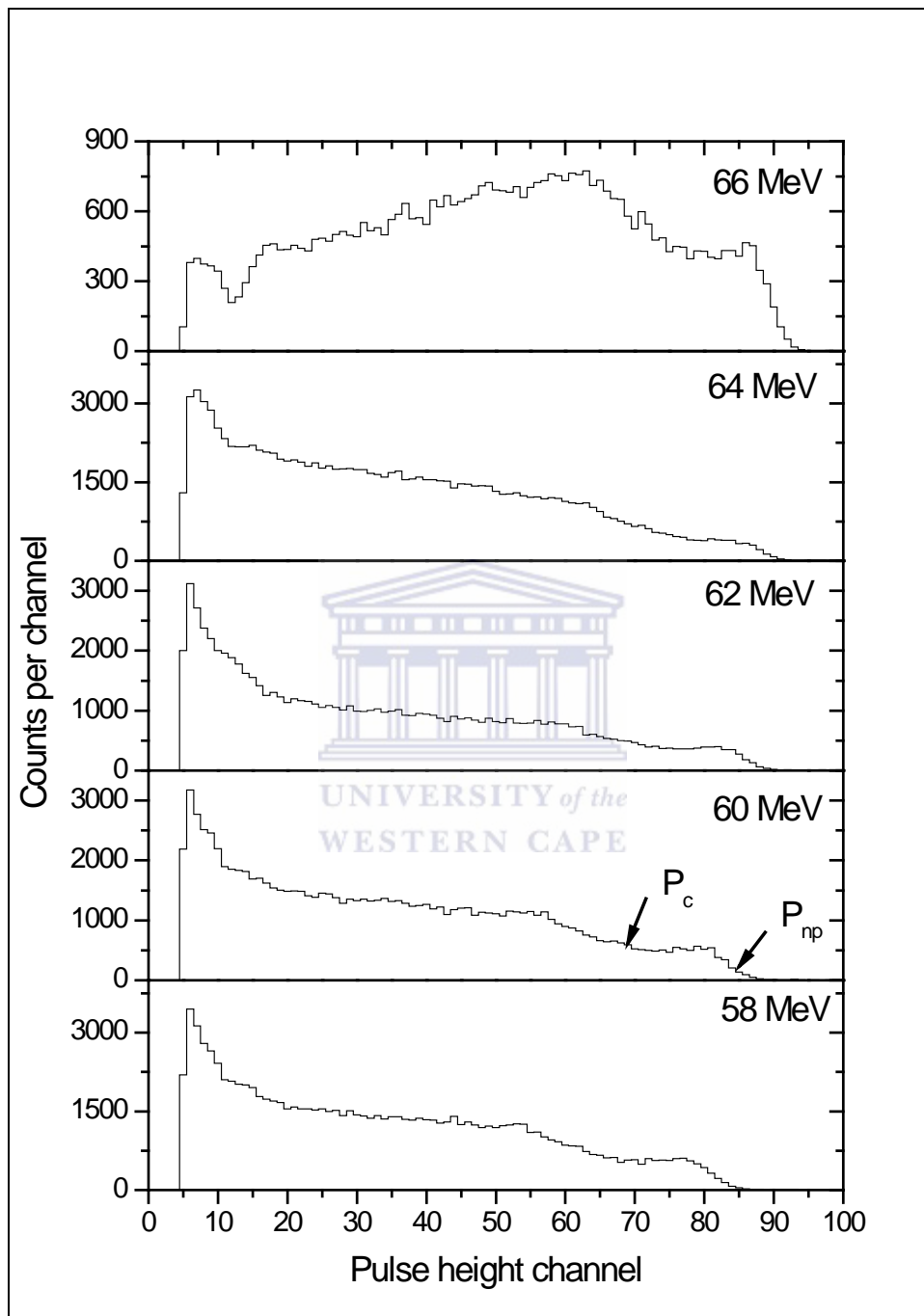
Figure 4. 15: *Pulse height spectra for proton events of incident neutron energy 58-66 MeV measured with the NE213 spectrometer, spectra produced for the sum target (Li, Be, and C).*

Pulse height spectra measured with the NE230 spectrometer were obtained similarly to those measured with the NE213 spectrometer. Energy bins of 2 MeV where chosen as these bins could resolve the resonance structures associated with the 6.5 cm graphite block as described in section 4.1.1 and the 64 MeV peak in the lithium energy spectrum. Equation 4.6 was solved for corresponding ToF channel windows using the calibration data measured with the NE230 spectrometer (see fig 4.2) and are shown in table 4.3. An example of a ToF window (corresponding to 2 MeV) set in the *LT*-plot at the sharp peak for 64 MeV neutrons is shown in fig 4.10 (b). The ToF windows corresponding to equal bin widths of 2 MeV were set on the LT data for up to 29 neutron energies of interest (refer to table 4.3). Pulse height spectra for up to 29 neutron energies were obtained by projecting events in these ToF windows onto the *L*-axis (see figure 4.11 (b)), with the *LS*-cuts (C_3 and C_4) imposed on the data to select only deuteron events.

Figure 4.16 shows pulse height spectrum measured with the NE230 spectrometer for the sum target, chosen for good statistics. Two main components can be seen in the pulse height spectrum (fig 4.16), scintillation pulse height events produced from n-C reactions and scintillation pulse height events due to recoiling deuterons from n-d elastic scattering as indicated in figure 4.1.6. Pulse height spectra measured with the NE230 spectrometer are shown in figures 4.17-4.20. The peak labelled D_{nd} is attributed to forward recoiling deuterons from n-d elastic scattering, and the peak labelled D_c is attributed to deuterons resulting from n-^{12}C reactions. The peak D_{nd} is visible and distinguishable especially at low to intermediate neutron energies (10-40 MeV). The peak shifts towards higher pulse height as the neutron energy increases, which is expected since forward recoiling protons increase with increase neutron energy due to elastic scattering. The peak, however, diminishes at higher neutron energies (42-66 MeV).

The peak D_c associated with deuterons resulting from n-^{12}C reactions is not seen at low neutron energies (10-20 MeV), this may be attributed to that at this neutron energy range, deuterons produced from these reactions fall below the threshold energy set for measurements (5 MeV). At higher neutron energies, the peak D_c mainly due to deuterons produced from ^{12}C(n,d)^{11}B reaction becomes visible. As the neutron energy increases the peak D_c shifts towards higher pulse heights until it overlaps with events associated with the peak D_{nd}.

Table 4. 3: Incident neutron energy bin width with their corresponding neutron ToF windows used in this work for pulse height spectra measured with the NE230 spectrometer.

Centre energy E_n (MeV)	Energy bin limit (MeV)		Neutron ToF window (ADC channels)	
	Lower	Upper	Lower	Upper
10	9	11	701	848
12	11	13	848	960
14	13	15	960	1048
16	15	17	1048	1120
18	17	19	1120	1180
20	19	21	1180	1232
22	21	23	1232	1276
24	23	25	1276	1315
26	25	27	1315	1350
28	27	29	1350	1381
30	29	31	1381	1408
32	31	33	1408	1433
34	33	35	1433	1456
36	35	37	1456	1477
38	37	39	1477	1497
40	39	41	1497	1514
42	41	43	1514	1531
44	43	45	1531	1546
46	45	47	1546	1561
48	47	49	1561	1574
50	49	51	1574	1587
52	51	53	1587	1599
54	53	55	1599	1610
56	55	57	1610	1621
58	57	59	1621	1631
60	59	61	1631	1641
62	61	63	1641	1650
64	63	65	1650	1658
66	65	67	1658	1667

This is attributed to the kinematic effect (see fig 4.22) which results in the faster energy increase of deuterons produced from the ^{12}C(n,d)^{11}B reaction compared to eight-ninth of the forward recoiling deuterons from n-d elastic scattering. It can also be seen that both the peaks D_C and as previously mentioned D_{nd} diminish with increasing neutron energy. The range of deuterons in the NE230 scintillator for 20 MeV, 40 MeV, and 60 MeV is 0.18 cm, 0.64 cm, and 1.33 cm respectively, this implies that 9%, 32%, and 64% of deuterons escape the detector at these energies (see table 5.5) . As with NE213 measurements, the escape effect for

deuterons in the NE230 scintillator was corrected for in the neutron fluence calculations using n-d elastic scattering events in section 5.2.2.
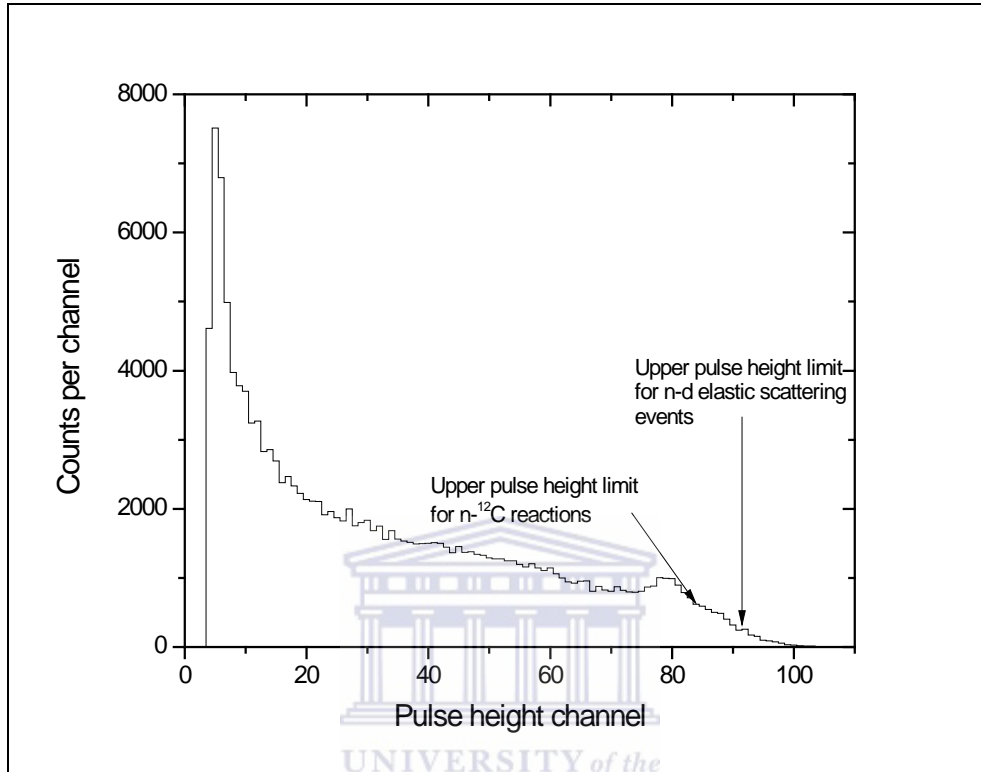
Figure 4. 16: *Pulse height spectrum with its deuteron component used for measurements in this work, for incident neutron energy of 64 MeV for sum target (Li, Be, and C) measured with the NE230 spectrometer.*
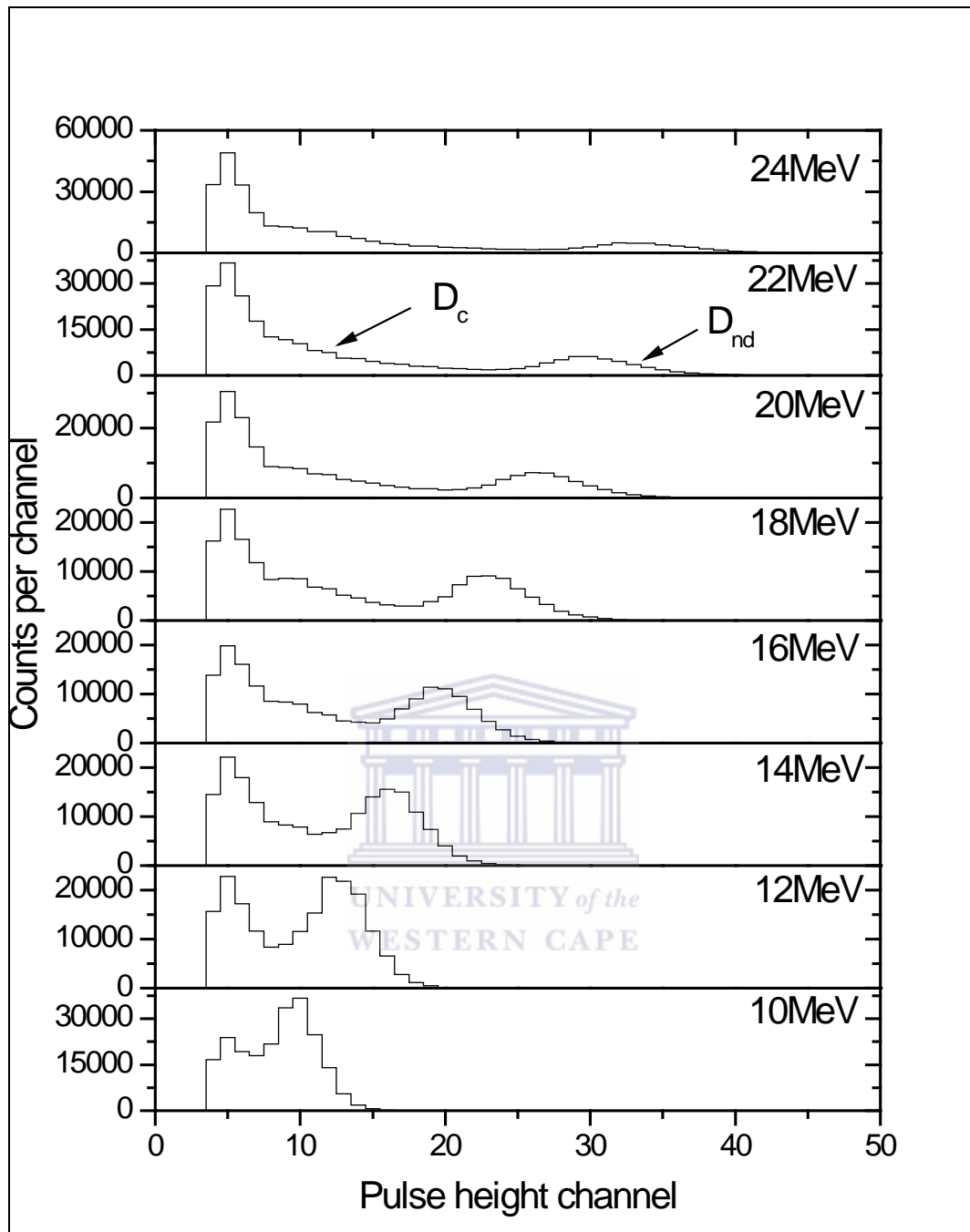
Figure 4. 17: *Pulse height spectra for deuteron events of incident neutron energy 10-24 MeV measured with the NE230 spectrometer, spectra produced for the sum target (Li, Be, and C).*
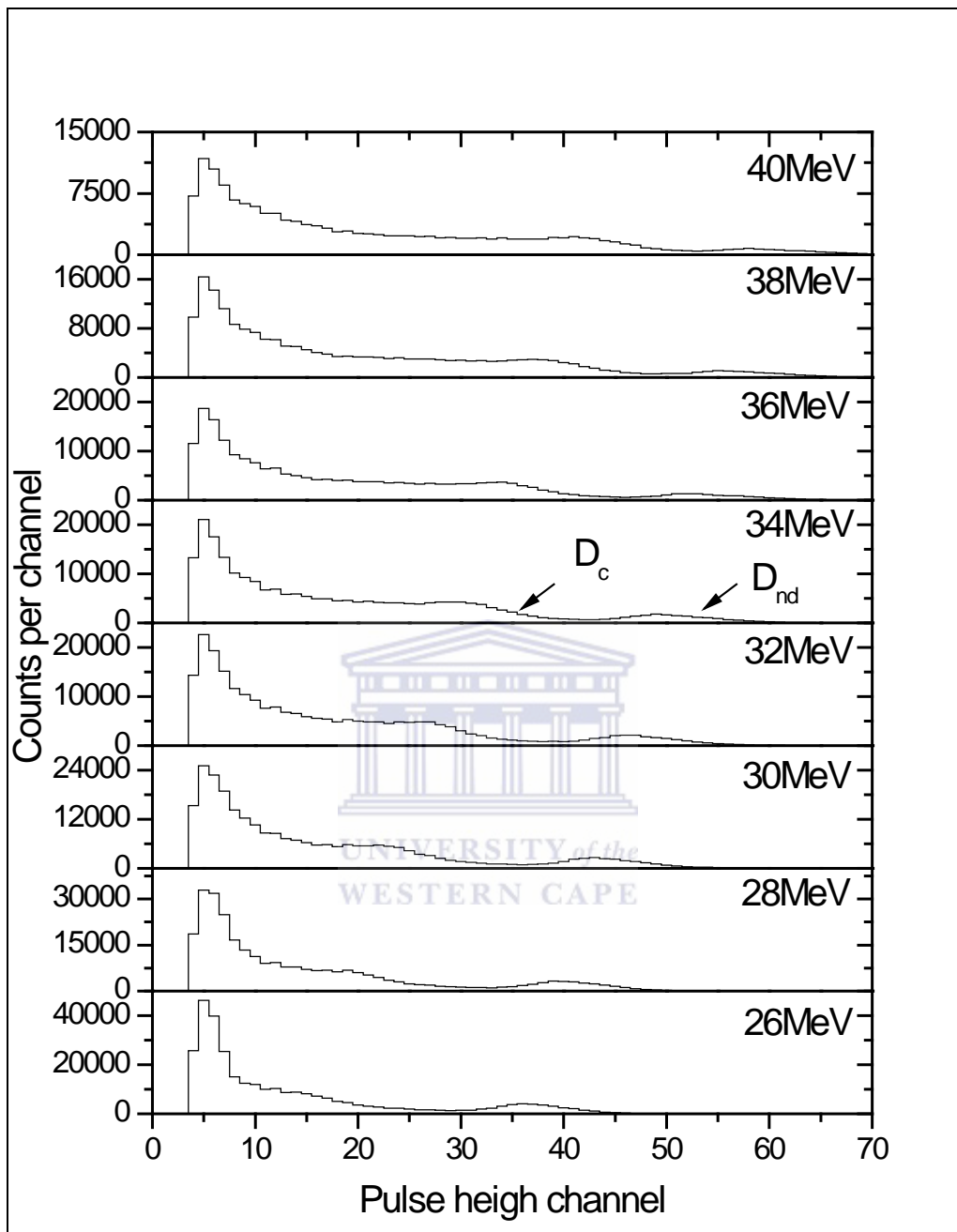
Figure 4. 18: *Pulse height spectra for deuteron events of incident neutron energy 26-40 MeV measured with the NE230 spectrometer, spectra produced for the sum target (Li, Be, and C).*
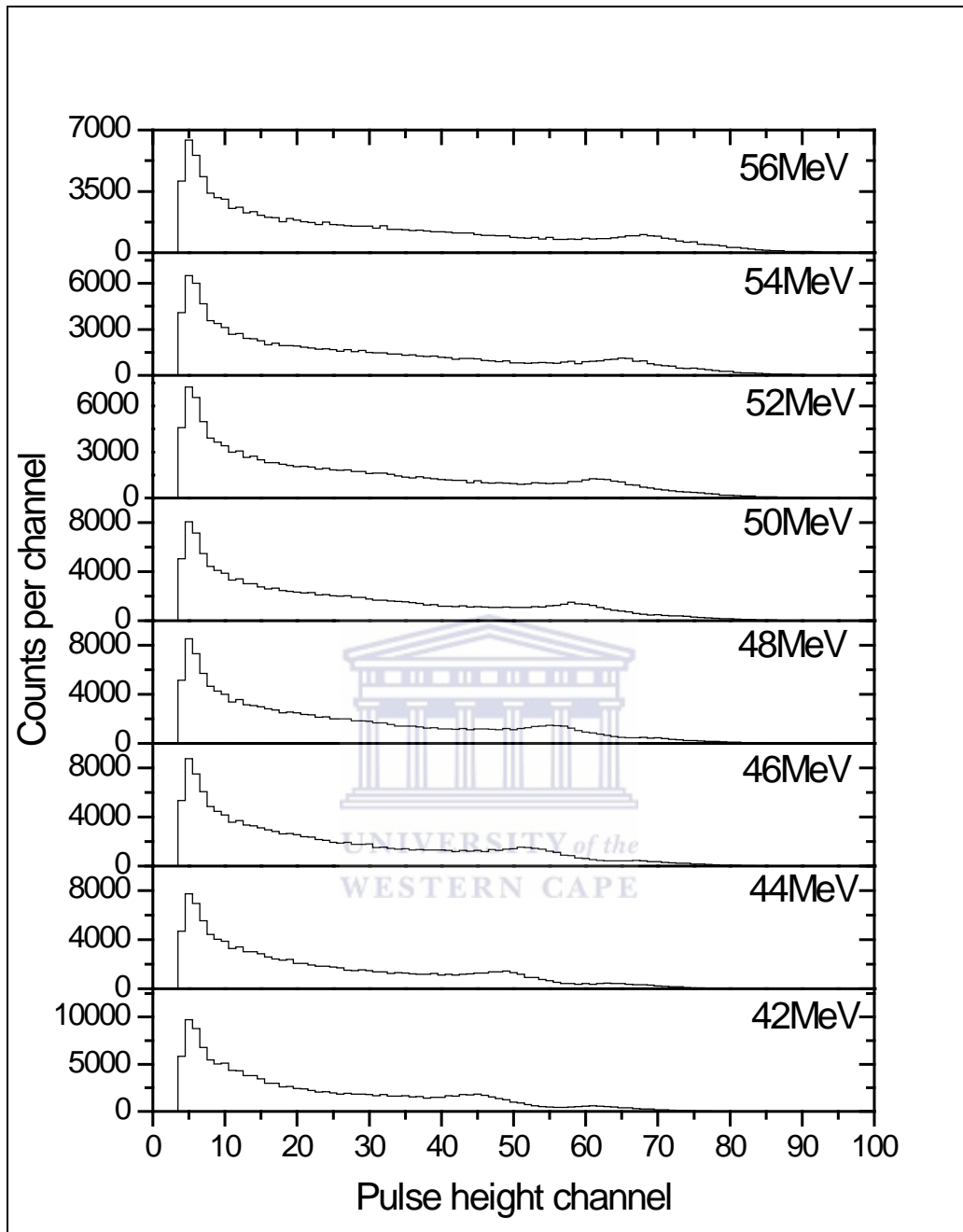
Figure 4. 19: *Pulse height spectra for deuteron events of incident neutron energy 42-56 MeV measured with the NE230 spectrometer, spectra produced for the sum target (Li, Be, and C).*
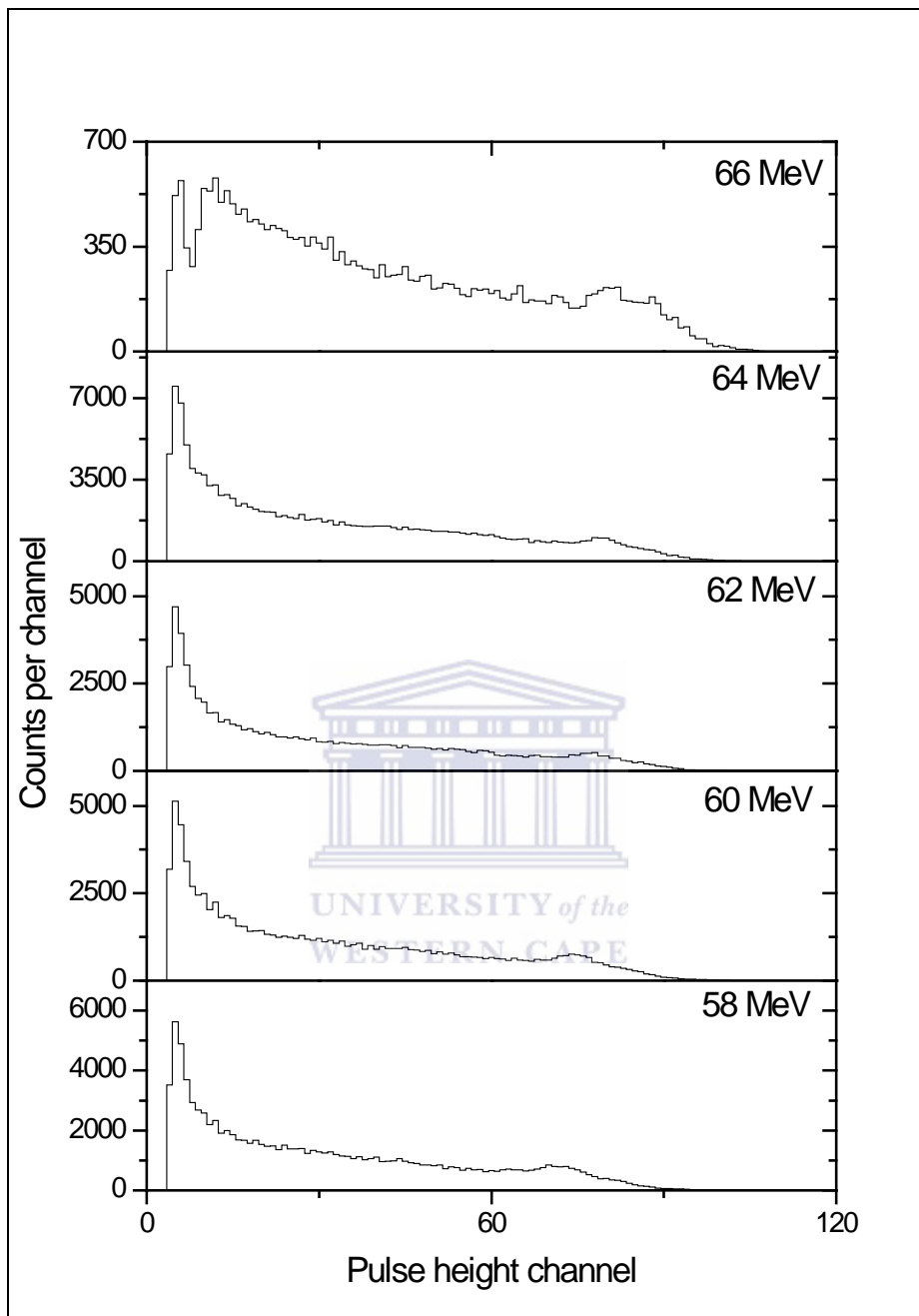
Figure 4. 20: *Pulse height spectra for deuteron events of incident neutron energy 58-66 MeV measured with the NE230 spectrometer, spectra produced for the sum target (Li, Be, and C).*

4.4   Selection of events

Figure 4.21 shows a proton pulse height spectrum for neutrons of 64 MeV, chosen due to good counting statistics, however most aspects of the discussion made in reference to this spectrum also apply to pulse height spectra of lower incident neutron energies. The upper pulse height limit (L_{np}) due to recoiling protons from the n-p elastic scattering was assumed to be half height of the abrupt edge of the proton pulse height spectrum [Makupula, 2003], the broadening of the edge is due to the detector resolution. The pulse height L_{np} corresponds to maximum proton energy equal to incident neutron energy (see appendix C). Figure 4.22 shows the plot of proton energy as a function of pulse height (ADC channels), also included is the fit to the data (solid line) used as proton to pulse height calibration curve with a form of Equation 4.9.

$$L(E_p) = -7.577 + 1.853E_p - 0.006E_p^2. \tag{4.9}$$

The non-linear relation of the response, $L(E)$, to protons may be described by the relations such as Birks relation [Birks, 1964] [Brooks, 1979], attributed due to quenching effect and space charge saturation [Buffler, 1991] which was not corrected for in this work. The most energetic protons arising from n-C reactions are produced from ^{12}C(n,p)^{12}B reaction with the Q-value calculated to be -12.587 MeV [NNDC]. Using this Q-value, the maximum energy of protons E_c for the reaction was calculated for neutron energies of interest (10-64 MeV). The proton energy E_c corresponds to the upper pulse height limit (L_c) for protons resulting from n-C reactions in the proton pulse height spectrum (refer to fig 4.21). Together with Eq. 4.9, L_c values for each pulse height spectrum were estimated, all events above L_c were taken to be associated with n-p elastic events in the proton pulse height spectra. The L_c values from the fit becomes less reliable at lower neutron energies ($E_n < 20\ MeV$), thus at this range it becomes increasingly difficult to estimate the L_c values, to overcome this challenge the maximum proton energies were calculated using non relativistic kinematic equations (fig 4.23 (a) and appendix C). At neutron energies $E_n < 16\ MeV$ all events are attributed to n-p elastic scattering, at this range the outgoing particles were calculated to have energy below the electronic threshold of 5 MeV (see section 3.4).
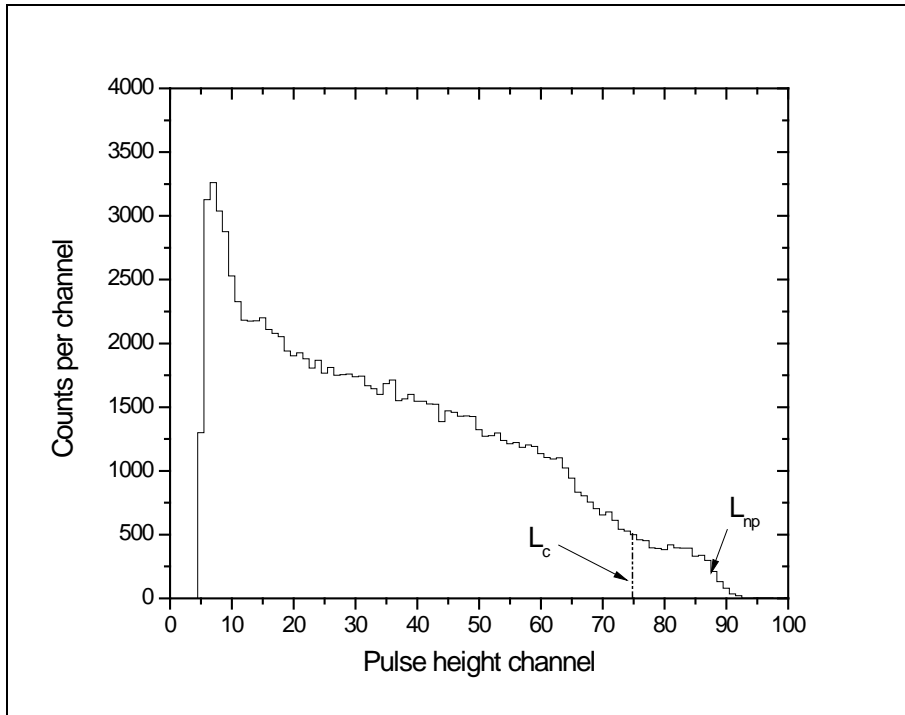
Figure 4. 21: *Pulse height spectrum measured with NE213 for 64 MeV neutrons, including the upper pulse height limits for n-^{12}C reactions and n-p elastic scattering.*
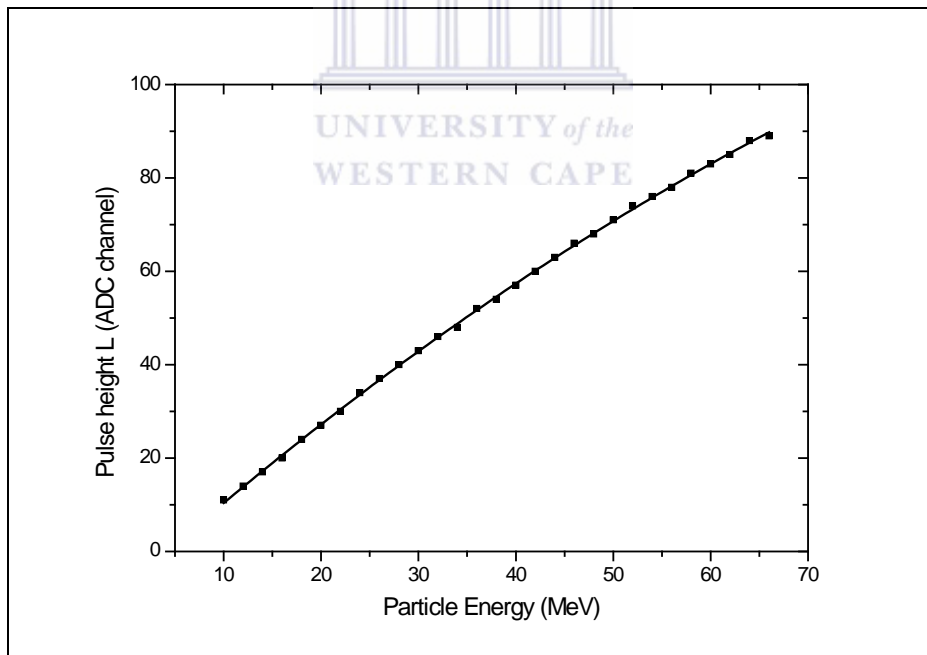
Figure 4. 22: *Pulse height in ADC channels as a function of proton energy, with the best fit (solid line) to the data measured with the NE213 spectrometer*
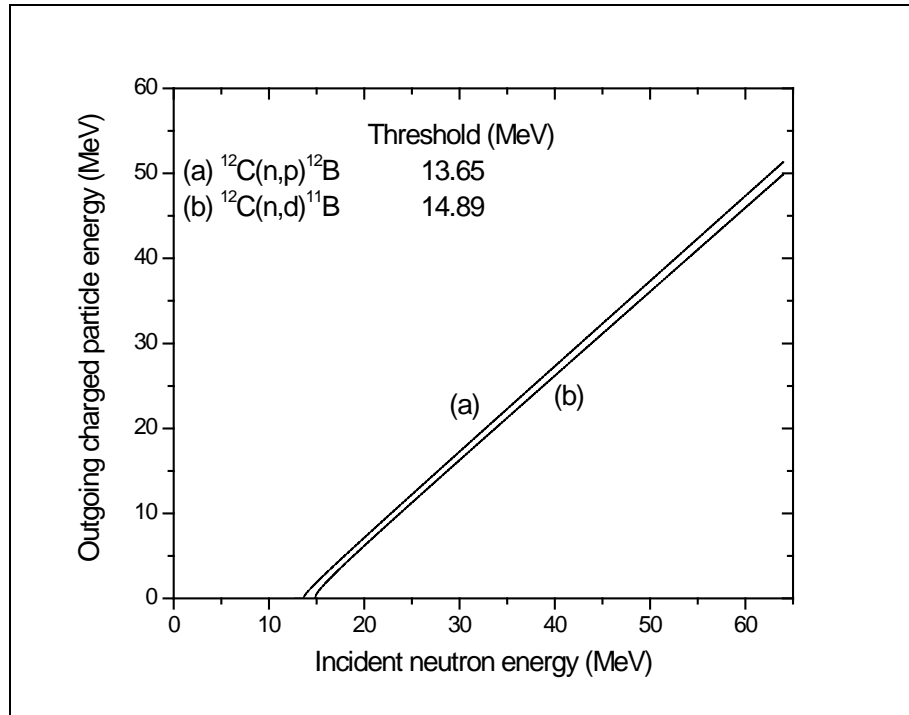
Figure 4. 23: *Maximum energy limit for outgoing charged particles produced from (a)* $^{12}C(n,p)^{12}B$ *and (b)* $^{12}C(n,d)^{11}B$, *calculated using standard kinematics equations (see appendix C.)*

At neutron energies E_n = 18 – 20 MeV most contribution is due to n-p elastic scattering events, the L_c values were slightly adjusted to the small detectable contribution of protons from n-C reactions.

Figure 4.24 shows the pulse height spectrum measured with NE230 for 64 MeV neutrons. Discussion with reference to this spectrum is applicable to pulse height spectra at lower neutron energies. The spectrum is characterized by deuterons produced from n-C reactions and n-d elastic scattering. Similar to pulse height spectra measured with NE213, the upper pulse height limit (L_{nd}) of recoiling deuterons from n-d elastic scattering was assumed to be half height of the abrupt edge (refer to fig 4.24), with broadening due to detector resolution. The deuterons were calculated to have a maximum energy of eight-ninth of the incident neutron (see appendix C). The pulse height L_{nd} at different neutron energies (10-64 MeV) as a function of deuteron energy give a calibration curve of pulse height to deuteron energy. Shown in figure 4.25 is the pulse height as a function of deuteron energy, with the best fit curve to the data (solid line) which is describe by equation 4.10

$$L(E_d) = 3.444 + 0.209E_d + 0.108E_d^2 - 0.002E_d^3 + 1.647E_d^4 \qquad (4.10)$$

63
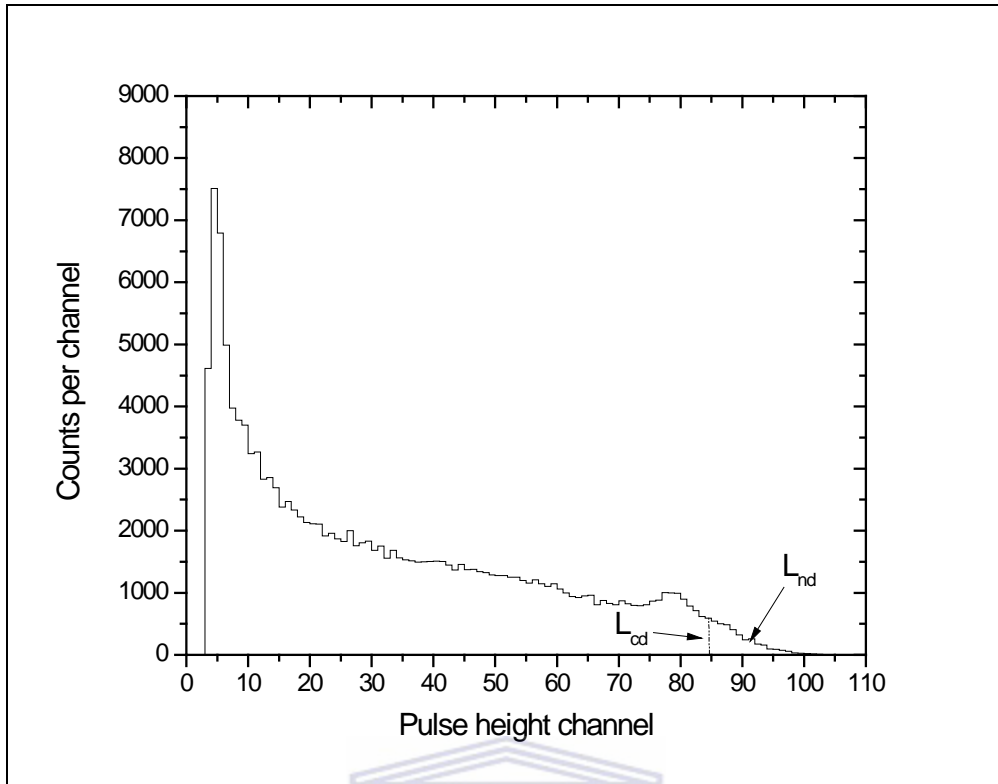
Figure 4. 24: *Pulse height spectrum for deuteron events selected by the corridor C_4 and C_5 on the LS plot measured with the NE230 spectrometer, at incident neutron energy of 64 MeV.*
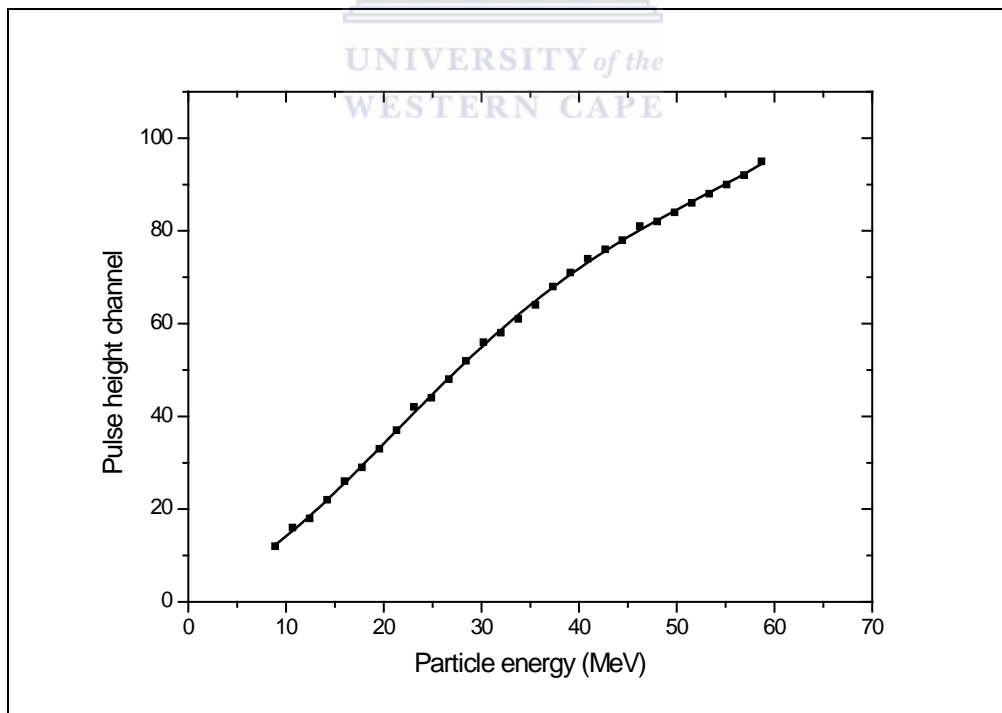
Figure 4. 25: *Pulse height in ADC channels as a function of deuteron energy, with the best fit (solid line) to the data measured with the NE230 spectrometer.*

From Eq.4.10, the response of NE230 to deuteron has greater non-linear dependence than the response of NE213 to protons, which can in addition to quenching and space charge saturation which was not corrected for in this work, also be attributed to a greater charge of deuterons than protons [Brooks, 1979].

Most energetic deuterons from the n-^{12}C reactions were produced by ^{12}C(n,p)^{12}B reaction, with the lowest Q-value for production of deuterons calculated to be -13.732 MeV for this reaction [NNDC]. The energy E_{cd} calculated using the Q-value of the reaction corresponds to the upper pulse height limit (L_{cd}) for deuterons resulting from n-C reaction (refer to fig 4.24). Together with values calculated using Eq. 4.10, L_{cd} values were estimated in the pulse height spectra. Events above L_{cd} are attributed to n-d elastic scattering events and those below L_{cd} to n-C reactions. At lower neutron energies (10-20 MeV), the calculated L_{cd} values are less reliable, however at these energies there is less to no contribution of deuterons resulting from n-^{12}C reactions, all events at energy range ($E_n < 18\ MeV$) are due to n-d elastic scattering, with outgoing charge particle energy calculated to be below the electronic threshold of 5 MeV (fig 4.23 (b)), at neutrons energy 20 MeV major contribution is due to n-d elastic events, however there is a small detectable contribution of deuterons from the n-^{12}C reaction, thus a slight adjustment to the selection of L_{cd} was made in the estimation of this value. Due to increasing deuteron escape effect with increasing particle energy (deuteron), separation between deuteron from n-d elastic scattering events and n-C reactions becomes increasingly difficult.

5   CALCULATION OF NEUTRON FLUENCE

5.1   Neutron Fluence with The NE213 spectrometer

Neutron fluence is defined as the total number of neutrons incident on a cross-sectional area over a defined period of time [Bartlett, et al., 2003] [Thomas, et al., 2011], and can be determined from experimental measurements and is expressed mathematically as:

$$\Phi = \frac{N_i}{A} \tag{5.1}$$

where Φ is the neutron fluence, N_i is the total number of neutrons incident on the detector and A is the cross sectional area of the detector. For determination of neutron fluence spectra, neutron detection efficiency is required as a function of neutron energy.

5.1.1 Neutron detection efficiency for the NE213 spectrometer

Consider a beam of mono-energetic neutrons incident on a slap detector with thickness t (fig 5.1). The neutron detection efficiency $\varepsilon(E_n)$ is given by:

$$\varepsilon(E_n) = \frac{N}{N_i} \tag{5.2}$$

Where N is the number of neutrons detected by the spectrometer. The efficiency of the detector depends on [Herbert, 2009]:

- Incident neutron energy
- Reaction cross-sections
- Detector thickness
- Direction of incident neutrons
- Electronic threshold and other applicable electronic selections
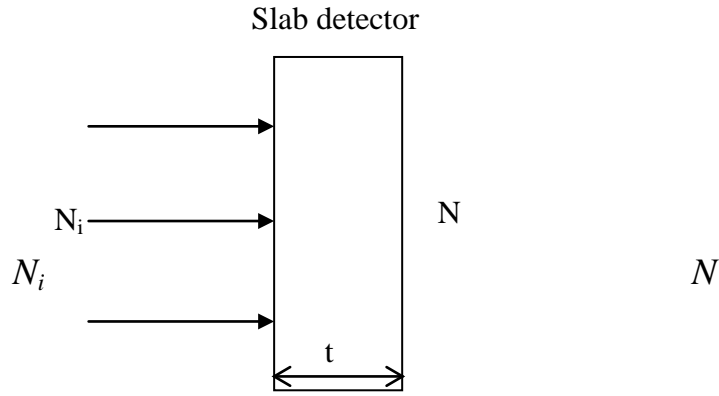
Slab detector

Figure 5. 1: Mono energetic beam of neutrons incident on a slab detector of thickness t

$$t$$

For the NE213 spectrometer, the detection efficiency can be calculated for recoiling protons from n-p elastic scattering only using well known reaction cross-sections and is given by:

$$\varepsilon_H(E_n) = \phi_{npf} \frac{n_H \sigma_H}{n_H \sigma_H + n_C \sigma_C} \left[1 - e^{-(n_H \sigma_H + n_C \sigma_C)} \right] \tag{5.3}$$

where:

n_H : The number of hydrogen nuclei per unit cross-sectional area presented by the scintillator to the neutron beam

n_C : The number of carbon nuclei per unit cross-sectional area presented by the scintillator to the beam.

σ_H : Total cross-sections for n-p elastic scattering

σ_c : Total cross-sections for neutron induced reactions with ^{12}C in the scintillator.

ϕ_{npf} : Fraction of elastically scattered protons detected above pulse height threshold L_c

Table 5. 1: *Cross-sections for n-p elastic scattering σ_H and n-^{12}C interactions σ_C together with their products $n_H\sigma_H$ and $n_C\sigma_C$ calculated for 5 cm × 5 cm NE213 scintillator.*

E_n (MeV)	σ_H (barn)	$n_H\sigma_H$	σ_C (barn)	$n_C\sigma_C$
10	0.938	0.237	1.173	0.233
20	0.482	0.122	1.507	0.300
30	0.306	0.077	1.295	0.258
40	0.218	0.055	1.111	0.221
50	0.163	0.041	0.946	0.188
60	0.134	0.034	0.812	0.162

Using the values in table 5.1, the term $(n_H\sigma_H + n_C\sigma_C) \ll 1$ at higher energies, this reduces Eq. 5.3 to:

$$\varepsilon(E_n) = \phi_{npf} \frac{n_H\sigma_H}{n_H\sigma_H + n_C\sigma_C} \left[1 - \left(1 - n_H\sigma_H - n_C\sigma_C\right)\right] \tag{5.4}$$

Thus Eq. 5.4 becomes:

$$\varepsilon(E_n) = \phi_{npf}\, n_H\sigma_H \tag{5.5}$$

Each input quantity used to determine the detection efficiency of NE213 will be discussed with reference to 64 MeV neutrons as an illustration.

(a) Total cross-sections for n-p elastic scattering

Figure 5.2 shows total cross-sections for n-p elastic scattering used in this work, the cross-section data were obtained from ENDF data library [Rose, 1991]. At 64 MeV the value of total cross section for n-p elastic scattering is 0.124 barn.
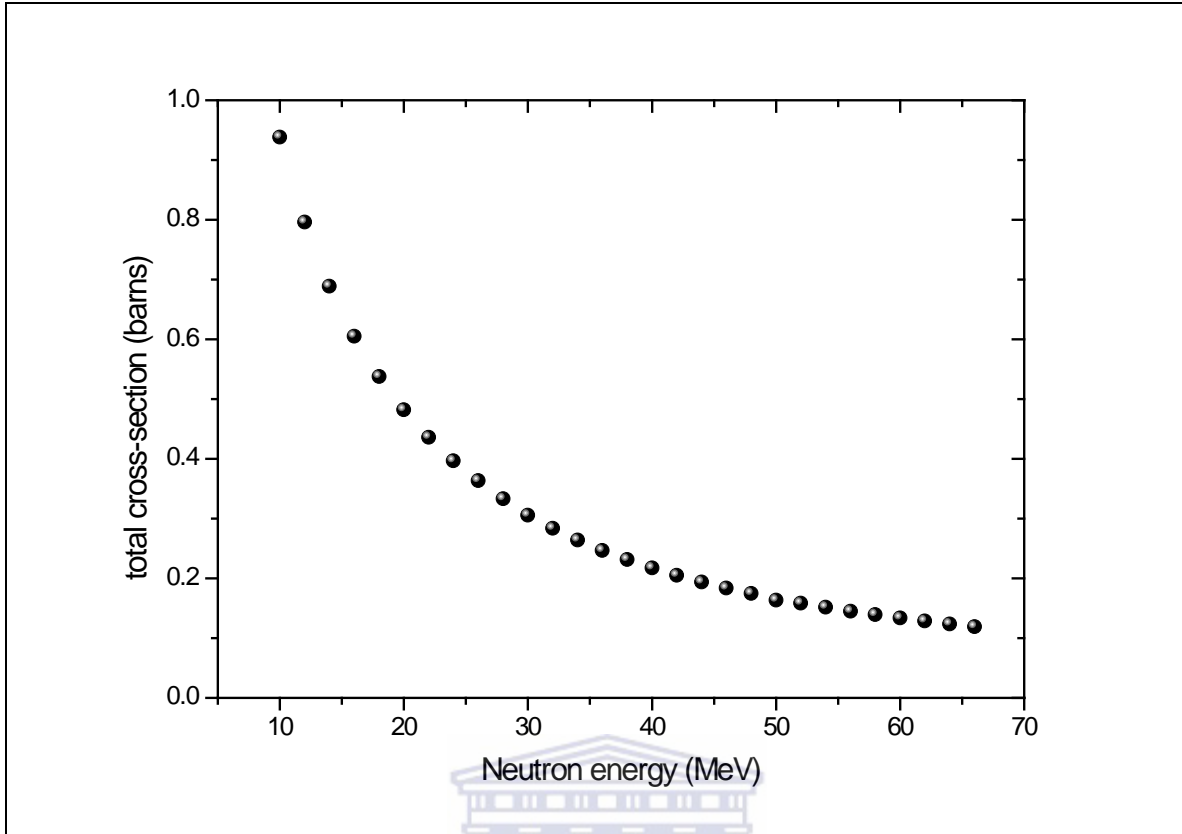
Figure 5. 2: *Total cross-sections for n-p elastic scattering [Rose, 1991].*

(b) n_H: the number of hydrogen nuclei per unit cross-sectional area presented by the scintillator to the neutron beam

The number of hydrogen nuclei per cross-sectional area is given by:

$$n_H = \frac{N_A \rho l \eta_H}{M} \qquad (5.6)$$

where:

N_A : Avogadro's number (6.022×10^{23} mol^{-1})

ρ : Density of NE213 organic liquid scintillator (0.874 g.cm^{-3})

l : The length of the NE213 organic liquid scintillator (5 cm)

η_H : The number of hydrogen atoms per molecule of NE213 scintillator (10.2)

M : Molar mass of the NE213 scintillator (106 g.mol^{-1})

69

From the Eq. 5.6, n_H was calculated to be 2.53×10^{23} cm^{-2} corresponding to 0.253 barn^{-1}.

(c) ϕ_{npf}: The fraction of n-p elastic scattering events detected above pulse height threshold L_c.

Figure 5.3 shows the pulse height spectrum measured with the NE213 spectrometer for 64 MeV neutrons, features of the spectrum were discussed in sections 4.3 and 4.4, the number of neutron events above pulse height threshold L_c detected via recoiling protons are labelled N_{np}.
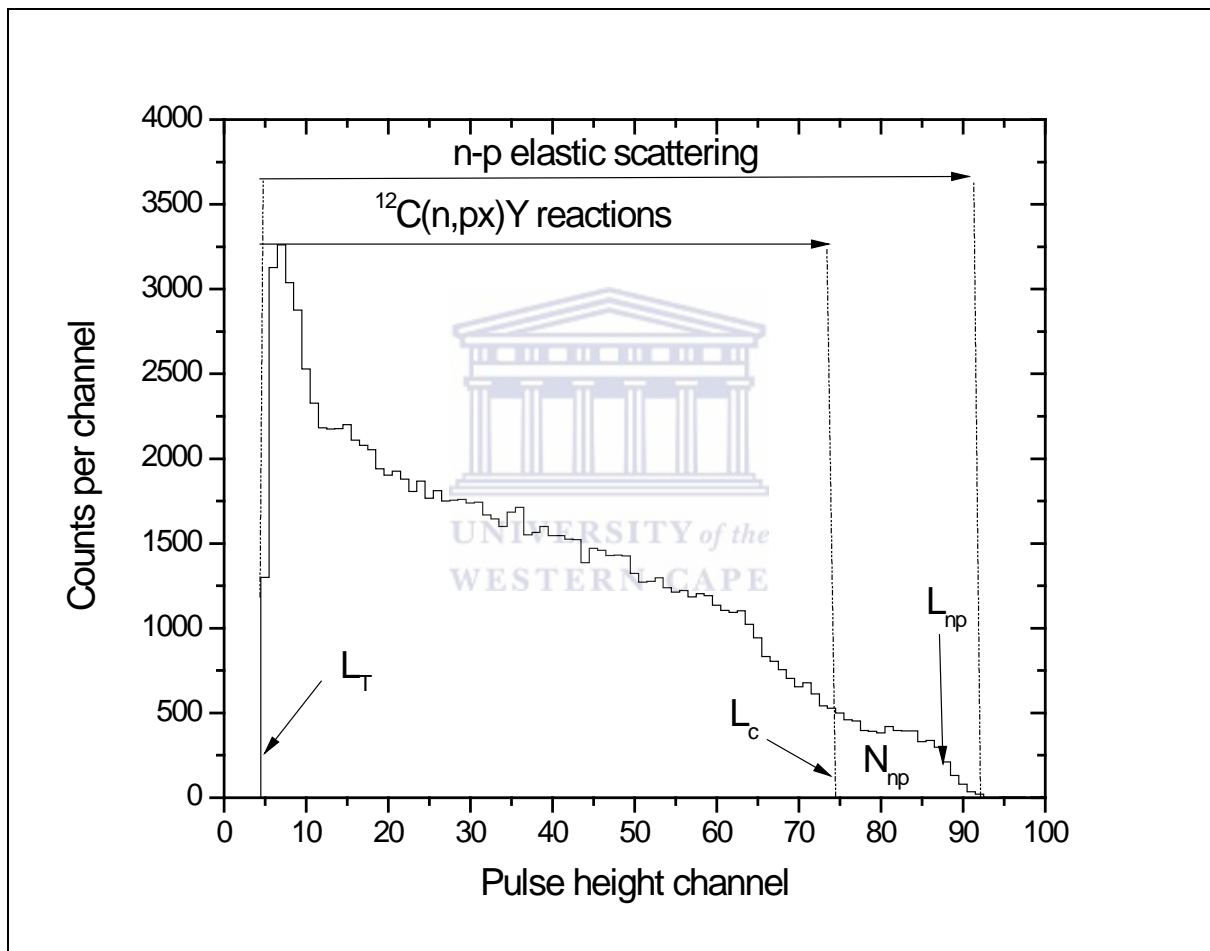
Figure 5. 3: *Pulse height spectrum measured with the NE213 spectrometer for 64 MeV incident neutrons.*

Recoiling protons with pulse height above L_c from n-p elastic scattering events lie within a cone with internal angle ζ in the laboratory frame. The angle ζ is related to incident neutron energy E_n and recoiling proton energy E_p by:

$$\cos(\zeta) = \frac{E_p}{m_p c^2 (\gamma_3^2 - 1)} - 1. \tag{5.7}$$

with

$$\gamma_3 = \frac{\gamma_1}{\gamma_2} . \tag{5.8}$$

where

$$\gamma_1 = \frac{m_p}{m_n} + \frac{E_n}{m_n c^2} + 1. \tag{5.9}$$

and

$$\gamma_2 = \sqrt{\left(\frac{m_p}{m_n}\right)^2 + 2\left(\frac{m_p}{m_n}\right)\left(\frac{E_n}{m_n c^2} + 1\right) + 1} . \tag{5.10}$$

where m_p and m_n are the rest masses of a proton and a neutron respectively, c is the speed of light. The angle ζ in the laboratory frame is related to the angle of the scattering neutron θ in the centre of mass frame and is given by:

$$\zeta = 180^0 - \theta . \tag{5.11}$$

Combining Eq. 5.7 and 5.11 we obtain:

$$\cos\theta = 1 - \frac{E_p}{m_p c^2 \left(\gamma_3^2 - 1\right)} . \tag{5.12}$$

The energy range of recoiling protons is $E_p = E_0$ (5 MeV) to E_n, this energy range corresponds to $\theta = \theta_0$ to π. The energy range of recoiling protons from n-p elastic scattering is $E_p = E_c$ to E_n, corresponding to $\theta_0 = \theta_c$ to π. The fraction of recoiling protons ϕ_{npf} above pulse height L_c is given by:

$$\phi_{npf} = \frac{\int_{\theta_c}^{\pi} \sigma(E_n, \theta) d\theta}{\int_{\theta_0}^{\pi} \sigma(E_n, \theta) d\theta}. \quad (5.13)$$

with

$$\cos\theta_c = 1 - \frac{E_c}{m_p c^2 (\gamma_3^2 - 1)}. \quad (5.14)$$

and

$$\cos\theta_0 = 1 - \frac{E_0}{m_p c^2 (\gamma_3^2 - 1)}. \quad (5.15)$$

where $\sigma(E_n, \theta)$ is the differential cross-section for n-p elastic scattering. Recommended differential cross-section evaluations for n-p elastic scattering as a function of neutron scattering angle ($\cos\theta$) obtained from ENDF data sets [Rose, 1991] and used in this work are shown in figure 5.4. For n-p elastic scattering data at 64 MeV corresponding to $E_c = 51.14$ MeV, $\cos\theta_c$ was calculated to be -0.607 and $\theta_c = 127.3^0$ with ϕ_{npf} calculated to be 0.272.
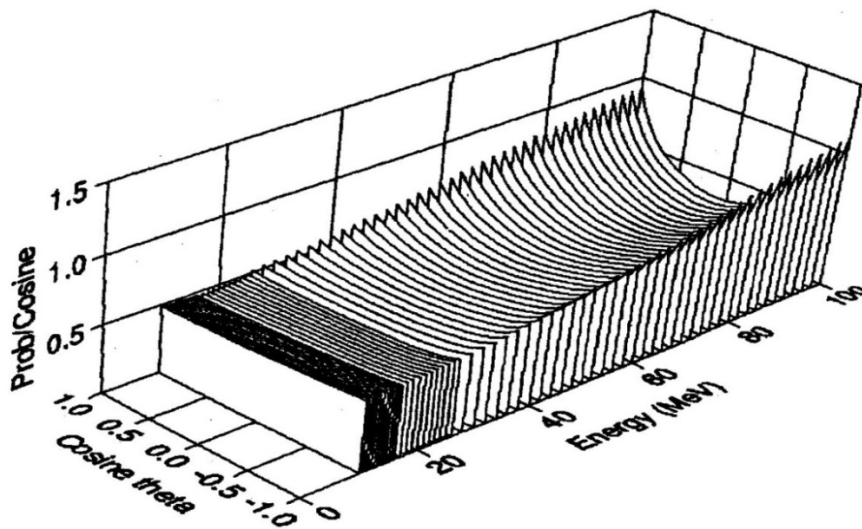
Figure 5. 4: *Differential cross-sections for n-p elastic scattering obtained from the ENDF data base as a function of neutron angle (cosine theta) in the centre of mass frame [Rose, 1991].*

The neutron detection efficiency of the NE213 spectrometer as a function of energy obtained in this work is shown in figure 5.5 together with the associated uncertainties. The uncertainties in the detection efficiency are discussed in section 5.1.3. The detection efficiency curve shows expected trend, however the curve does not decrease smoothly with increasing energy, with the smoothness of the curve disrupted below 20 MeV neutron energies. The disruption of the smoothness of the curve may be attributed to the fraction of recoiling protons above pulse height L_c, (ϕ_{npf}), below 20 MeV. Below 18 MeV the fraction $\phi_{npf} = 1$ and $\phi_{npf} \approx 1$ at 18 MeV (see table 5.2), thus all events in this energy range are attributed to recoiling protons from n-p elastic scattering.
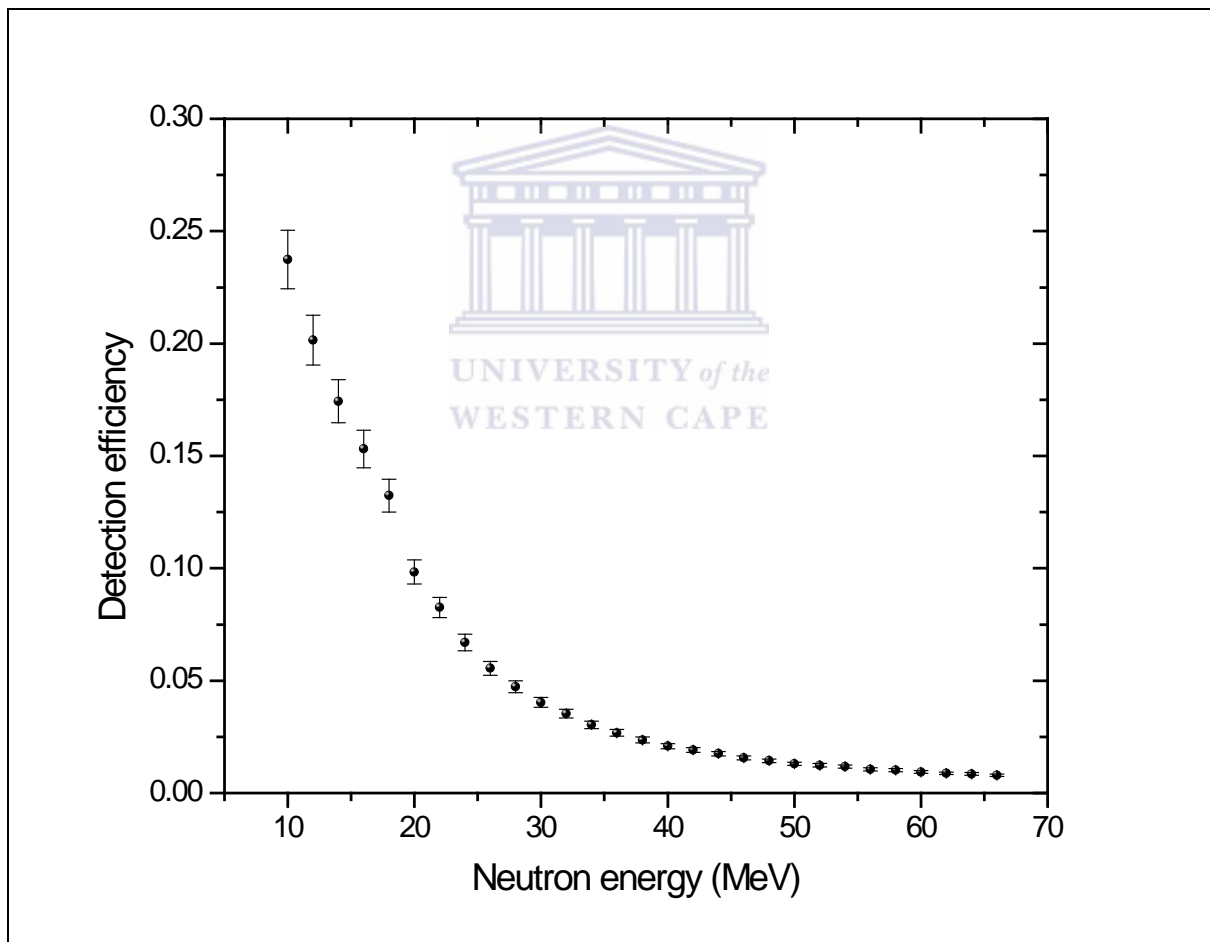
Figure 5. 5: *Neutron detection efficiency of the NE213 spectrometer as a function of neutron energy.*

5.1.2   Neutron fluence

The total number of neutrons incident on the NE213 spectrometer is given by:

$$N_i = \frac{N_{np}}{\varepsilon_H(E_n)}. \tag{5.16}$$

Where N_{np} is the number of neutrons detected via recoiling protons above pulse height threshold L_c by the NE213 spectrometer and $\varepsilon_H(E_n)$ is the detection efficiency of the NE213 spectrometer for n-p elastic scattering. The number of incident neutrons on the NE213 spectrometer is given by:

$$N_i = \frac{N_{np}}{\phi_{npf} n_H \sigma_H}. \tag{5.17}$$

A fraction of recoiling protons tend to escape the detector before depositing all their energies to the scintillator, thus resulting in their pulse height to fall below L_c. There arises a need to correct for these protons which would have had pulse height above L_c and this factor is given by:

$$\phi_{ep} = \left(1 - \textit{fraction of protons above } L_c \textit{ which escape}\right) \tag{5.18}$$

thus

$$N_i = \frac{N_{np}}{\phi_{npf}\,\phi_{ep}\,n_H \sigma_H}. \tag{5.19}$$

For a cross-sectional area A of the detector, the neutron fluence is given by:

$$\Phi = \frac{N_{np}}{A\phi_{npf}\,\phi_{ep}\,n_H \sigma_H}. \tag{5.20}$$
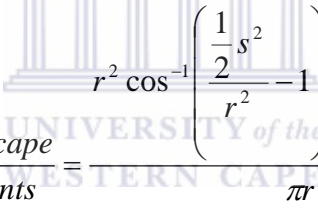
Input quantities used to calculate neutron detection efficiency of the NE213 spectrometer and neutron fluence measured with NE213 at particular energies of interest are shown in table 5.2.

(a) N_{np}: The integral counts measured above L_c

Event counts N_{np} detected above pulse height L_c were selected as events from n-p elastic scattering (refer to fig 5.3). The pulse height L_c at incident neutron energy 64 MeV was found to be 74 ADC channel corresponding to 51.14MeV. The integral count of events N_{np} for this neutron energy was calculated to be 3103 counts for the Li-target.

(b) ϕ_{ep}: Correction factor for recoiling protons above pulse height threshold L_c escaping the NE213 scintillator.

The range of protons, deuterons, and alpha particles as a function of recoiling charged particle energy in the NE213 scintillator is shown in figure 5.6. The ranges were calculated using the computer program ELOSS. At 40 MeV, the range for protons, deuterons and alpha particles is 1.678, 0.957, and 0.138 respectively. It can be seen that protons have a longer range as compared to deuterons and alphas particles in the same scintillator (NE213 scintillator) for the same energy. The fraction of protons above pulse height L_c is given by (see appendix B):

$$\phi_{ep} = \frac{protons\ non\ escape}{all\ proton\ events} = \frac{r^2 \cos^{-1}\left(\dfrac{\dfrac{1}{2}s^2}{r^2} - 1\right) - \dfrac{1}{2}s\sqrt{4r^2 - s^2}}{\pi r^2}. \tag{5.21}$$

Where r is the radius of the detector, and s is the range of a recoiling proton at a particular particle energy in NE213 scintillator. For a detector radius of 2.5 cm, with the recoiling proton range of 3.922 at 64 MeV, the fraction of recoiling proton above pulse height L_c was calculated to be 0.116 at this energy.
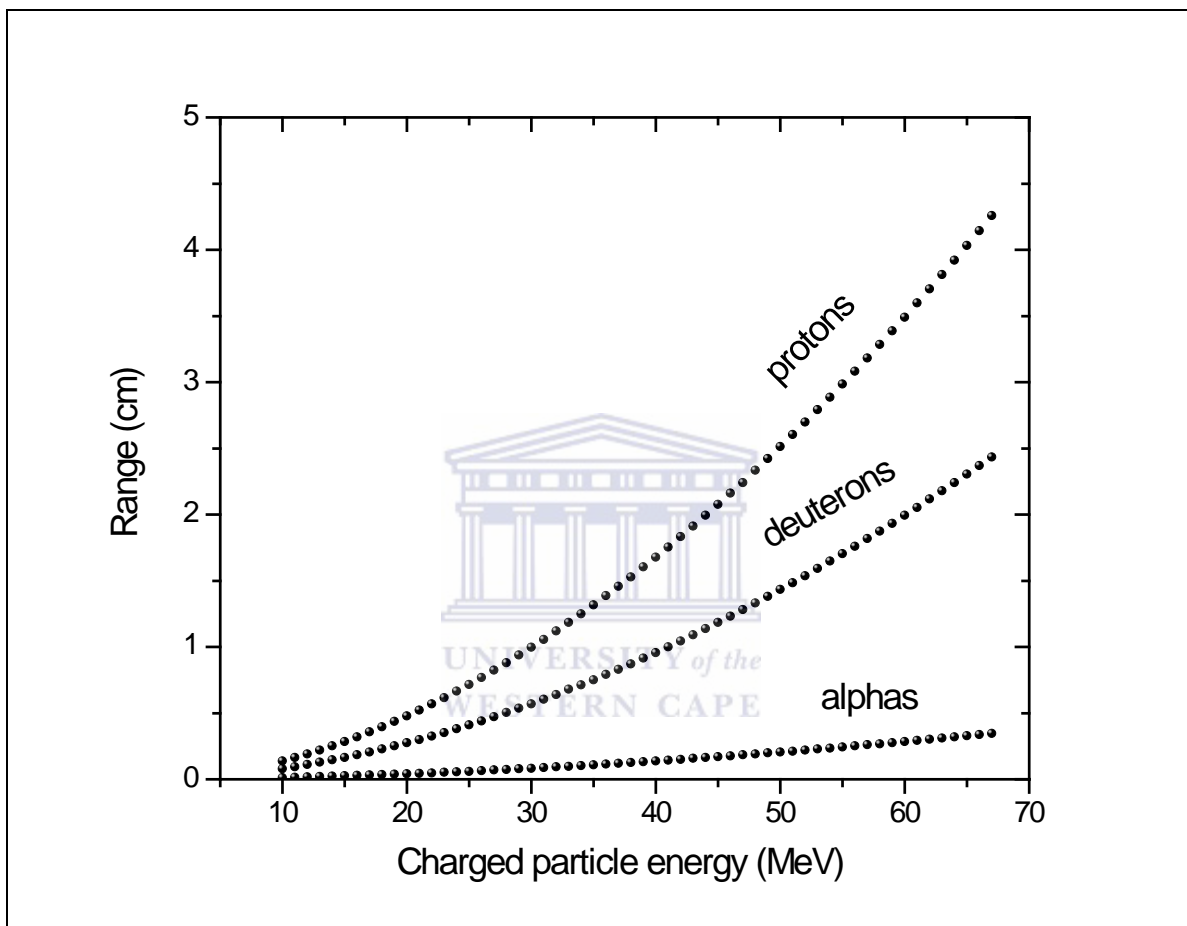
Figure 5. 6: *Range of protons, deuterons, and alpha particles in the NE213 scintillator of radius 2.5 cm*

Table 5. 2: *Input quantities used to calculate neutron fluence measured with the NE213 spectrometer for each target.*

E_n (MeV)	L_c (channel)	n_H (barn^{-1})	σ_H (barn)	ϕ_{npf}	ϕ_{ep}	$N_{np}(Li)$ (counts)	$N_{np}(Be)$ (counts)	$N_{np}(C)$ (counts)
10	5	0.253	0.938	1.000	0.965	15405	104624	257036
12	5	0.253	0.796	1.000	0.951	14503	93355	240294
14	5	0.253	0.689	1.000	0.936	14276	90796	242485
16	5	0.253	0.605	1.000	0.919	13386	80215	220678
18	6	0.253	0.538	0.973	0.899	12601	73962	206799
20	9	0.253	0.482	0.806	0.878	10406	60077	167255
22	10	0.253	0.436	0.749	0.856	10194	57430	160403
24	13	0.253	0.397	0.668	0.831	9089	50290	138215
26	16	0.253	0.363	0.603	0.805	8224	44107	121976
28	20	0.253	0.333	0.562	0.777	6948	35742	96722
30	23	0.253	0.306	0.521	0.748	6054	29469	82396
32	26	0.253	0.284	0.493	0.717	5293	25610	70544
34	30	0.253	0.264	0.455	0.685	4465	21029	55915
36	33	0.253	0.247	0.429	0.652	3737	17534	44579
38	36	0.253	0.231	0.403	0.617	3474	15411	36324
40	40	0.253	0.218	0.379	0.581	2503	11499	23063
42	42	0.253	0.205	0.370	0.544	2493	11586	16869
44	46	0.253	0.194	0.357	0.506	2078	10106	8865
46	48	0.253	0.184	0.337	0.467	1911	12937	7246
48	52	0.253	0.175	0.325	0.428	1516	14191	3632
50	54	0.253	0.163	0.317	0.388	1348	17121	454
52	57	0.253	0.159	0.308	0.348	1024	14585	
54	59	0.253	0.152	0.307	0.308	928	12977	
56	62	0.253	0.145	0.288	0.268	645	11799	
58	65	0.253	0.139	0.290	0.229	373	9578	
60	68	0.253	0.134	0.278	0.190	314	8391	
62	71	0.253	0.128	0.270	0.152	397	5701	
64	74	0.253	0.124	0.272	0.116	3103	3114	
66	85	0.253	0.119	0.264	0.083	1938		

77

5.1.3 Estimates of uncertainties in NE213 measurements

The uncertainty in the calibration constant k was found to be about 5% of the calculated value. Uncertainty in the estimated incident neutron energy was calculated using Eq. 4.7 for neutrons less than 64 MeV. For the 64 MeV peak (refer to figure 4.5 (a)) the uncertainty was found to be 1.78 MeV for all neutrons falling within this peak. Systematic uncertainties associated with the measurements are due to charged particle loci in the *LS*-plot used to select charged particles of interest, neutron ToF windows, and the measurements of all peaks and edges in the pulse height spectra. These uncertainties proved difficult to assess, however a fluctuation of less than 2% in repeated measurements was calculated [Buffler, 1991]. Uncertainties due to counting statistics in the counts of pulse height spectra were calculated to be less than 2%, this is due to that the total number of counts in each pulse height spectra is typically in the order of 10^4.

The uncertainty in the neutron detection efficiency of the NE213 spectrometer and neutron fluence measured with the NE213 spectrometer are attributed to the uncertainties in each input quantity used in Eq. 5.4 and 5.19 respectively. The uncertainties in these input quantities are categorised into type A and type B [GUM, 2008] [Barry & Kuyatt, 1994]. Uncertainties categorised as type A are based on valid statistics, for measurements in this work, a Gaussian distribution was used to model the knowledge about these quantities, thus a square root of the measured quantity is the uncertainty of the estimated value. Type B categorized uncertainties were calculated based on scientific judgement using all available knowledge about the measurements [Barry & Kuyatt, 1994]. In this case a Probability Density Function (PDF) was used to model the uncertainty in each quantity. The uncertainty in these quantities is given by:

$$\Delta x_i = \frac{\frac{1}{2}\left(x_{upper} - x_{lower}\right)}{\sqrt{3}}. \tag{5.22}$$

where x_{lower} and x_{upper} are lower and upper limits in the PDF, respectively. For quantities calculated using a combination of input quantities such as calibration constant k, incident neutron energy, detection efficiency and neutron fluence, a quadratic summation was used and is given by [Bevington & Robinson, 2003]:

$$\left(\frac{\Delta x}{x}\right) = \sum_i \left(\frac{\Delta x_i}{x_i}\right)^2. \tag{5.23}$$

Table 5.3 shows uncertainties of each input quantity used to calculate the neutron detection efficiency of the NE213 spectrometer and neutron fluence measured with The NE213 spectrometer at 64 MeV. The uncertainties in the detection efficiency and neutron fluence are shown in table 5.4.

Table 5. 3: *Input quantities with the uncertainties used to calculate the neutron detection efficiency of the NE213 spectrometer and neutron fluence for the Li-target for 64 MeV neutrons.*

Input quantity	x_i	Δx_i	Uncertainty type	x_{lower}	x_{upper}
N_{np}	3103	56	A	-	-
σ_H	0.124	0.004	B	0.118	0.130
n_H	0.253	0.005	B	0.247	0.266
ϕ_{npf}	0.272	0.014	B	0.256	0.305
ϕ_{ep}	0.116	0.005	B	0.110	0.127
A	19.634	0.425	B	19.144	20.617

UNIVERSITY *of the*

WESTERN CAPE

Table 5. 4: *The neutron detection efficiency for the NE213 spectrometer and neutron fluence together with their uncertainties for each target.*

E_n (MeV)	ε_H	$\Delta\varepsilon_H$	$\Phi(Li)$ (n.cm^{-2})	$\Delta\Phi(Li)$ (n.cm^{-2})	$\Phi(Be)$ (n.cm^{-2})	$\Delta\Phi(Be)$ (n.cm^{-2})	$\Phi(C)$ (n.cm^{-2})	$\Delta\Phi(C)$ (n.cm^{-2})
10	0.2374	0.0130	3425	248	23260	1676	57144	4114
12	0.2015	0.0111	3854	279	24806	1787	63850	4597
14	0.1743	0.0096	4455	323	28337	2042	75678	5449
16	0.1531	0.0084	4848	351	29051	2093	79923	5755
18	0.1324	0.0073	5391	391	31642	2280	88473	6370
20	0.0984	0.0054	6134	446	35413	2553	98591	7100
22	0.0826	0.0045	7348	534	41394	2984	115614	8326
24	0.0671	0.0037	8305	604	45952	3313	126292	9096
26	0.0555	0.0030	9379	683	50300	3628	139101	10019
28	0.0473	0.0026	9623	702	49504	3572	133963	9651
30	0.0403	0.0022	10229	748	49791	3595	139216	10031
32	0.0354	0.0019	10625	778	51407	3714	141603	10205
34	0.0304	0.0017	10927	803	51464	3721	136841	9865
36	0.0268	0.0015	10913	805	51204	3705	130183	9390
38	0.0236	0.0013	12149	898	53894	3903	127028	9166
40	0.0208	0.0011	10528	786	48366	3510	97005	7011
42	0.0192	0.0011	12156	908	56492	4099	82252	5953
44	0.0175	0.0010	11937	898	58052	4218	50924	3705
46	0.0157	0.0009	13268	1002	89818	6512	50307	3669
48	0.0144	0.0008	12563	960	117601	8521	30098	2223
50	0.0131	0.0007	13527	1041	171811	12435	4556	391
52	0.0124	0.0008	12116	1024	172566	13622		
54	0.0118	0.0007	13033	1109	182256	14397		
56	0.0106	0.0007	11612	1020	212423	16791		
58	0.0102	0.0006	8135	765	208902	16538		
60	0.0094	0.0006	8962	866	239490	18982		
62	0.0088	0.0006	15164	1413	217764	17337		
64	0.0085	0.0005	159453	12841	160019	12885		
66	0.0080	0.0005	149965	12256				

5.2 Neutron fluence with the NE230 spectrometer

5.2.1 Detection efficiency of the NE230 spectrometer

To measure neutron fluence with the NE230 spectrometer, there is a need to determine the detector efficiency. In this work detector efficiency of The NE230 spectrometer has been determined using two methods:

(i) Efficiency of the NE230 spectrometer for n-d elastic scattering.

(ii) Efficiency of the NE230 spectrometer relative to n-p elastic scattering (NE213 detector efficiency).

The motivation for using two methods in determining the efficiency of the NE230 spectrometer is that method (i) offers a way to determine the neutron fluence measured with the NE230 spectrometer independently of detection efficiency of the NE213 spectrometer. The challenge with (i) however is the unavailability of n-d reaction cross-sections for elastic scattering for some energies in the energy range of interest. If the reaction cross-sections are known or can be estimated for all energy range of interest, the detection efficiency of the NE230 spectrometer may be calculated analogous to that of the NE213 spectrometer [Knoll, 2000]. Method (ii) has been recommended for determining the efficiency of the NE230 spectrometer [Herbert, 2009]. This is since it relies on the efficiency of The NE213 spectrometer of which the cross-sections are well known. As mentioned previously (refer to sections 4.3 and 4.4), it is difficult to separate accurately the deuterons resulting from n-d elastic scattering to those resulting from n-^{12}C reactions in the pulse height spectra measured with NE230 at high neutron energies. To overcome this challenge all events in the pulse height spectra measured with The NE230 spectrometer were selected for method (ii).

(i) The efficiency of the NE230 spectrometer for n-d elastic scattering

The neutron detection efficiency of the NE230 spectrometer using reaction cross-sections for n-d elastic scattering for neutron energy range of interest is given by:

$$\varepsilon_D(E_n) = \phi_{ndf} \frac{n_D \sigma_D}{n_D \sigma_D + n_C \sigma_C} \left[1 - e^{-(n_D \sigma_D + n_C \sigma_C)} \right].$$ (5.24)

Where:

n_D :   The number of deuteron nuclei per unit cross-sectional area presented by the scintillator to the beam.

n_C : The number of carbon nuclei per unit cross-sectional area presented by the scintillator to the beam.

σ_D : Total cross-section for n-d elastic scattering

σ_c : Total cross-sections for neutron induced reactions with ^{12}C.

ϕ_{ndf} : Fraction of elastically scattered deuterons detected above pulse height threshold L_{cd}.

The term $(n_D \sigma_D + n_C \sigma_C) \ll 1$ at higher energies, this reduces Eq. 5.24 to:

$$\varepsilon_D(E_n) = \phi_{ndf} n_D \sigma_D .\tag{5.25}$$

Each quantity used to calculate the detection efficiency for n-d elastic scattering is illustrated for 64 MeV neutrons.

(a) Total cross-section for n-d elastic scattering

Figure 5.7 shows total cross-sections for n-d elastic scattering as a function of neutron energy used in this work, the data was obtained from the ENDF data sets [ENDF]. From the data the value of total cross-section for n-d elastic scattering at 64 MeV is 0.075 barn
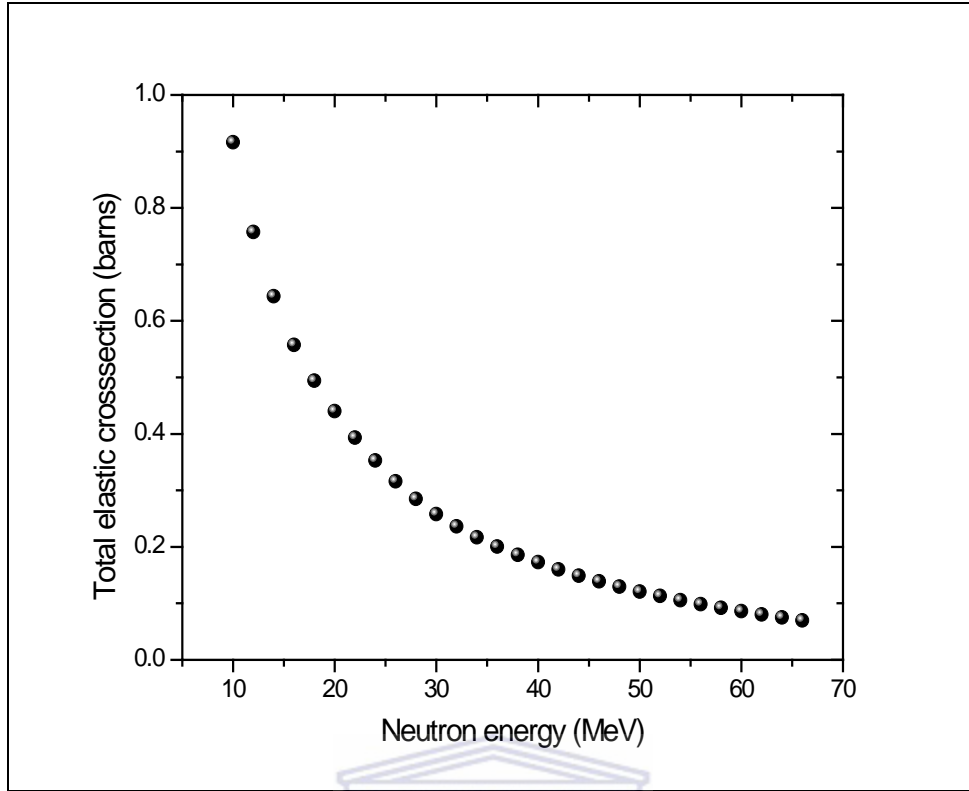
Figure 5. 7: *Total cross-section for n-d elastic scattering as a function of neutron energy obtained from ENDF data [ENDF].*

(b) n_D: The number of deuterium nuclei per cross-sectional area presented by the scintillator to the beam.

The number of deuterium nuclei per cross-sectional area of NE230 scintillator of thickness 2.5 cm is given by:

$$n_D = \frac{N_A \rho l \eta_D}{M}. \tag{5.26}$$

Where:

N_A : Avogadro's number (6.022×10^{23} mol^{-1})

ρ : Density of NE230 organic liquid scintillator (0.945 g.cm^{-3})

l : The length of the NE230 organic liquid scintillator (2.5 cm)

η_D : The number of deuterium atoms per molecule of NE230 scintillator (6)

M : Molar mass of the NE230 scintillator (84.15 g.mol^{-1})

n_D was calculated using Eq. 5.26 to be 1.101×10^{23} cm^{-2} corresponding to 0.101 barn^{-1}.

(c) Fraction of elastically scattered deuterons detected above pulse height threshold L_{cd}.

Figure 5.8 shows a pulse height spectrum measured with The NE230 spectrometer for 64 MeV incident neutrons. Features of the spectrum were discussed (sections 4.3 and 4.4), with the number of neutrons detected above pulse height L_{cd} labelled N_{nd}.
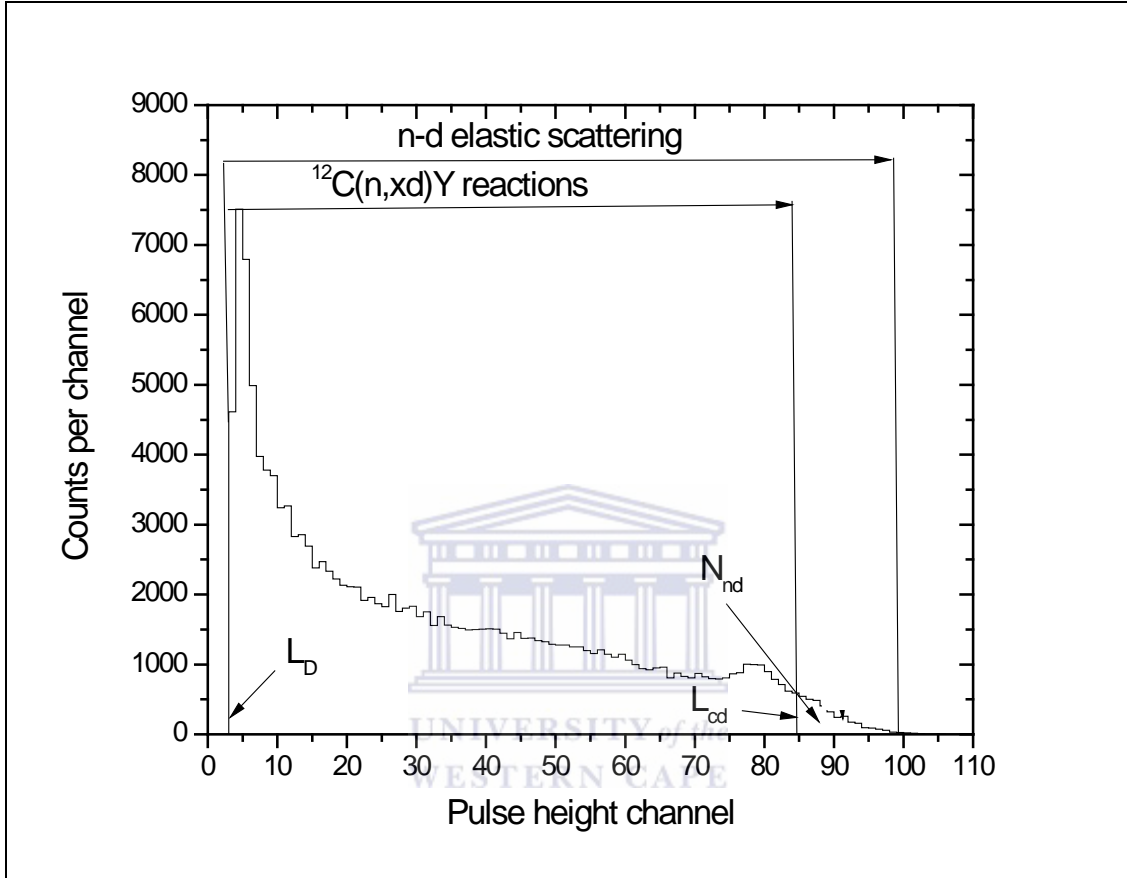
Figure 5. 8: Pulse height spectrum measured with NE230 for incident neutrons of 64 MeV.

Recoiling deuterons from n-d elastic scattering events producing pulse height greater than L_{cd} thus have energy $E_d > E_{cd}$ were calculated analogues to recoiling protons in the NE213 scintillator, using the rest mass of neutrons and deuterons m_n and m_d, and the energy E_d of recoiling deuterons due to n-d elastic scattering. The fraction of recoiling deuterons above pulse height threshold L_{cd} is given by:

$$\phi_{ndf} = \frac{\int_{\theta_{cd}}^{\pi} \sigma(E_n,\theta)d\theta}{\int_{\theta_0}^{\pi} \sigma(E_n,\theta)d\theta} \tag{5.27}$$

84

Where $\sigma_D(E_n, \theta)$ is the differential cross-section for n-d elastic scattering at different neutron energies. With the scattered neutron angles θ_{cd} and θ'_0 obtained from:

$$\cos\theta_{cd} = 1 - \frac{E_c}{m_p c^2 \left(\gamma_3^2 - 1\right)}.$$

(5.28)

and

$$\cos\theta'_0 = 1 - \frac{E_0}{m_d c^2 \left(\gamma_3^2 - 1\right)} .$$

(5.29)

For deuterons detected above $L > L_{cd}$ corresponding to $E_d > E_{cd}$ and electronic pulse height threshold L_D corresponding $E_0(5\ MeV)$.

As highlighted earlier, the challenge is the unavailability of differential cross-sections for n-d elastic scattering at some particular neutron energies of interests. The unavailable differential cross-sections were estimated by fitting Legendre polynomials of appropriate order to the available differential cross-sections [ENDF].
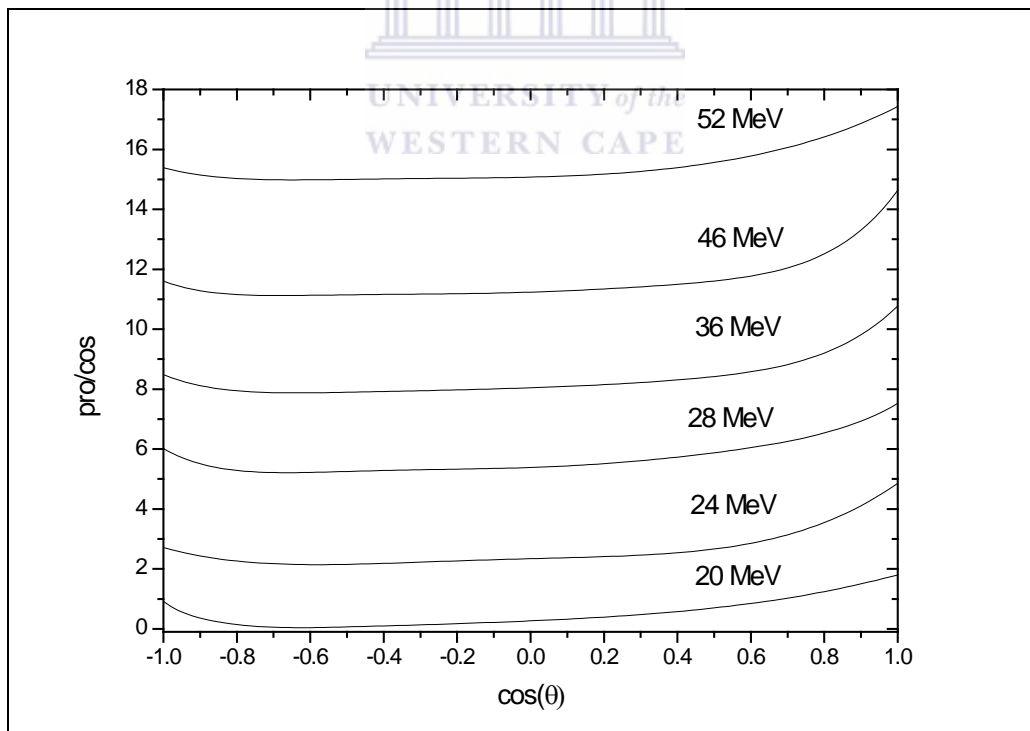
Figure 5. 9: *Legendre polynomial fits to some available differential cross-sections (not shown) for n-d elastic scattering as a function of scattered neutron angle θ (cosine theta) in the centre of mass frame obtained from ENDF data sets [ENDF].*
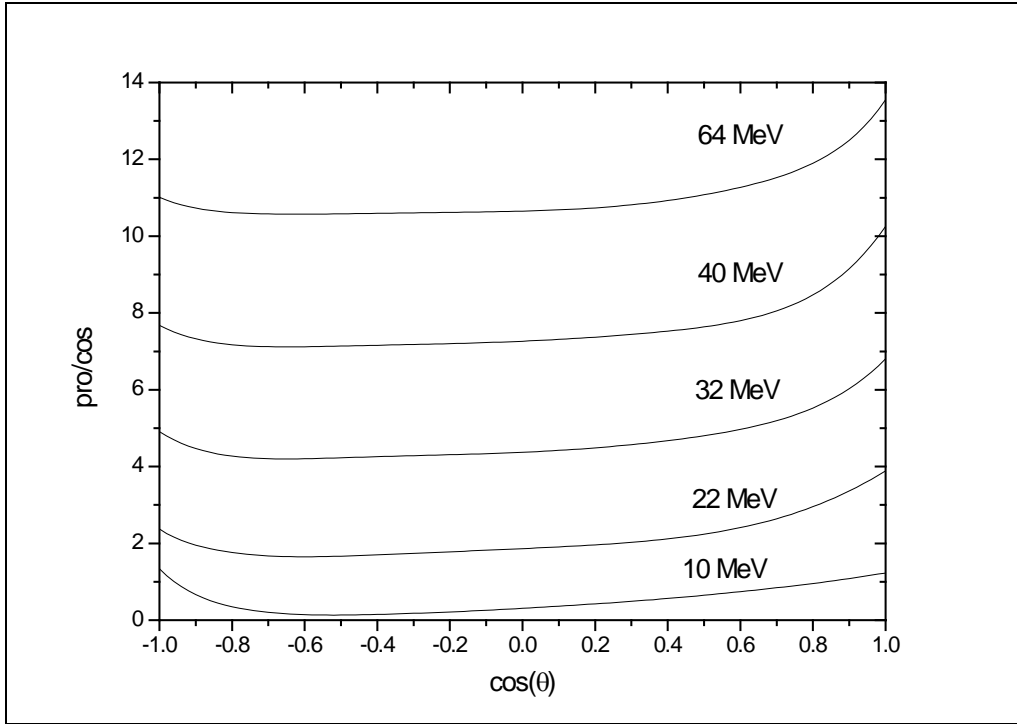
Figure 5. 10: *Legendre polynomial fits of differential cross-sections for n-d elastic scattering as a function of scattered neutron angle θ (cosine theta) in the centre of mass frame, obtained for some missing incident neutron energies within the range of interest.*

A method of midpoint between two successive functions of differential cross-sections to unknown differential cross-sections at unavailable neutron energies was used to deduce unknown differential cross-sections for n-d elastic scattering. This method introduced deviations to the available differential cross-sections of up to about 11%. Available differential cross-sections for n-d elastic scattering obtained from ENDF data sets are shown in figure 5.9. Estimated differential cross-sections at some unavailable neutron energies are shown in figure 5.10. At 64 MeV incident neutrons, $\cos\theta_{cd}$ was determined to be -0.76 corresponding to $\theta_{cd} = 139.4^0$ for $E_{cd} = 50.27$ MeV. Using obtained data of differential cross-sections for n-d elastic scattering, fraction of recoiling deuterons producing pulse height $L > L_{cd}$ was calculated to be 0.095 for 64 MeV neutrons.

The neutron detection efficiency for the NE230 spectrometer as a function of energy obtained in this work is shown in figure 5.11 together with the associated uncertainties. The uncertainties in the detection efficiency are discussed in section 5.2.3. The detection efficiency curve show expected trend. Similar to the efficiency of the NE213 spectrometer, the efficiency of the NE230 spectrometer decrease with an increase in energy. The change of

86

the smooth drop of the curve at 20 MeV may be attributed to the fraction of recoiling deuterons above pulse height L_{cd}, (ϕ_{ndf}), below 20 MeV. Below 20 MeV the fraction $\phi_{ndf} = 1$, thus all events in this energy range are attributed to recoiling deuterons from n-d elastic scattering.
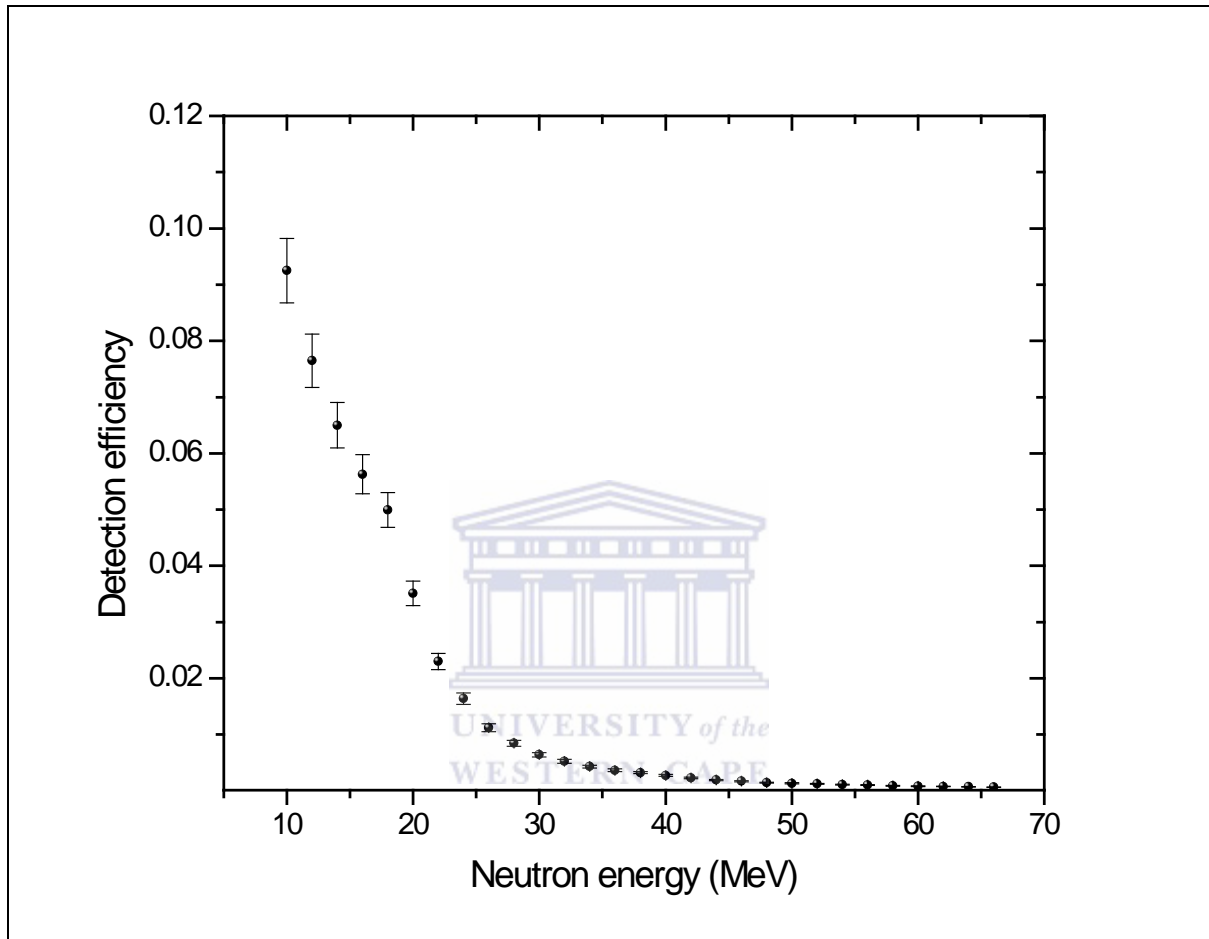
Figure 5. 11: Neutron detection efficiency of the NE230 spectrometer as a function of incident neutron energy calculated using available cross-sections for n-d elastic scattering.

(ii) Efficiency of the NE230 spectrometer relative to n-p elastic scattering (NE213 detection efficiency).

Consider the NE230 spectrometer exposed to the same beam of mono-energetic neutrons of energy E_n as in the case of the NE213 spectrometer (figure 5.1). We can express the detection efficiency of the NE230 spectrometer for detecting neutrons above pulse height L_D as:

$$\varepsilon_D'(E_n) = \frac{N_D}{N_0} . \qquad (5.30)$$

where, N_D is the number of deuteron events detected above pulse height threshold L_D as shown in figure 5.12 and N_0 is the number of mono-energetic neutrons incident on the NE230 spectrometer.
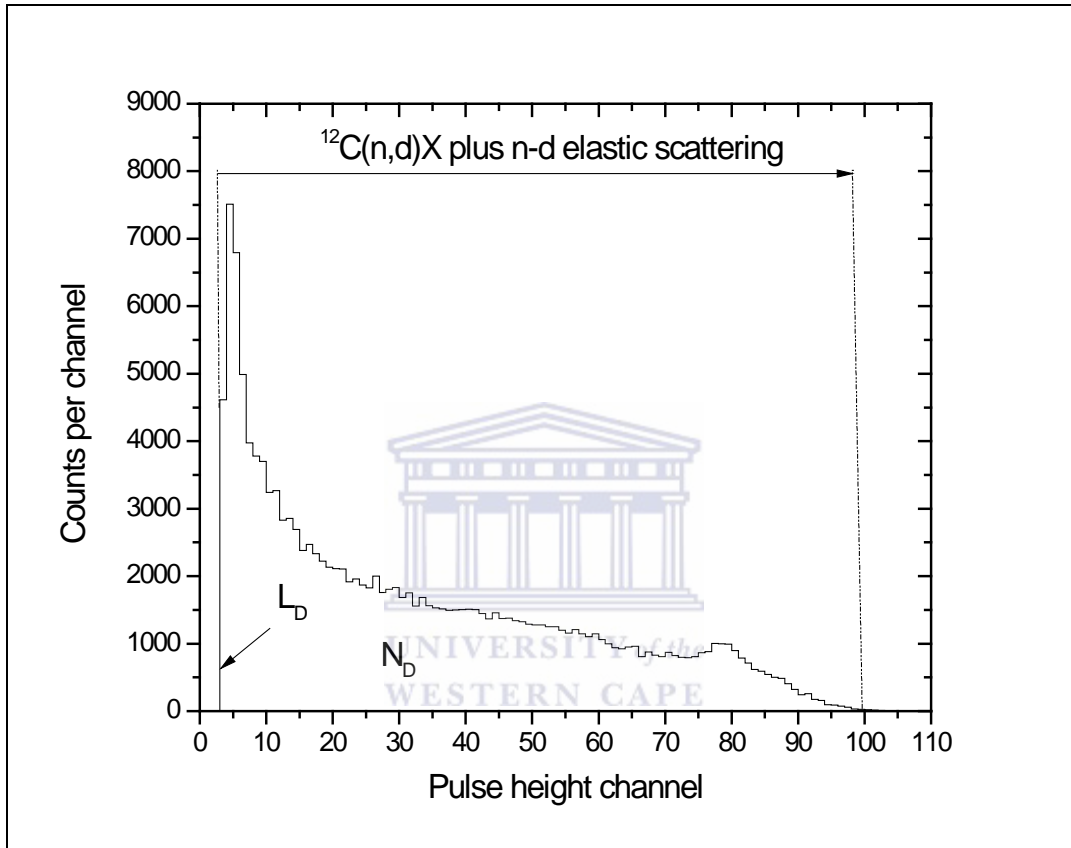
Figure 5. 12: *Pulse height spectrum measured with NE230 for incident neutrons of 64 MeV.*

Rearranging 5.30 we obtain:

$$N_D = \varepsilon_D'(E_n)N_0 . \qquad (5.31)$$

The detection efficiency of the NE230 spectrometer was determined from the ratio N_D/N_{np} and is given by:

$$\frac{N_D}{N_{np}} = \frac{\varepsilon_D'(E_n)N_0}{\varepsilon_H(E_n)N_{np}} . \qquad (5.32)$$

Using Eq. 5.5 and 5.32 the experimentally measured efficiency of NE230 relative to n-p elastic scattering is given by:

$$\varepsilon_D^{'} = \frac{N_D}{N_{np}} \frac{N_i}{N_0} \phi_{npf} \phi_{ep} n_H \sigma_H \, . \tag{5.33}$$

Normalising N_i and N_0 to the same number of neutrons counted using a neutron monitor, Eq. 5.33 becomes:

$$\varepsilon_D^{'} = \frac{N_D}{N_{np}} \frac{M_i}{M_0} \phi_{npf} \phi_{ep} n_H \sigma_H \, . \tag{5.34}$$

Where ϕ_{npf}, ϕ_{ep} , σ_H, n_H and N_{np} are as defined in section 5.1.1, M_i is the number of neutrons recorded by the neutron monitor (the NE213 spectrometer) during measurements of N_i using the NE213 spectrometer and M_0 using the NE230 spectrometer. The integral counts from the pulse height spectra of the sum targets for both the NE213 and the NE230 spectrometers were used to calculate the efficiency of the NE230 spectrometer.

(a) M_i and M_0 number of neutrons recorded by the neutron monitor.

The number of neutrons M_i recorded by the neutron monitor taken as the integral count over all target measurements during the NE213 spectrometer measurements was 35664. The reading M_0 recorded by the neutron monitor during measurements using the NE230 spectrometer was 89166.

(b) N_D: Integral of counts measured above pulse height threshold L_D measured with the NE230 spectrometer.

The integral number of counts above pulse height L_D was taken as the integral of all deuteron events in the pulse height spectrum (see figure 5.12). The number of counts (N_D and N_{np}) for the sum targets measured with each spectrometer were used for the determination of the efficiency relative to n-p elastic scattering. At 64 MeV incident neutrons, N_D was determined to be 147862 for the spectrum of the sum target.

The detection efficiency relative to cross-section for n-p elastic scattering is shown in figure 5.13. The trend in the efficiency of the NE230 spectrometer calculated relative to n-p elastic scattering below 20 MeV is mainly due to contribution of n-d elastic scattering events below 20 MeV, as the neutron energy increases (> 20 MeV) the contribution of

deuterons from n-^{12}C reactions tend to have a greater contribution, hence the trend at that energy range.
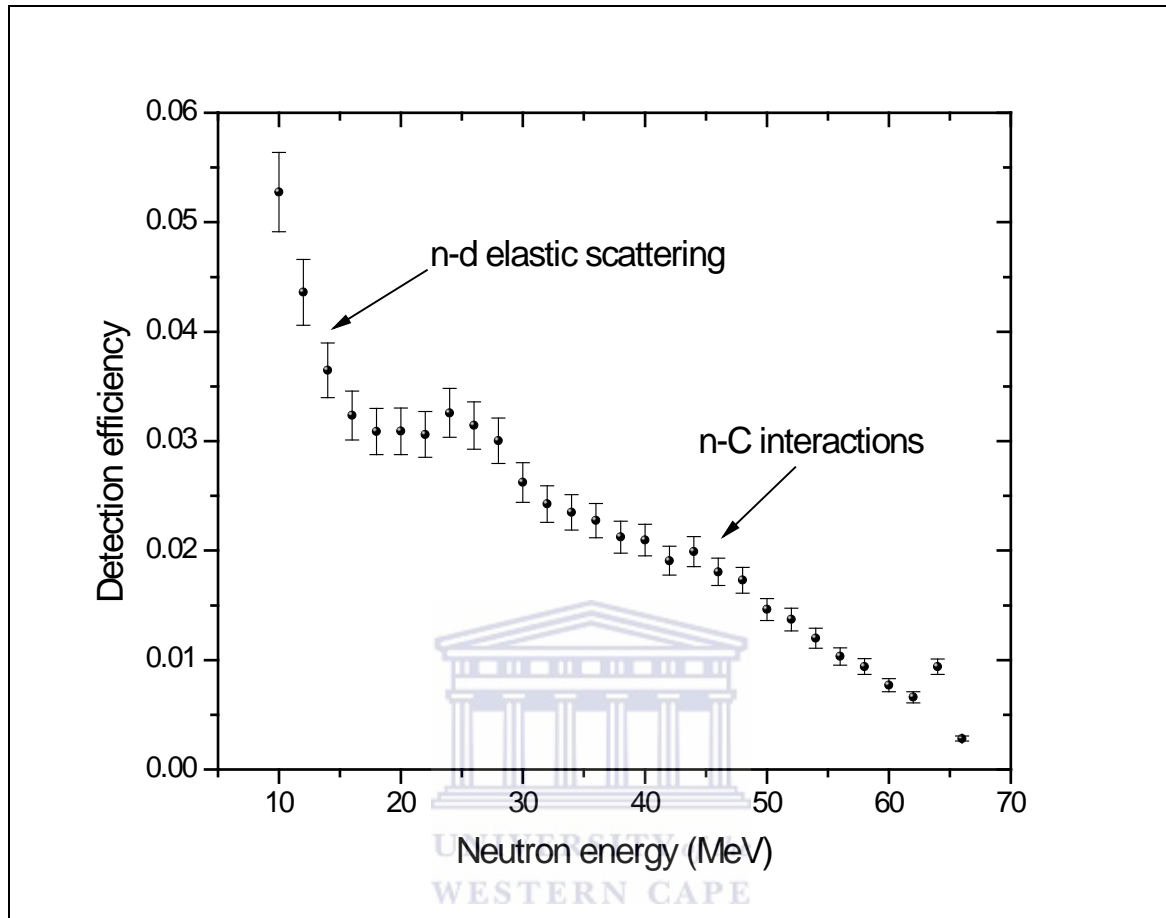
Figure 5. 13: Neutron detection efficiency of the NE230 spectrometer as a function of incident neutron energy determined relative to n-p elastic scattering.

5.2.2   Neutron fluence

Neutron fluence measured with the NE230 spectrometer is given by:

$$\Phi = \frac{N_0}{A} \tag{5.35}$$

where N_0 is the number of neutrons incident on the NE230 spectrometer, and A is the cross-sectional area of the NE230 scintillator. N_0 is related to the efficiency of the NE230 spectrometer. Since two methods ((i) and (ii)) were used to calculate the detector efficiency of the NE230 spectrometer, neutron fluence was calculated independently using efficiencies determined from both methods.

(i) Neutron fluence for n-d elastic scattering events

Neutron fluence determined by selecting only events due to n-d elastic scattering on the pulse height spectra, is obtained by using the relation:

$$N_0 = \frac{N_{np}}{\varepsilon_D} \tag{5.36}$$

Where N_{nd} is the integral number of counts above pulse height L_{cd}. Using Eq. 5.25 and Eq. 5.36, the neutron fluence measured with NE230 using n-d elastic scattering events is given by:

$$\Phi = \frac{N_{nd}}{An_D \sigma_D \phi_{ndf}} \tag{5.37}$$

A fraction of deuterons tend to leave the detector before depositing all their energy in the scintillator, resulting in their pulses to fall at lower pulse height (below L_{cd}). Therefore there arise a need to correct for the escape of deuterons, this is achieved by using a factor ϕ_{ed}, thus Eq. 4.43 becomes:

$$\Phi = \frac{N_{nd}}{An_D \sigma_D \phi_{ndf} \phi_{ed}} \tag{5.38}$$

Input quantities used to determine the detection efficiency and neutron fluence using the efficiency for n-d elastic scattering are shown in table 5.5.

(a) Integral number of counts above pulse height L_{cd}

At 64 MeV incident neutrons corresponding to 56 MeV deuteron energy, the pulse height L_{cd} was found to be 83 ADC channel corresponding to 50.27 MeV. The integral count of n-d elastic scattering events, N_{nd}, measured above pulse height L_{cd} was determined to be 4333 counts for the Li-target.

(b) ϕ_{ed}: Correction factor for recoiling deuterons above pulse height threshold L_{cd} escaping the NE230 scintillator

The range of deuterons in the NE230 scintillator at different energies was estimated using the Bragg-Kleeman rule which is a semi empirical formula [Knoll, 2000]:

$$\frac{s_1}{s_0} \cong \frac{\rho_0\sqrt{A_1}}{\rho_1\sqrt{A_0}} . \tag{5.39}$$

where:

s_1: The range of deuterons in the NE230 scintillator

s_0: The range of protons in the NE213 scintillator

ρ_1: The density of the NE230 scintillator (0.945 g.cm^{-3})

ρ_0: The density of the NE213 scintillator (0.874 g.cm^{-3})

A_1: The atomic weight of the NE230 scintillator (84.15 g.mol^{-1})

A_0: The atomic weight of the NE213 scintillator (106 g.mol^{-1})

Figure 5.14 shows the ranges of deuterons in the NE230 scintillator as a function of deuteron energy calculated using Eq. 5.39.
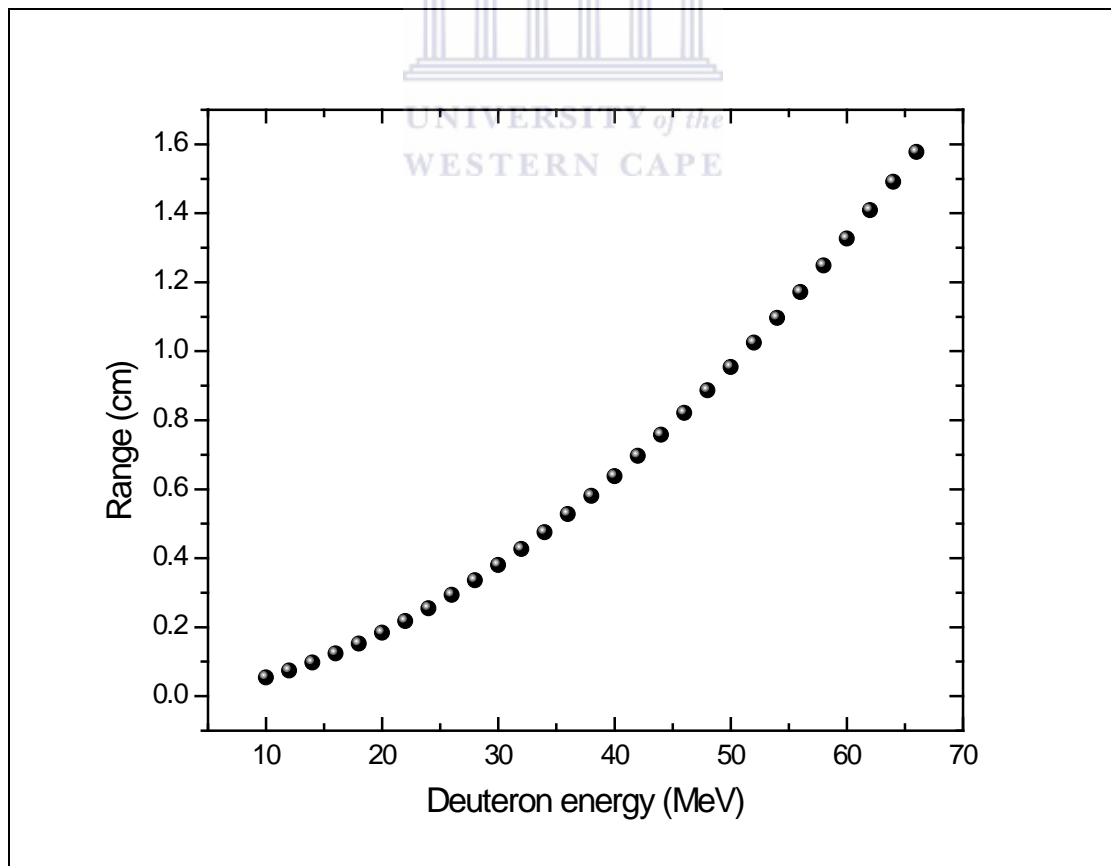
Figure 5. 14: *Range of deuterons in the NE230 scintillator as a function of deuteron energy used in this work.*

The range of protons in the NE213 scintillator with proton energy equal to deuteron energy in the NE230 scintillator was calculated using a computer program ELOSS. The correction factor for recoiling deuterons detected above pulse height L_{cd} escaping the NE230 scintillator is given by (Buffler, 1991):

$$\phi_{ed} = \frac{deuterons\ non\ escape}{all\ deuteron\ events} = \frac{r^2 \cos^{-1}\left(\frac{\frac{1}{2}s^2}{r^2} - 1\right) - \frac{1}{2}s\sqrt{4r^2 - s^2}}{\pi r^2} \tag{5.40}$$

where s_1 is the range of deuterons in the NE230 scintillator and r is the radius of the NE230 scintillator. Using Eq. 5.40, the correction factor ϕ_{ed} for incident neutrons of 64 MeV corresponding to deuteron energy of 56.89 MeV was calculated to be 0.288.

Table 5. 5: *Input quantities used to determine the neutron detection efficiency using n-d elastic scattering cross-sections and neutron fluence measured with the NE230 spectrometer.*

E_n (MeV)	L_{cd} (channel)	n_D (barn^{-1})	σ_D (barn)	ϕ_{ndf}	ϕ_{ed}	$N_{nd}(Li)$ (counts)	$N_{nd}(Be)$ (counts)	$N_{nd}(C)$ (counts)
10	4	0.101	0.916	1.000	0.973	12148	66481	138407
12	4	0.101	0.757	1.000	0.962	11201	59125	127654
14	4	0.101	0.644	1.000	0.950	11260	56538	126370
16	4	0.101	0.557	1.000	0.937	10433	51525	118757
18	4	0.101	0.494	1.000	0.922	11136	53964	125175
20	5	0.101	0.440	0.791	0.906	9665	45047	190967
22	12	0.101	0.393	0.579	0.889	6898	31742	113252
24	16	0.101	0.353	0.461	0.871	5295	24128	86213
26	19	0.101	0.316	0.352	0.851	4132	17912	42889
28	23	0.101	0.285	0.295	0.830	3405	14482	33889
30	27	0.101	0.258	0.246	0.807	2764	11545	27441
32	31	0.101	0.236	0.220	0.784	2413	9421	22311
34	36	0.101	0.217	0.197	0.759	1814	7096	16786
36	40	0.101	0.200	0.181	0.733	1486	5903	13305
38	44	0.101	0.186	0.172	0.707	1348	5173	10614
40	48	0.101	0.173	0.157	0.679	1013	3951	6715
42	52	0.101	0.160	0.142	0.650	969	3652	4503
44	56	0.101	0.149	0.128	0.620	793	3510	2448
46	60	0.101	0.139	0.122	0.590	643	4201	1898
48	63	0.101	0.130	0.112	0.558	604	5217	662
50	67	0.101	0.121	0.110	0.526	455	5025	92
52	69	0.101	0.113	0.108	0.493	393	5051	
54	72	0.101	0.106	0.103	0.460	334	4364	
56	75	0.101	0.099	0.103	0.426	224	4113	
58	77	0.101	0.092	0.098	0.392	138	3808	
60	79	0.101	0.086	0.097	0.358	263	3662	
62	82	0.101	0.080	0.096	0.323	388	2127	
64	83	0.101	0.075	0.095	0.288	4333	1102	
66	85	0.101	0.070	0.092	0.254	1497		

(ii) **Neutron fluence calculated using neutron efficiency of NE230 relative to n-p elastic scattering.**

Neutron fluence measured with The NE230 spectrometer using the detection efficiency relative to n-p elastic scattering was obtained from:

$$N_0 = \frac{N_{D'}}{\varepsilon'_D}. \tag{5.41}$$

Where $N_{D'}$ is the integral number of deuterons above L_D for each target at energy range of interest and ε'_D is as defined in section 5.2.1. Using Eq. 5.34 and Eq. 5.41, the neutron fluence measured with the NE230 spectrometer using efficiency ε'_D is given by:

$$\Phi = \frac{N_{D'}}{A\varepsilon'_D} = \frac{N_{np} M_0 N_{D'}}{A N_D M_i \phi_{npf} \phi_{ep} n_H \sigma_H}. \tag{5.42}$$

Input quantities used to determine the measured neutron detection efficiency (relative to n-p elastic scattering) of the NE230 spectrometer and neutron fluence measured with the NE230 spectrometer are presented in table 5.6.
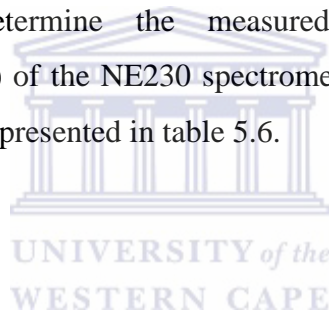
Table 5. 6: *Input quantities used to calculate detection efficiency of NE230 relative to n-p elastic scattering and neutron fluence at energies of interest for each target. The n-p elastic scattering quantities also used in the efficiency calculation are shown in table 5.2.*

E_n (MeV)	$N_{np}(sum)$ (counts)	$N_D(Li)$ (counts)	$N_D(Be)$ (counts)	$N_D(C)$ (counts)	$N_D(sum)$ (counts)
10	377072	12148	66481	138407	217045
12	348159	11201	59125	127654	197983
14	347573	11260	56538	126370	194172
16	314285	10433	51525	118757	180718
18	293363	11136	53964	125175	190281
20	237733	12719	59849	140042	212615
22	228023	14731	69700	162555	246990
24	197598	17654	81076	190018	288750
26	174300	19493	85291	201895	306686
28	139414	19019	80175	185558	284759
30	117917	17252	70961	168232	256451
32	101433	16708	67592	158119	242422
34	81407	16523	64292	149034	229850
36	65843	16240	62252	136160	214655
38	55215	16340	60820	124030	201206
40	37056	14728	54151	91447	160331
42	30940	15114	57225	68933	141280
44	21058	13785	61903	42456	118147
46	22090	14064	83688	38182	135939
48	19334	12722	109952	13296	135970
50	18921	11755	122282	2227	136269
52	15847	9924	114361		126142
54	14121	8764	106454		116812
56	12636	6795	107019		115356
58	10088	3952	96252		101564
60	8824	7294	87023		95189
62	6173	19077	56786		76378
64	6241	124291	23459		147862
66	2347	24421			25223

5.2.3   Estimates of uncertainties in the measurements with the NE230 spectrometer.

The calibration constant k for the NE230 spectrometer calculated was found to be equal to that of the NE213 spectrometer, with the uncertainty calculated using Eq. 5.22 to be about 8% of the value of k. The counting statistics in the pulse height spectra were calculated to be less than 2%. Systematic uncertainties due to loci in the *LS*-plot used to select charged particles of interest, incident neutron energy, neutron ToF windows, and measured peaks and edges in the pulse height spectra were difficult to assess, however fluctuations in repeated measurements were calculated to be less than 3% [Buffler, 1991] [Herbert, 2009]. Eq.5.22 and appropriate statistical evaluations of uncertainties (square root of the estimated value) were used to calculate and estimate uncertainty in each input quantity and are shown in table 5.7 for 64 MeV neutrons. Uncertainties in the neutron detection efficiency of the NE230 spectrometer for n-d elastic scattering ($\varepsilon_D(E_n)$) and efficiency relative to n-p elastic scattering ($\varepsilon'_D(E_n)$) are shown together with neutron fluencies calculated using both efficiencies for the NE230 spectrometer in table 5.8 and 5.9 respectively.

Table 5. 7: *Uncertainty in the each input quantity used in calculations of detection efficiencies for the NE230 spectrometer (using n-d elastic cross-sections and relative to n-p elastic scattering), and neutron fluence at 64 MeV.*

Input quantity	x_i	Δx_i	Uncertainty type	x_{lower}	x_{upper}
N_{nd}	4333	66	A		
N_{np}	6241	79	A		
N_D	147862	385	A		
σ_D	0.075	0.002	B	0.071	0.079
n_D	0.101	0.002	B	0.098	0.106
ϕ_{ndf}	0.095	0.006	B	0.089	0.108
ϕ_{ed}	0.288	0.012	B	0.274	0.317
A	4.909	0.106	B	4.786	5.154

Table 5. 8: *Detection efficiency calculated using n-d elastic scattering and neutron fluence, together with their associated uncertainty.*

E_n (MeV)	ε_D 10^{-2}	$\Delta\varepsilon_D$ 10^{-3}	$\Phi(Li)$ $(n.cm^{-2})$ 10^3	$\Delta\Phi(Li)$ $(n.cm^{-2})$ 10^3	$\Phi(Be)$ $(n.cm^{-2})$ 10^3	$\Delta\Phi(Be)$ $(n.cm^{-2})$ 10^3	$\Phi(C)$ $(n.cm^{-2})$ 10^3	$\Delta\Phi(C)$ $(n.cm^{-2})$ 10^3
10	9.25	5.74	28	2	150	12	313	25
12	7.65	4.74	31	2	164	13	353	28
14	6.50	4.03	37	3	186	15	417	33
16	5.63	3.49	40	3	199	16		
18	4.99	3.10	49	4	239	19	459	36
20	3.51	2.18	62	5	288	23	554	44
22	2.30	1.43	57	5	264	21	677	53
24	1.64	1.02	64	5	290	23		
26	1.12	0.70	88	7	382	30	622	49
28	0.85	0.53	99	8	420	33	692	55
30	0.64	0.40	109	9	453	36	913	72
32	0.52	0.33	120	10	467	37		
34	0.43	0.27	113	9	442	35	982	77
36	0.37	0.23	113	9	448	36	1078	85
38	0.32	0.20	120	10	461	37	1106	87
40	0.27	0.17	111	9	434	35		
42	0.23	0.14	132	11	498	40	1044	83
44	0.19	0.12	135	12	599	48	1010	80
46	0.17	0.11	130	11	847	68	945	75
48	0.15	0.09	150	13	1298	104	737	59
50	0.13	0.08	131	12	1447	116		
52	0.12	0.08	132	13	1697	145	613	49
54	0.11	0.08	135	14	1766	151	418	34
56	0.10	0.07	105	11	1923	164	383	31
58	0.09	0.06	79	9	2182	187		
60	0.08	0.06	178	19	2475	212	165	14
62	0.08	0.05	314	31	1720	149	27	3
64	0.07	0.05	4257	364	1083	97		
66	0.07	0.04	1846	162				

Table 5. 9: *Detection efficiency calculated relative to n-p elastic scattering and neutron fluence, together with their associated uncertainties.*

E_n (MeV)	ε'_D	$\Delta\varepsilon'_D$	$\Phi(Li)$ $(n.cm^{-2})$ 10^3	$\Delta\Phi(Li)$ $(n.cm^{-2})$ 10^3	$\Phi(Be)$ $(n.cm^{-2})$ 10^3	$\Delta\Phi(Be)$ $(n.cm^{-2})$ 10^3	$\Phi(C)$ $(n.cm^{-2})$ 10^3	$\Delta\Phi(C)$ $(n.cm^{-2})$ 10^3
10	0.053	0.0036	47	3	257	19	535	39
12	0.044	0.0030	52	4	276	19	596	43
14	0.036	0.0025	63	5	318	23	706	51
16	0.032	0.0022	66	5	325	23	748	54
18	0.031	0.0021	73	5	356	26	826	60
20	0.031	0.0021	84	6	394	28	923	67
22	0.031	0.0021	98	7	464	33	1082	78
24	0.033	0.0022	110	8	507	36	1188	86
26	0.031	0.0022	126	9	553	39	1309	94
28	0.030	0.0021	129	9	544	39	1258	91
30	0.026	0.0018	134	10	551	39	1307	94
32	0.024	0.0017	140	10	567	40	1328	96
34	0.024	0.0016	143	10	557	40	1292	93
36	0.023	0.0016	145	11	558	40	1220	88
38	0.021	0.0015	157	11	584	42	1190	86
40	0.021	0.0014	143	10	526	38	889	64
42	0.019	0.0013	161	12	611	44	736	53
44	0.020	0.0014	141	10	634	45	435	32
46	0.018	0.0012	159	12	944	68	431	31
48	0.017	0.0012	150	11	1296	93	157	11
50	0.015	0.0010	164	12	1704	123	31	2
52	0.014	0.0010	148	12	1699	134		
54	0.012	0.0009	149	12	1807	142		
56	0.010	0.0008	134	11	2111	166		
58	0.009	0.0007	86	7	2085	165		
60	0.008	0.0006	193	15	2302	182		
62	0.007	0.0005	589	47	1753	139		
64	0.009	0.0007	2696	215	509	40		
66	0.003	0.0002	1758	144				

6.   RESULTS AND DISCUSSION

In this section neutron fluence spectra measured with NE213 (proton recoil spectrometry) are compared with those measured with NE230 (deuteron recoil spectrometry). The black solid square-line histograms in figures 6.1, 6.2 and 6.4 represent neutron fluence spectra measured with the NE213 spectrometer. The red circle-line histograms in figures 6.1, 6.2, and 6.5 represent neutron fluence spectra measured with the NE230 spectrometer where all events were selected in the pulse height spectra to determine the efficiency and neutron fluence measured with the NE230 spectrometer. The blue triangle-line histograms in figures 6.1, 6.4, and 6.5 represent results measured with the NE230 spectrometer selecting only n-d elastic scattering events in the pulse height spectra and using the calculated detection efficiency (n-d cross-sections) of the NE230 spectrometer for determination of neutron fluence spectra.

All neutron fluence spectra measured with NE230 compared with neutron fluence spectra measured with NE213 were normalised to the number of events measured by the neutron monitor during measurements with NE213 for each respective target (refer to table 3.2), and are presented in figures 6.1, 6.2, and 6.4 (a)-(c). Neutron fluence spectra measured with NE230 determined using the detector efficiency of the NE230 spectrometer relative to n-p elastic scattering (measured efficiency) are also compared with those measured with NE230 determined using the detector efficiency of the NE230 spectrometer calculated using cross-sections for n-d elastic scattering (calculated efficiency). For comparison of neutron spectra measured with the NE230 spectrometer (fig 6.5), results were normalised to the number of events measured by the neutron monitor during NE230 measurements (refer to table 3.2).

In order to facilitate the comparison in detail, ratios of neutron fluence at different neutron energies calculated are shown in table 6.1 and in addition are plotted and shown in figures 6.3, 6.6 and 6.7. Uncertainties associated with each neutron fluence spectra were calculated as discussed previously (refer to section 5.1.3 and 5.2.3) and are shown as error bars in each spectrum. The uncertainties associated with the ratios were calculated using quadratic summation   (refer to section 5.1.3 for discussion).

Figure 6.1 shows neutron fluence spectra measured with the NE213 and the NE230 spectrometers for (a) (1 mm) ^{7}Li target, (b) (10 mm) ^{9}Be target, and (c) (10 mm) ^{12}C target. Neutron fluence spectra measured with the NE230 spectrometer using measured efficiency, with all events in the pulse height spectra selected (labelled all events), and those determined

using the calculated efficiency, selecting n-d event in the pulse height spectra (labelled calc n-d events) are included in fig 6.1 (a)-(c). Each spectra in fig 6.1 (a)-(c) show expected trends, that is in each spectra prominent peaks due to most energetic neutrons lie in the expected energy range (refer to 4.1.1. for detailed discussion) and low energy neutrons lie in the tail of each spectrum, thus each spectra exhibits the expected shape. Neutron fluence spectra for ^{9}Be target exhibit broader prominent peak, with a broader distribution exhibited for the ^{12}C target (graphite), which is in addition to other factors is attributed to target thickness. For clear visual comparison, results in fig 6.1 are paired for each target.

Neutron fluence spectra measured with the NE213 spectrometer are compared to neutron fluence spectra measured with the NE230 spectrometer with all events in the pulse height spectra selected and using the measured efficiency to determine neutron fluence (fig 6.2), and neutron fluence spectra measured with the NE230 spectrometer selecting only n-d elastic scattering events in the pulse height spectra and using the calculated efficiency (using cross-sections for n-d elastic scattering) to determine neutron fluence (fig 6.4). In addition results measured with NE230 for both, all events using measured efficiency and n-d elastic scattering events using efficiency calculated from n-d cross-sections are compared with each other (fig 6.5).

From results in figure 6.2, neutron fluence spectra for ^{9}Be target and ^{12}C target (fig 6.2 (b) and (c)) show better agreement compared to ^{7}Li target neutron fluence spectra (fig 6.2 (a)). For results in figure 6.2 (a), below 20 MeV, there is a good agreement between the neutron fluence spectra for ^{7}Li target measured with the two spectrometers (NE213 and the NE230 spectrometer). Based on the ratios (table 6.1), the overall disagreement in this energy range is calculated to be around 5% Above 20 MeV, the disagreement worsen to around 13% for neutron energies of up to 58 MeV and 17% for energies of up to 64 MeV.

From figure 6.2 (b), at neutron energies below 20 MeV, there is a satisfactory agreement between the results measured with each spectrometer, with overall disagreements calculated to be about 15%. The agreement however improves between neutron energies 22-44 MeV with disagreements calculated be about 13% at this range and 4% at neutron energies 46-62 MeV. The improved agreement may be attributed to improving counting statistics for events in the pulse height spectra measured with the NE230 spectrometer (refer to table 5.5), there is also a notable disagreement at neutron energy 64 MeV (fig 6.2 (b)), this is
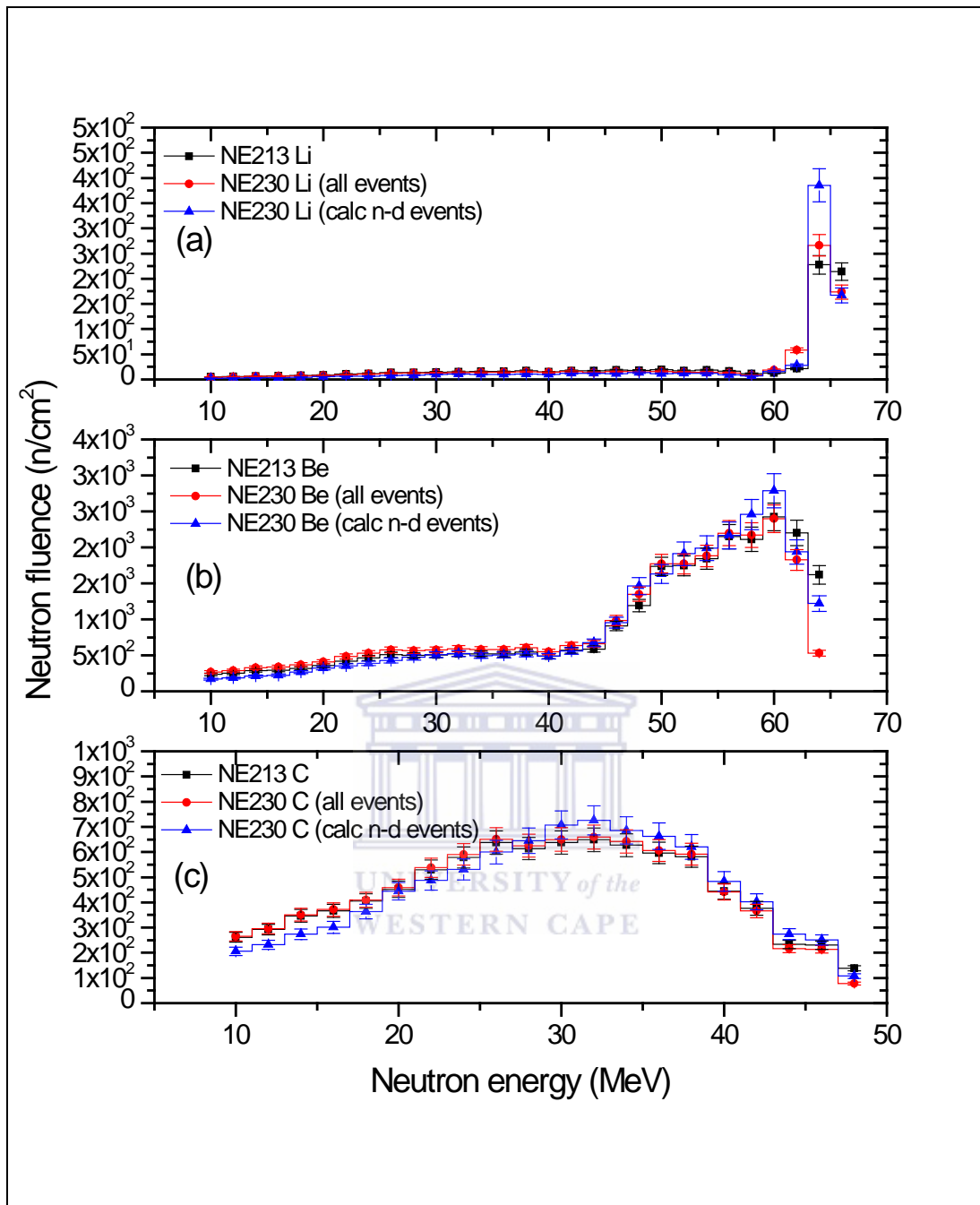
Figure 6. 1*: A comparison of neutron fluence spectra measured with NE213 (black-line histogram) and NE230 with all events selected for neutron fluence determination (red-line histogram) and measured with NE230 with only n-d elastic scattering events selected for neutron fluence determination (blue-line histogram).*
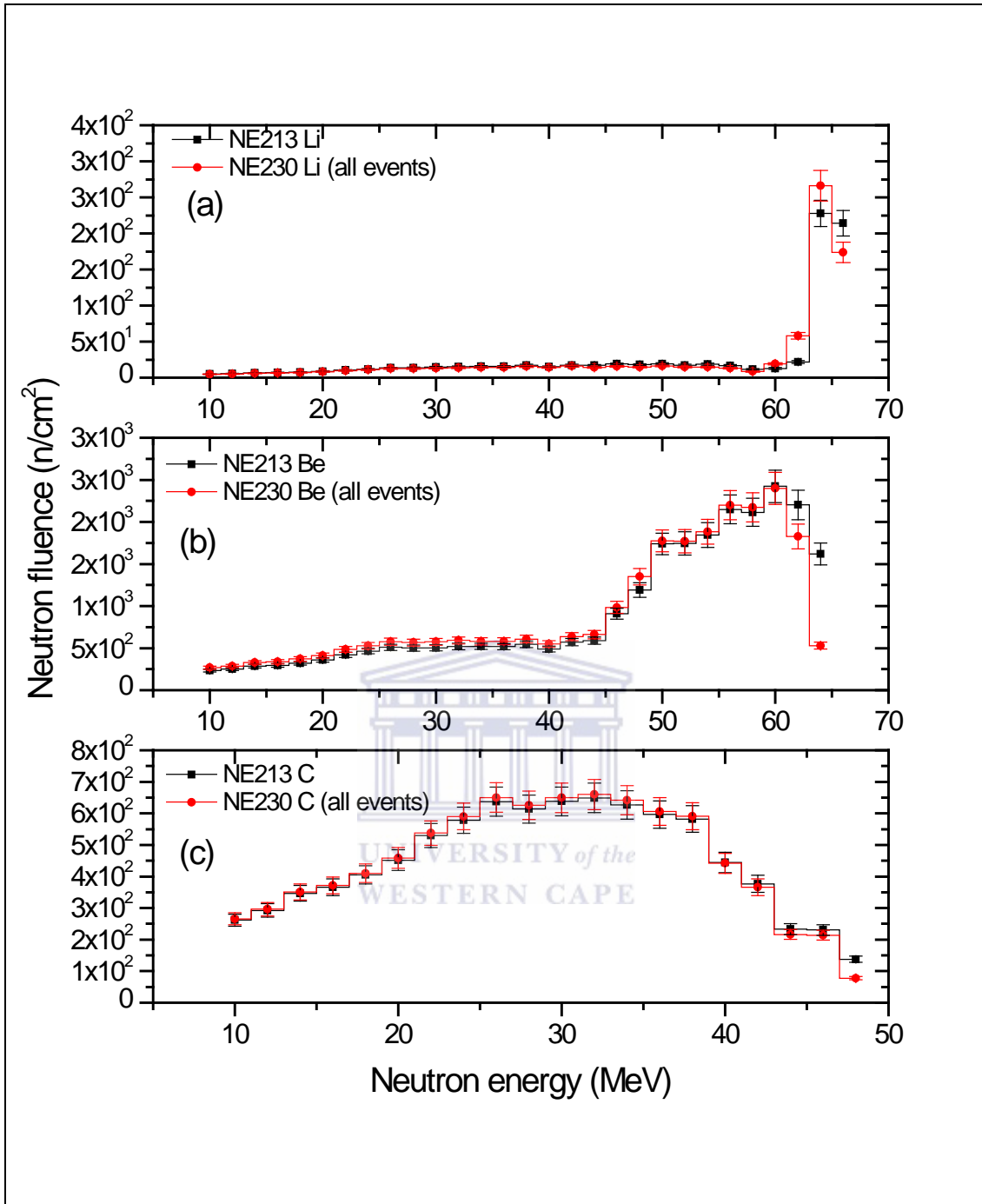
Figure 6. 2: *A comparison of neutron fluence spectra measured with the NE213 spectrometer (black-line histogram) and the NE230 spectrometer (red-line histogram) with all events selected for determination of neutron fluence spectra.*

Table 6. 1: *Ratios of neutron fluence spectra measured with the NE213 and the NE230 spectrometers*

Energy (MeV)	Ratio of NE213 and NE230 (all events)			Ratio of NE213 and NE230 (calculated n-d events)			Ratio of NE230 (all events and (calculated n-d events)		
	Li	Be	C	Li	Be	C	Li	Be	C
10	0.948	1.137	1.015	0.509	0.720	0.785	0.537	0.634	0.774
12	0.94	1.147	1.013	0.510	0.735	0.793	0.543	0.641	0.782
14	0.977	1.148	1.012	0.529	0.733	0.789	0.541	0.638	0.780
16	0.938	1.15	1.015	0.527	0.763	0.822	0.562	0.663	0.810
18	0.943	1.158	1.012	0.580	0.840	0.897	0.615	0.725	0.886
20	0.946	1.147	1.015	0.639	0.906	0.983	0.676	0.790	0.968
22	0.923	1.154	1.015	0.593	0.850	0.920	0.642	0.737	0.907
24	0.92	1.136	1.02	0.577	0.834	0.918	0.627	0.734	0.900
26	0.932	1.132	1.02	0.595	0.845	0.941	0.639	0.746	0.922
28	0.927	1.131	1.019	0.651	0.944	1.050	0.702	0.835	1.031
30	0.907	1.14	1.018	0.673	1.014	1.109	0.743	0.889	1.089
32	0.914	1.137	1.017	0.714	1.012	1.119	0.781	0.890	1.100
34	0.907	1.115	1.024	0.655	0.955	1.093	0.723	0.857	1.068
36	0.922	1.121	1.016	0.655	0.974	1.111	0.711	0.869	1.093
38	0.893	1.115	1.016	0.627	0.952	1.066	0.702	0.853	1.049
40	0.941	1.121	0.994	0.670	0.998	1.088	0.712	0.891	1.095
42	0.919	1.114	0.971	0.689	0.981	1.068	0.750	0.880	1.101
44	0.818	1.124	0.926	0.719	1.149	1.175	0.879	1.022	1.269
46	0.827	1.083	0.929	0.620	1.050	1.089	0.749	0.970	1.173
48	0.826	1.135	0.565	0.759	1.229	0.784	0.919	1.083	1.389
50	0.838	1.021		0.615	0.938		0.734	0.919	
52	0.842	1.014		0.691	1.095		0.821	1.079	
54	0.79	1.021		0.658	1.079		0.833	1.056	
56	0.798	1.023		0.572	1.008		0.716	0.985	
58	0.728	1.028		0.617	1.163		0.847	1.132	
60	1.49	0.99		1.258	1.151		0.844	1.162	
62	2.687	0.829		1.313	0.880		0.488	1.061	
64	1.17	0.327		1.694	0.754		1.448	2.301	
66	0.811			0.781			0.962		

Figure 6. 3: *Ratio of fluence measured with the NE213 spectrometer and the NE230 spectrometer for the measured efficiency relative to the efficiency of the NE213 spectrometer.*

due to the poor statistics in the pulse height spectrum at 64 MeV for ^{9}Be target, thus a drop in event statistics.

There is a good agreement between neutron fluence spectra for graphite target (fig 6.2 (c)), with overall disagreement calculated using ratios to be 2% below 38 MeV and 5% above this neutron energy (38 MeV). Disagreement between neutron fluence measurements with both the NE213 and the NE230 spectrometers may be attributed to: particle escape (proton and deuteron respectively) in the scintillators, this may affect the results since there was no correction for deuteron escape in the neutron fluence spectra measured with the NE230 spectrometer and only forward recoiling protons could be corrected for in the measurements with NE213 (refer to appendix B). For the graphite target results, there is less particle escape since only up to 48 MeV neutrons are produced by the target, thus less particle escape at this energy range, hence a better agreement. There seems to be an improvement in comparison for results measured with the NE230 spectrometer to those measured with the NE213 spectrometer with good event statistics.

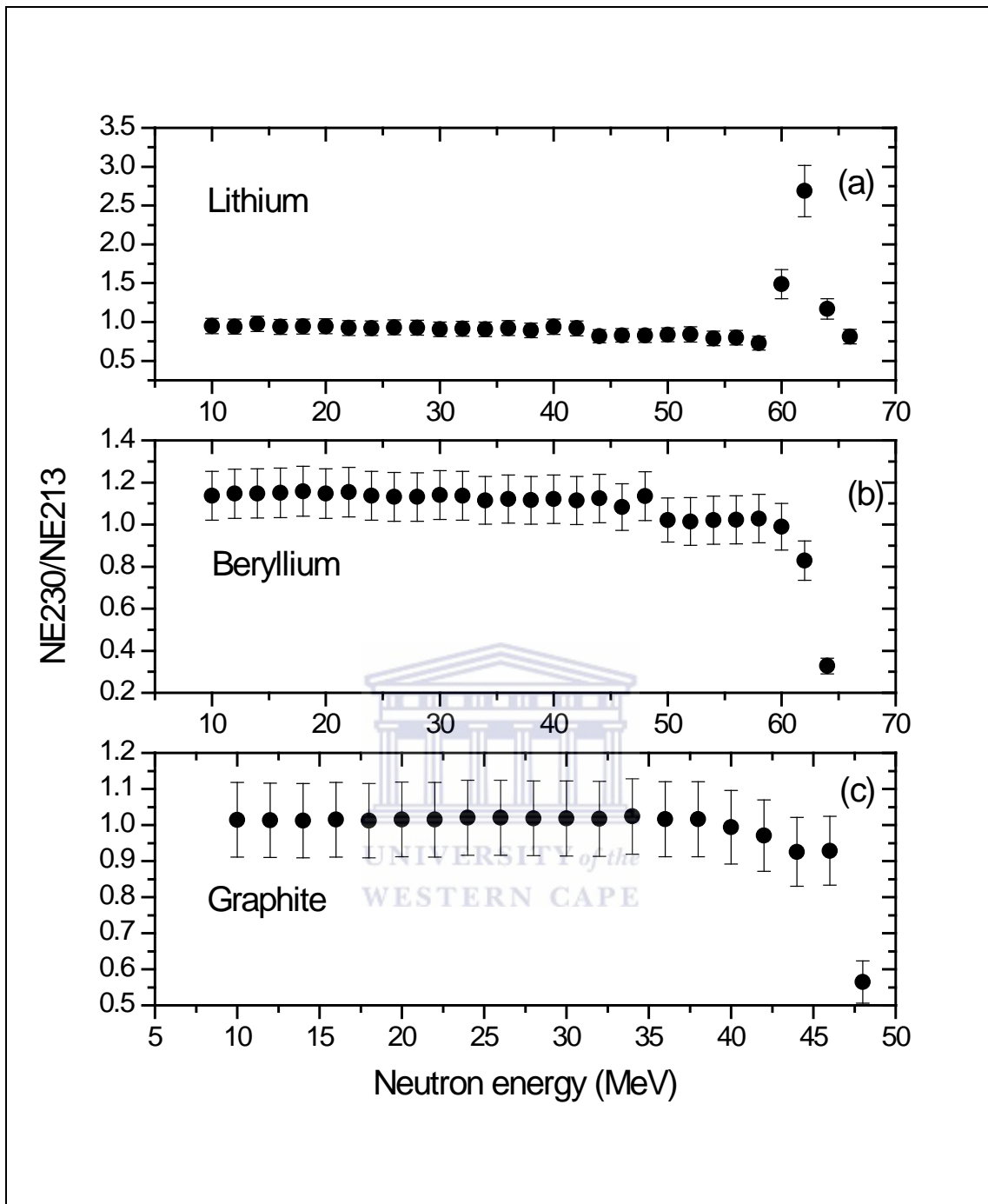The comparison of neutron fluence spectra measured with the NE213 spectrometer and with the NE230 spectrometer selecting only n-d elastic events in the pulse height spectra using the efficiency calculated using cross-section for n-d elastic scattering (theoretically calculated efficiency) are shown in figure 6.4. The disagreements between spectra can be clearly seen below 30 MeV, clearly noticeable in fig 6.4 (b) and (c). This may be attributed to the n-d elastic scattering events which are dominant at this energy range with high event statistics (event counts). The agreement between the spectra improves above 30 MeV, with overall disagreement calculated to be 34 % and 29% above 60-62 MeV, 0.3% to 9% between 32-44 MeV and 46-62 MeV, and 10% in fig 6.4 (a), (b) and (c) respectively. The disagreement was calculated to be about 69% for result at 64 MeV for the ^{7}Li target.

The improvement in agreement (fig 6.6 (a)-(c)) is not steady below 58 MeV, 60 MeV and 46 MeV for each respective target, however the disagreements worsen above these energies as clearly seen in fig 6.6 (a)-(c). The overall disagreement in these results (fig 6.4 (a)-(c)) may be attributed to the difficulty in the selection of n-d elastic scattering events due to increasing contribution of deuterons from to n-^{12}C interactions in the pulse height spectra measured with the NE230 spectrometer. Large uncertainties in the estimated differential reaction cross-sections for n-d elastic scattering may also be a contributing factor in these disagreements and particle escape effect for neutron fluence spectra measured with both the NE213 and the NE230 spectrometers.

Figure 6.5 shows a comparison of neutron fluence spectra for all targets (fig 6.5 (a)-(c)) measured with the NE230 spectrometer, results for n-d elastic events using the efficiency calculated from n-d elastic scattering cross-sections are compared to those for all events using measured efficiency relative to n-p elastic scattering. Below 30 MeV there is an underestimation of neutron fluence determined from n-d elastic scattering events, this can be clearly seen in fig 6.5 (b) and (c). These disagreements may be attributed to selection of n-d elastic scattering events in the pulse height spectra (refer to fig 4.25), at this energy range there are up to no contribution of deuterons from n-^{12}C interactions resulting in high event statistics. The disagreements at this energy range were calculated to be about 38%, 27% and 10% for fig 6.5 (a), (b), and (c) respectively.

There is an improvement in the results above 30 MeV, with overall disagreement calculated to be 22% for 32-60 MeV in the ^{7}Li target spectra (fig 6.5 (a)), 11% to 5% at 32-44 MeV and 46-62 MeV for ^{9}Be target spectra (fig 6.5 (b)) respectively, and 15% for the graphite target neutron fluence spectra. The improving agreement with energy increase is reasonably steady below 58 MeV, 60 MeV and 46 MeV for each target respectively (fig 6.7 (a)-(c)), however above these energies the agreement worsen non steadily as seen in fig 6.7 (a)-(c).

Lower event statistics (event counts) for n-d elastic scattering events, caused by increasing contribution of deuterons from n-C interactions and escaping deuterons, result in an increase in neutron fluence determined from n-d elastic scattering events using the efficiency calculated from n-d elastic scattering cross-sections, improving the agreement between neutron fluence spectra (fig 6.5). For the ^{7}Li target (fig 6.5 (a)), the apparent increase in event counts (N_{nd}) at 62-64 MeV worsen the agreement, with the disagreement calculated to be about 48%. In addition to event statistics brought about by selection of events in the pulse height spectra, the disagreements in the results may also be attributed to large uncertainties in the estimated reaction differential cross-sections for n-d elastic scattering and deuteron escape which was not corrected for in results determined from the selection of all events in the pulse height spectra measured with the NE230 spectrometer.

Figure 6. 4: *A comparison of neutron fluence spectra measured with the NE213 spectrometer (black-line histogram) and the NE230 spectrometer (blue-line histogram). The neutron fluence measured with NE230 was determined from n-d elastic scattering events using the efficiency calculated using reaction cross-section for n-d elastic scattering.*
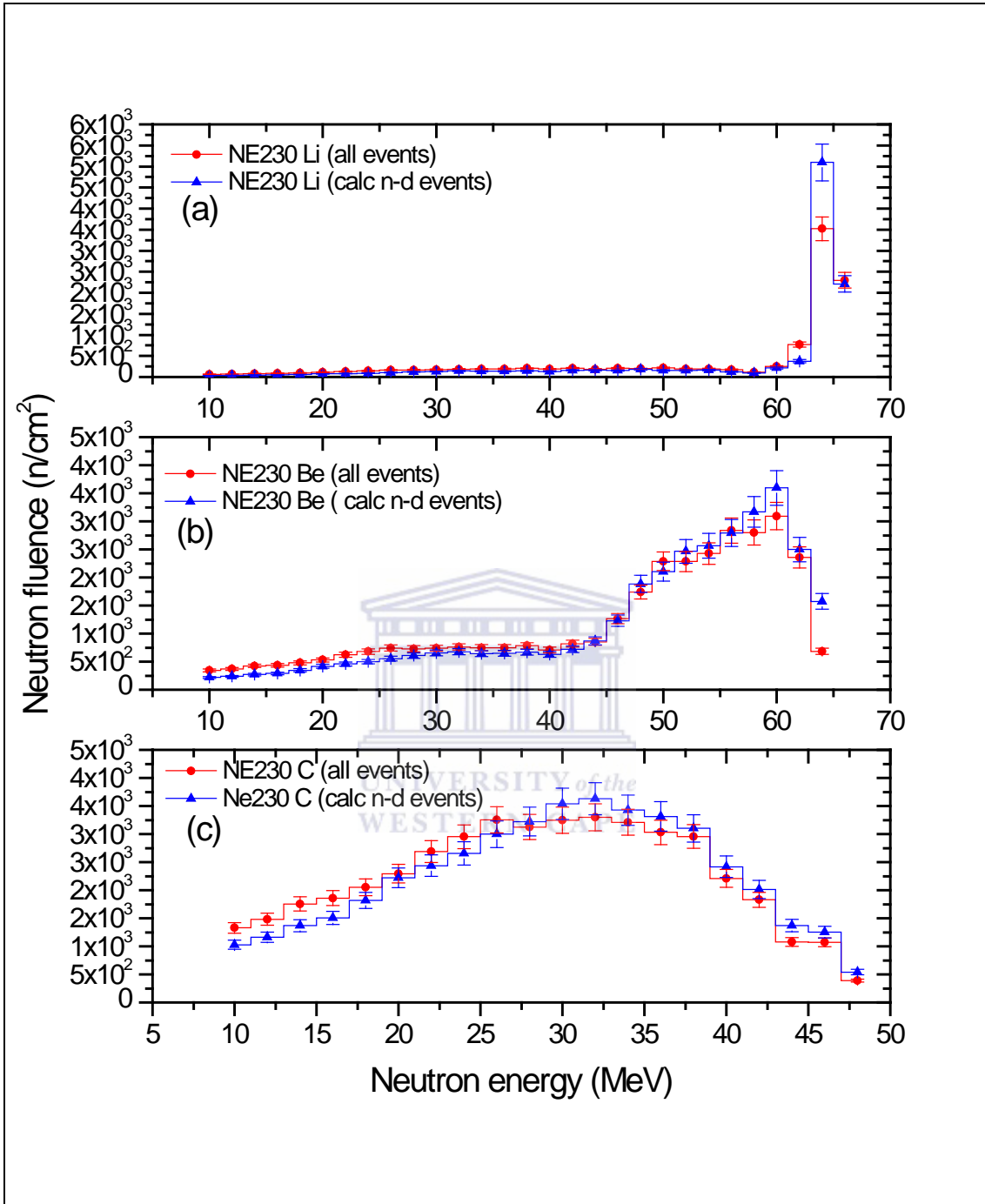
Figure 6. 5: *A comparison of neutron fluence spectra measured with the NE230 spectrometer. The red-line histogram represents results for neutron fluence determined from selecting all events with results determined from selecting only n-d elastic scattering events is represented by blue-line histograms.*
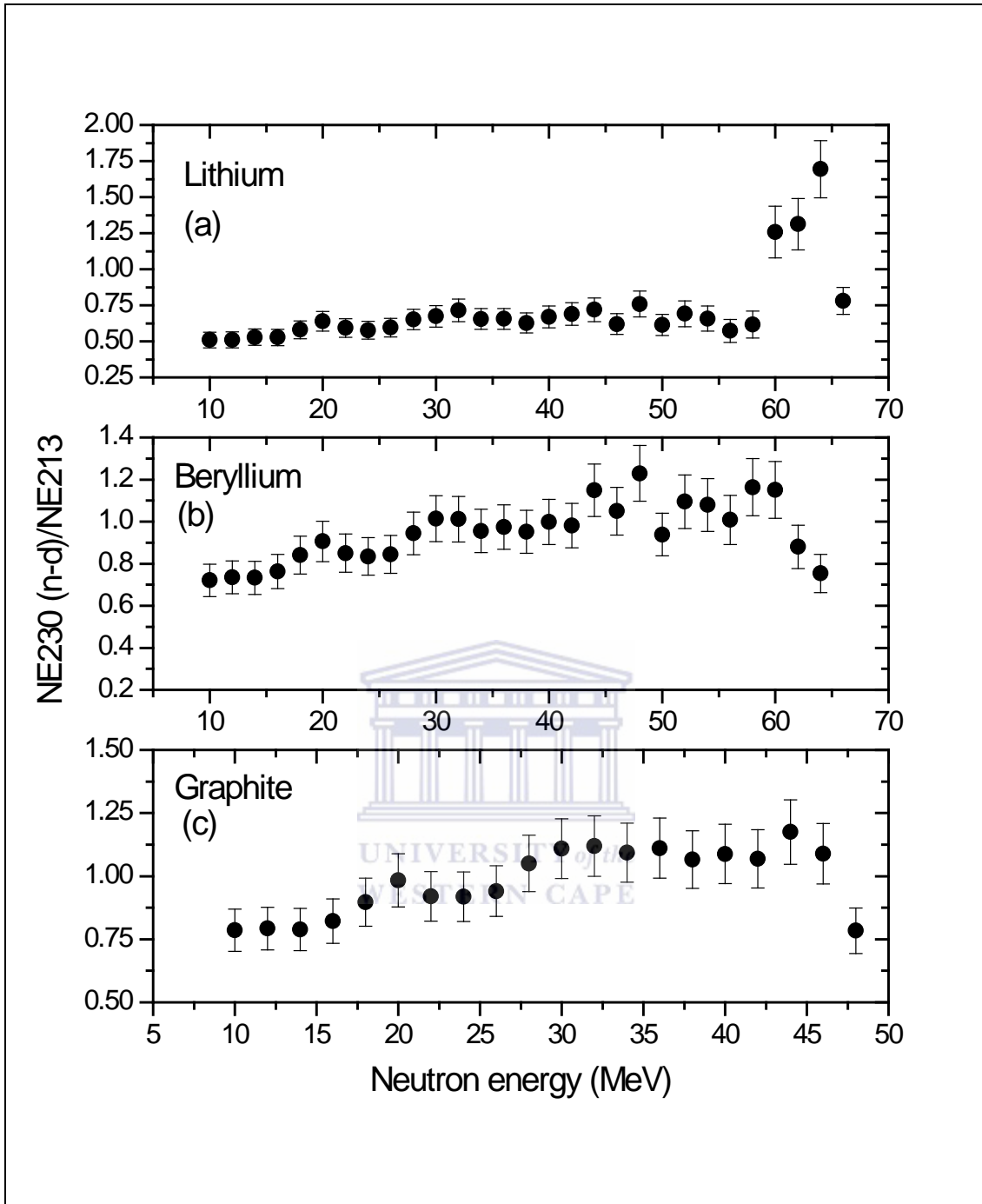
Figure 6. 6: Ratio of neutron fluence measured with the NE213 spectrometer and the NE230 spectrometer. The results measured with NE230 are neutron fluence determined by selecting n-d elastic events and using the detector efficiency of NE230 using n-d cross-sections.
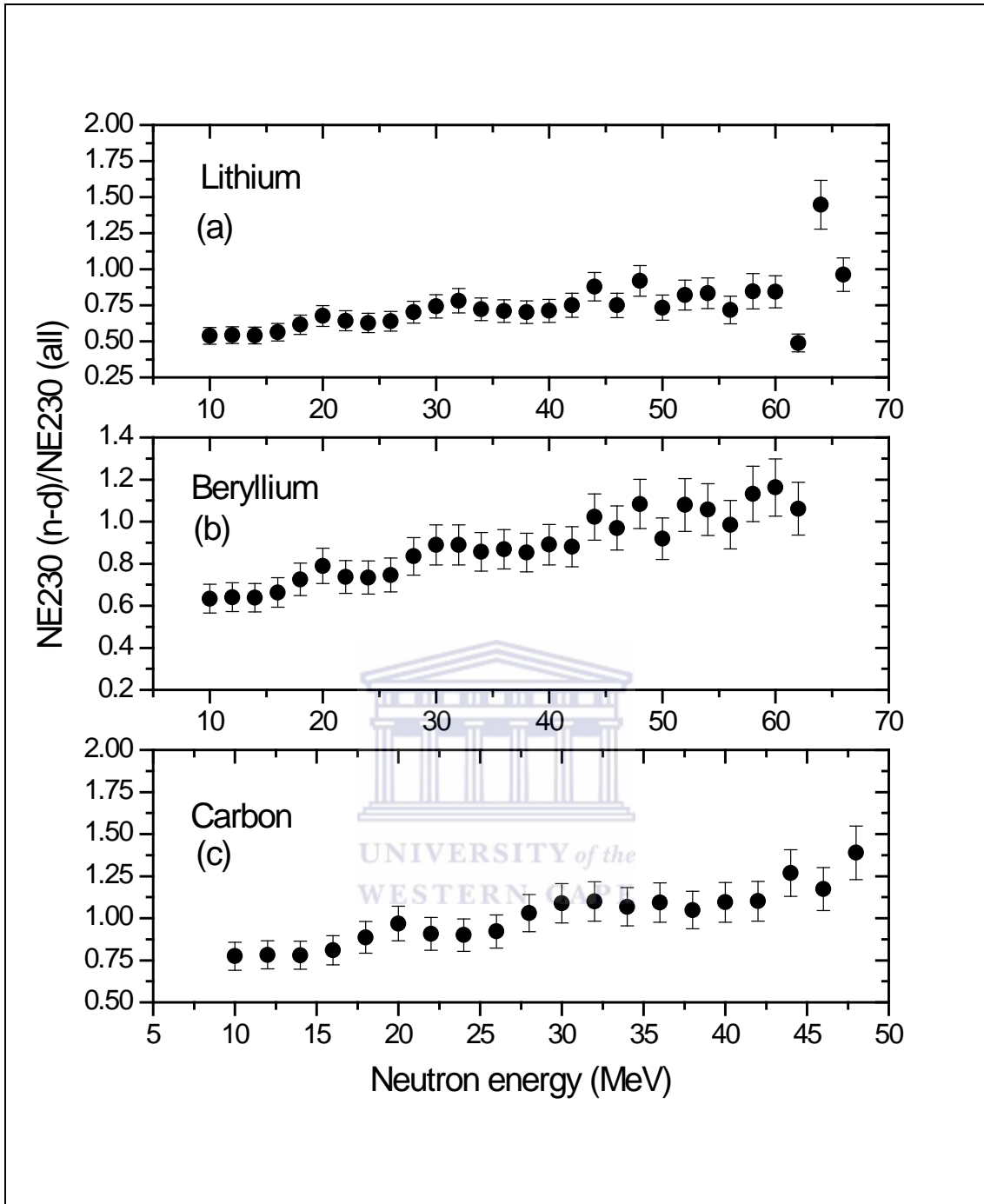
Figure 6. 7: *Ratio of neutron fluence measured with the NE230 spectrometer, for neutron fluence determined from selecting all events and n-d elastic scattering events.*

6 CONCLUSIONS

6.1 Conclusions

The purpose of this work was to measure neutron fluence spectra in air with NE213 (proton recoil spectrometer) and NE230 (deuteron recoil spectrometer), and compare the measured neutron fluence spectra. For measurements with the NE230 spectrometer, results where all events in the pulse height spectra were selected using the measured efficiency ($\varepsilon_D'(E_n)$) and only n-d elastic scattering events using the efficiency calculated from n-d elastic cross-sections ($\varepsilon_D(E_n)$) were compared with each other. The results (neutron fluence spectra measured with the NE213 spectrometer and the NE230 spectrometer (all and calc n-d events)) showed good comparison with each other. The comparison between neutron fluence spectra measured with the NE213 spectrometer and the NE230 spectrometer for all events had a better agreement compared to those measured with the NE213 spectrometer and the NE230 spectrometer for n-d elastic scattering events using calculated efficiency from n-d elastic scattering cross-sections. It was also noted that neutron fluence spectra measured with the NE230 spectrometer for n-d elastic scattering events using the calculated efficiency using n-d elastic scattering cross-sections compared better with those measured with the NE213 spectrometer than with those measured with the NE230 spectrometer for all events using measured efficiency. This is thought to be due to particle escape correction in the results measured with the NE213 spectrometer and the NE230 spectrometer for n-d elastic scattering events. The conclusion on the overall effect of particle escape on results measured with each spectrometer could not be reached however since both detectors are of different sizes (5 cm $\times$ 5 cm for the NE213 scintillator and 2.5 cm $\times$ 2.5 cm for NE230 scintillator).

Neutron fluence spectra measured with the NE230 spectrometer selecting only n-d elastic scattering events using the measured efficiency (labelled n-d events), are compared in figure 7.1 to results measured with the NE213 spectrometer and the NE230 spectrometer selecting n-d elastic scattering events using the calculated efficiency from n-d cross-sections for elastic scattering. There is a good agreement between the neutron fluence spectra measured with the NE230 spectrometer for n-d events and results measured with the NE213 spectrometer. The measured efficiency used to determine the neutron fluence for the n-d elastic scattering events is discussed in appendix A.
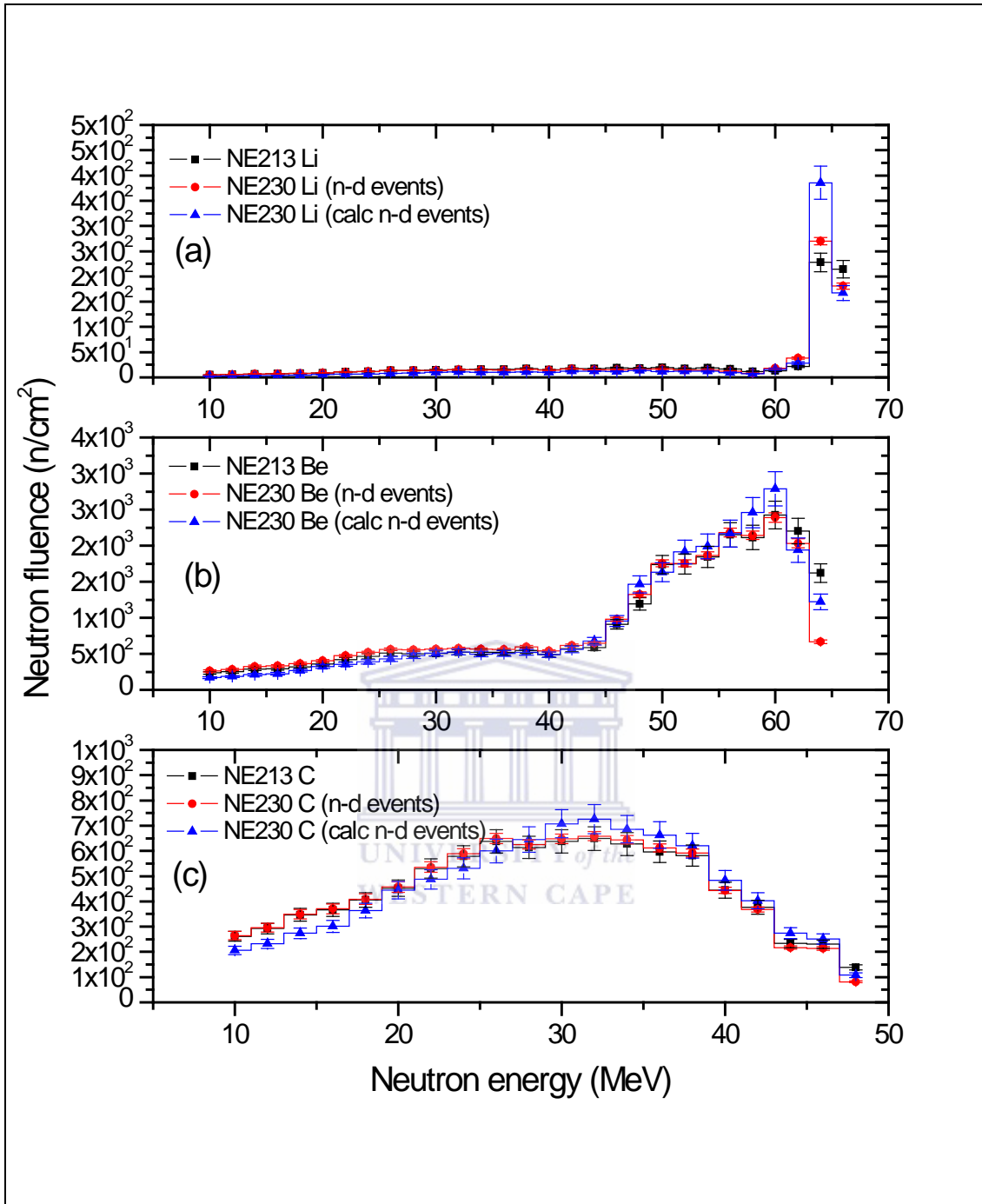
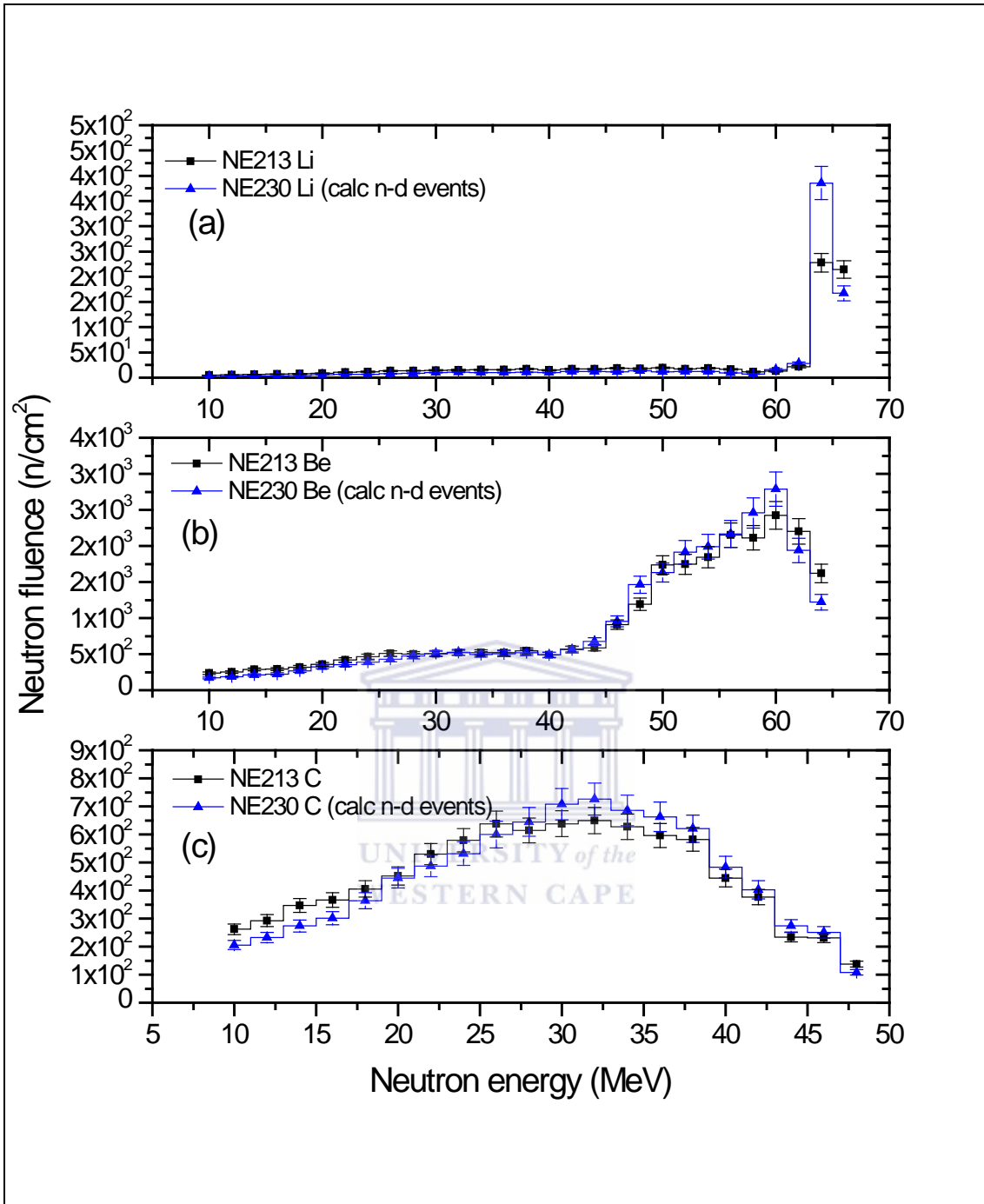***Figure 7. 1:*** *A comparison of neutron fluence spectra measured with the NE213 spectrometer (black-line histogram) and the NE230 spectrometer with n-d events selected for neutron fluence determination (pink-line histogram) and measured with the NE230 spectrometer with only n-d elastic scattering events selected for neutron fluence determination (blue-line histogram).*

Although the efficiencies for the NE230 spectrometer calculated using n-d elastic scattering cross-sections and that determined using n-d elastic events relative to the efficiency of the NE213 spectrometer compare well, there seems to be disagreements in the results for neutron

fluence spectra obtained using these efficiencies. The disagreements are similar to those of results for neutron fluence determined using the calculated efficiency and measured efficiency of the NE230 spectrometer (refer to fig 6.5). From this a conclusion can be reached that the selection of n-d elastic scattering events using the measured efficiency for n-d events does not carry a significant effect on the neutron fluence spectra measured with the NE230 spectrometer.

Based on the better agreement with results measured with the NE213 spectrometer, good knowledge about reaction cross-sections for n-p elastic scattering, unavailability of differential cross-section for n-d elastic scattering across the energy range of interest, it is recommended that for both in air and in-situ measurements of neutron fluence spectra, selection of all events or n-d elastic scattering events with detector efficiency relative to n-p elastic scattering (relative to efficiency of The NE213 spectrometer) be used to determine energy spectra measured with the NE230 spectrometer. Results with the NE230 spectrometer for n-d elastic scattering however provide encouragement, thus with good knowledge about differential cross-sections for n-d elastic scattering and improved event selection in the pulse height spectra, there is an expectation of improvement in the results. The results measured with NE230 in air show that the NE230 can be used as a spectrometer in air using the ToF technique with recoil spectrometry.

6.2 Future Work

One of the objectives in this work was to observe the effect of particle escape on the neutron fluence spectra measured with each detector (NE213 and The NE230 spectrometers), the results were inconclusive as discussed. To study the effect of particle escape, an experiment using detectors (NE213 and The NE230 spectrometers) of the same size was carried out in 2013 at iThemba LABS in South Africa, from which the data is still to be analysed. Further work still needs to be done in unfolding the pulse height spectra measured with the NE230 spectrometer in air, and a detailed study of response of the NE230 spectrometer to different charged particles to aid better selection of events. The major challenge with measurements using the NE230 spectrometer are the differential cross-section for n-d elastic scattering, which are unavailable across energy range of interest as discussed (refer to section 4.2.2). It is therefore highly recommended that measurements and calculations of nuclear reaction differential cross-sections for n-d elastic scattering be given more attention to encourage and exploit potential advantages of the NE230 spectrometer has over widely used the NE213

114

spectrometer, as this will aid an independent use of the NE230 spectrometer as demonstrated by the results using cross-sections for n-d elastic scattering in this work.

APPENDIX A

Detection efficiency of the the NE230 spectrometer for n-d elastic scattering events relative to the detection efficiency of The NE213 spectrometer.

The detection efficiency of the NE230 spectrometer for n-d elastic scattering events relative to n-p elastic scattering can be determined analogues to the of The NE230 spectrometer relative to n-p elastic scattering discussed in 5.2.1.

Consider the NE230 spectrometer exposed to the same beam of mono-energetic neutrons of energy E_n as in the case of the NE213 spectrometer (refer to figure 5.1). We can express the detection efficiency of the NE230 spectrometer for detecting neutrons above pulse height L_{cd} as:

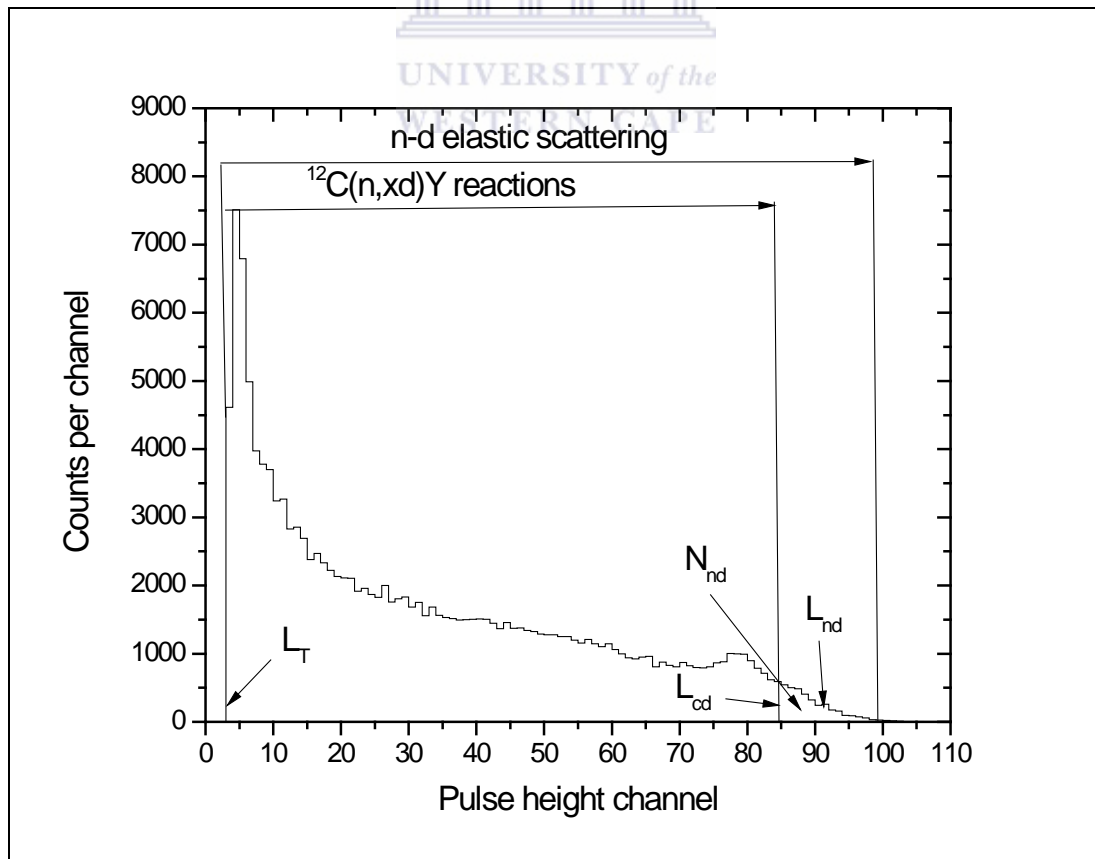$$\varepsilon'_{nd}(E_n) = \frac{N_{nd}}{N_0} \tag{A.1}$$

Figure A- 1: Pulse height spectrum measured with NE230 for incident neutrons of 64MeV.

Where, N_{nd} is the number of deuteron events detected above pulse height threshold L_{cd} as shown in figure A-1 and N_0 is the number of mono-energetic neutrons incident on the NE230 spectrometer.

Rearranging A.1 we obtain:

$$N_{nd} = \varepsilon'_{nd}(E_n)N_0 \tag{A.2}$$

The detection efficiency of the NE230 spectrometer was determined from the ratio N_{nd}/N_{np} and is given by:

$$\frac{N_{nd}}{N_{np}} = \frac{\varepsilon'_{nd}(E_n)N_0}{\varepsilon_H(E_n)N_{np}} \tag{A.3}$$

The experimentally measured efficiency of the NE230 spectrometer for n-d elastic scattering events relative to n-p elastic scattering is given by:

$$\varepsilon'_{nd} = \frac{N_{nd}}{N_{np}} \frac{N_i}{N_0} \phi_{npf} \phi_{ep} n_H \sigma_H \tag{A.4}$$

Normalizing N_i and N_0 to the same number of neutrons counted using a neutron monitor, Eq. A.4 becomes:

$$\varepsilon'_{nd} = \frac{N_{nd}}{N_{np}} \frac{M_i}{M_0} \phi_{npf} \phi_{ep} n_H \sigma_H \tag{A.5}$$

Where ϕ_{npf}, ϕ_{ep} , σ_H, n_H and N_{np} are as defined previously (refer to 5.1.1), M_i is the number of neutrons recorded by the neutron monitor (the NE213 spectrometer) during measurements of N_i using the NE213 spectrometer and M_0 using the NE230 spectrometer. The integral counts from the pulse height spectra of the sum targets for both the NE213 and the NE230 spectrometers were used to calculate the efficiency of the NE230 spectrometer.

(a) M_i and M_0 number of neutrons recorded by the neutron monitor.

The number of neutrons M_i recorded by the neutron monitor taken as the integral count over all target measurements during the NE213 spectrometer measurements was 35664. The reading M_o recorded by the neutron monitor during measurements using the NE230 spectrometer was 89166.

(b) N_{nd}: Integral of counts measured above pulse height threshold L_{cd} measured with the NE230 spectrometer.

The integral number of counts above pulse height L_{cd} was taken as the integral of all deuteron events in the pulse height spectrum (see figure A-1). At 64 MeV incident neutrons N_{nd} was determined to be 5448 for the spectrum of the sum target.

The detection efficiency of the NE230 spectrometer for n-d elastic scattering events relative to n-p elastic scattering cross-section is shown in figure A-2. The uncertainties in the detection efficiency are discussed in 5.2.3. The detection efficiency curve show expected trend for n-d elastic scattering. Similar to the efficiency of the NE230 spectrometer calculated using cross-sections for n-d elastic scattering, the curve does not decrease smoothly with increase in energy, with the smoothness of the curve disrupted below 18 MeV neutron energies. The disruption of the smoothness of the curve may be due to that below 18 MeV all events are regarded as n-d elastic scattering events, which have high counting statistics. However as the energy increase the contribution of deuterons resulting from n-d elastic scattering increase, this decrease the events due n-d elastic scattering, which tend to smoothen the detection curve of the measured efficiency of the NE230 spectrometer. Figure A-3 shows a comparison of the measured detection efficiency of the NE230 spectrometer determined relative to n-p elastic scattering for n-d elastic events and calculated detection efficiency of the NE230 spectrometer using the cross-sections for n-d elastic scattering. There is a good overall agreement between the measured efficiency relative to n-p elastic scattering and calculated using cross-sections for n-d elastic scattering. Below 22 MeV there are some noticeable disagreements, these may be due to n-d event selection in the pulse height spectra measured with the NE230 spectrometer. Also the fraction of recoiling protons (ϕ_{npf}) at this energy range was assigned as 1, this is since almost all to all events at this range are due to recoiling protons from n-d elastic scattering.
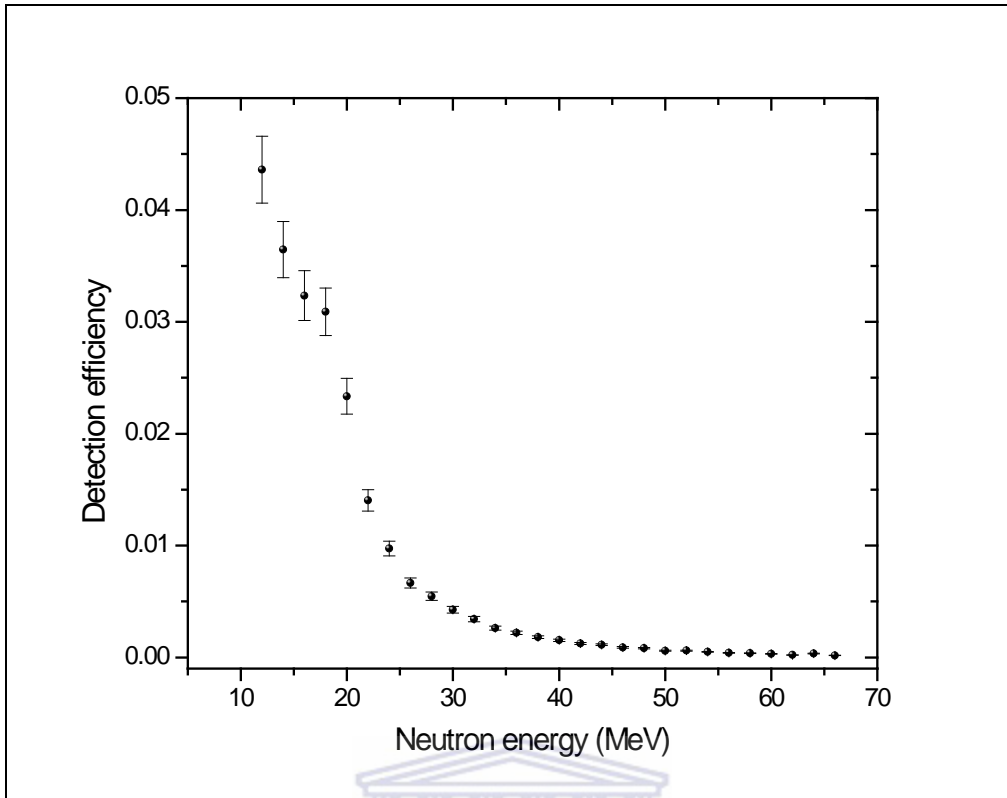
Figure A- 2: *Neutron detection efficiency of the NE230 spectrometer for n-d elastic scattering events as a function of incident neutron energy determined relative to n-p elastic scattering.*
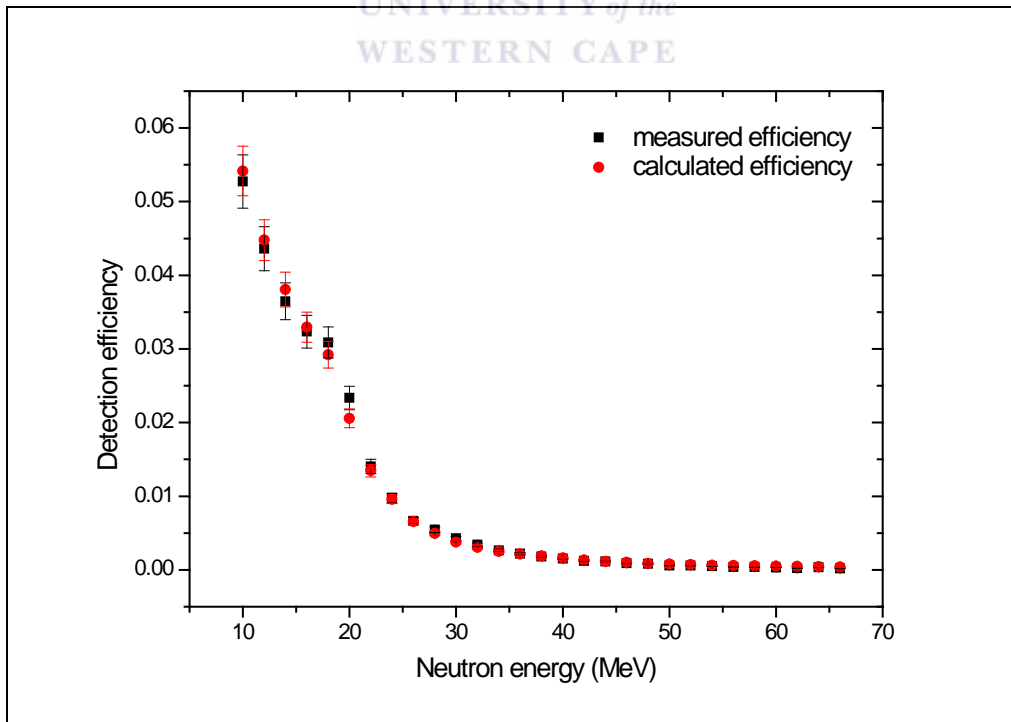
Figure A- 3: *Comparison between detection efficiencies of the NE230 spectrometer calculated using cross-sections for n-d elastic scattering and determined from n-d elastic scattering events relative to n-p elastic scattering.*

APPENDIX B

Calculation of the ratio of the total number of protons or deuterons which recoil directly forward from $^1H(n,n)^1H$/ $^2H(n,n)^2H$ events in a scintillator to the number of such protons or deuterons which do not escape from the detector.

(Reproduced from Buffler and with minor modifications to include recoiling deuterons) [Buffler, 1991]

Consider the case of neutrons incident on a curved surface of either a NE213 or NE230 cylindrical detector (as shown in the figure B-1) of diameters 5 cm and 2.5 cm respectively, with the either detector placed perpendicular to the incident neutrons.
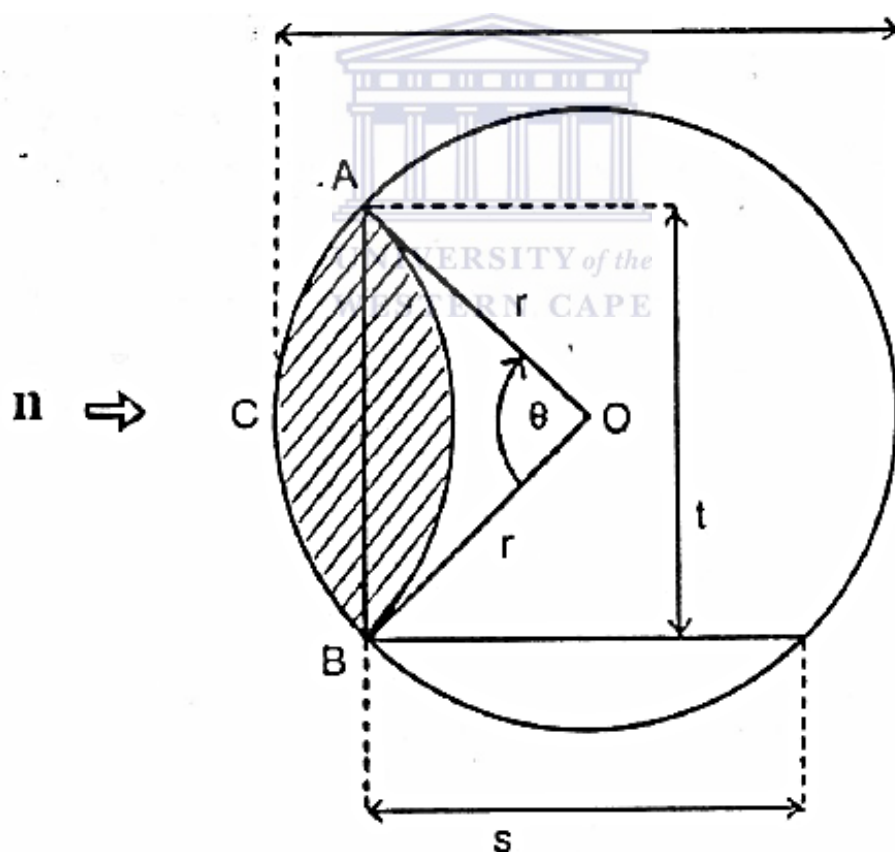
Figure B- 1: *Adopted from the thesis of Buffler, shown is the representation of neutrons incident on a curved surface of a detector (Buffler, 1991).*

The distance line AB is given by:

$$t^2 = 4r^2 - s^2 \tag{B.1}$$

For protons or deuterons recoiling forward only, the ratio:

$$\frac{all\ proton\ or\ deuteron\ events}{proton\ or\ deuteron\ non-escapes} = \frac{\pi r^2}{shaded\ area} \tag{B.2}$$

$$Area\ of\ segment\ OACB = \frac{1}{2}r^2\theta \tag{B.3}$$

Where θ is in radians, by the cosine rule:

$$t^2 = r^2 + r^2 + 2r \times r\cos(\theta) \tag{B.4}$$

Giving:

$$\theta = \cos^{-1}\left(1 - \frac{t^2}{2r^2}\right) = \cos^{-1}\left(\frac{s^2}{2r^2} - 1\right) \tag{B.5}$$

Using eqns. B.3 and B.4 we obtain:

$$Area\ of\ segment\ OACB = \left(\frac{1}{2}r^2\right)\cos^{-1}\left(\frac{\frac{1}{2}s^2}{r^2} - 1\right) \tag{B.6}$$

$$Area\ of\ \Delta AOB = \frac{1}{4}st = \frac{1}{4}s\sqrt{4r^2 - s^2} \tag{B.7}$$

$$shaded\ area = 2\left[\left(\frac{1}{2}r^2\right)\cos^{-1}\left(\frac{s^2}{2r^2} - 1\right) - \frac{1}{4}s\sqrt{4r^2 - s^2}\right] \tag{B.8}$$

This simplifies to:

$$shaded\ area = r^2\cos^{-1}\left(\frac{s^2}{2r^2} - 1\right) - \frac{1}{2}s\sqrt{4r^2 - s^2} \tag{B.9}$$

Then the ratio:

$$\frac{all\ proton\ or\ deuteron\ events}{proton\ or\ deuteron\ non-escapes} = \frac{\pi r^2}{r^2 \cos^{-1}\left(\frac{s^2}{2r^2}-1\right) - \frac{1}{2}s\sqrt{4r^2-s^2}} \qquad \text{(B.10)}$$

APPENDIX C

Non-relativistic kinematics of nuclear reactions and scattering

(Reproduced from Marion and Young [Marion & Young, 1968])
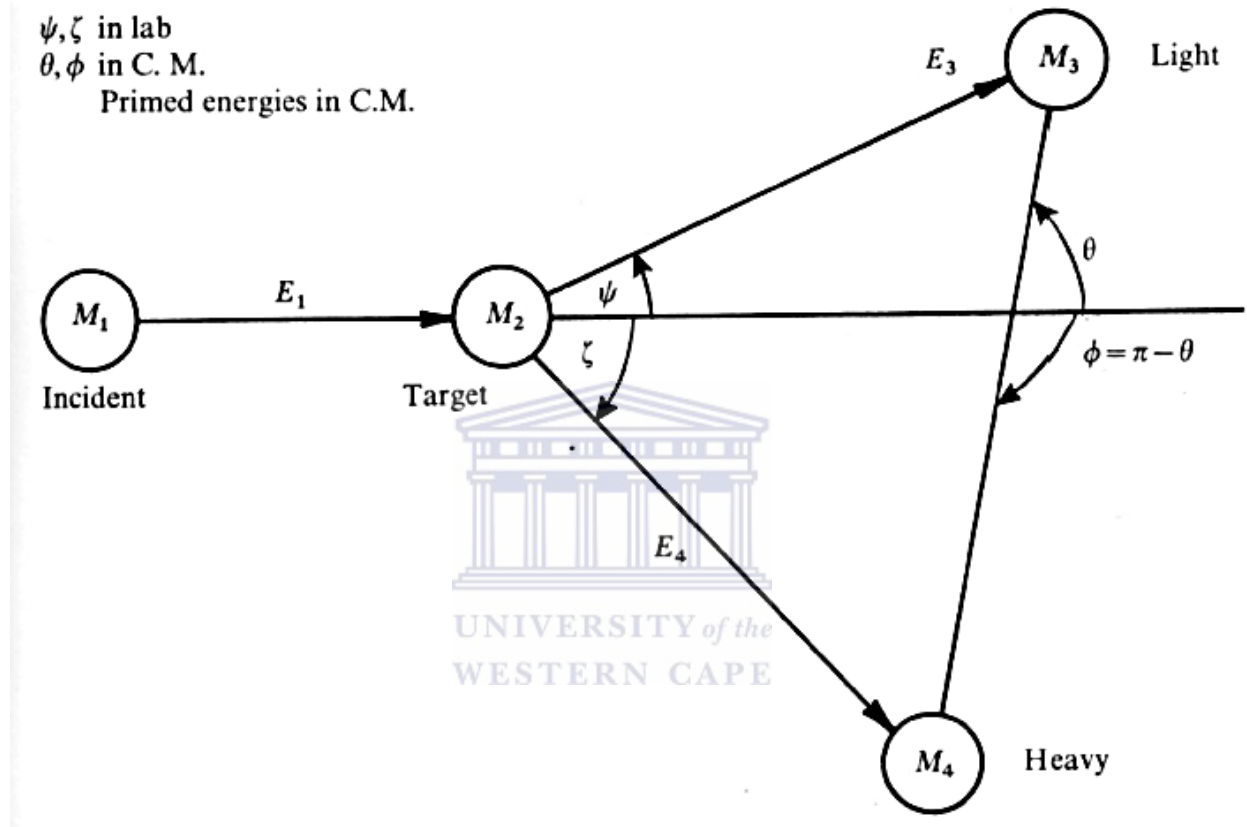
Figure C- 1: Diagram adopted from Marion and Young for nuclear reaction with angles in the laboratory and center of mass frames [Marion & Young, 1968].

The Q-value is given by:

$$5 \qquad Q = \left(M_1 + M_2 - M_3 - M_4\right)c^2$$

(C.1)

Where $M_1, M_2, M_3,$ and M_4 are the rest masses of particles as shown in fig C-1 in MeV/c^2, and c is the speed of light. The kinetic energy in the laboratory (lab) frame is given by:

$$E_T = E_1 + Q = E_3 + E_4 \qquad (C.2)$$

Where $E_1, E_3,$ and E_4 are energies in the lab frame of the incident particle, light, and heavy product particles respectively. We define:

$$A = \frac{M_1 M_2 (E_1/E_T)}{(M_1 + M_2)(M_3 + M_4)} \qquad (C.3)$$

$$B = \frac{M_1 M_3 (E_1/E_T)}{(M_1 + M_2)(M_3 + M_4)} \qquad (C.4)$$

$$C = \frac{M_2 M_3}{(M_1 + M_2)(M_3 + M_4)}\left(1 + \frac{M_1 Q}{M_2 E_T}\right) \qquad (C.5)$$

$$D = \frac{M_2 M_4}{(M_1 + M_2)(M_3 + M_4)}\left(1 + \frac{M_1 Q}{M_2 E_T}\right) \qquad (C.6)$$

$$\textit{Note that } A + B + C + D = 1 \textit{ and } AC = BD \qquad (C.7)$$

The energy of the light product in the centre of mass frame (CM) is given by:

$$\frac{E_3}{E_T} = B + D + 2\left((AC)^{1/2} \cos\theta\right) \qquad (C.8)$$

In the lab frame this becomes:

$$\frac{E_3}{E_T} = B\left[\cos\psi \pm \left(D/B - \sin^2\psi\right)^{1/2}\right]^2 \qquad (C.9)$$

The energy of the heavy product in the CM frame is given by:

$$\frac{E_4}{E_T} = A + C + 2\left((AC)^{1/2} \cos\phi\right) \qquad (C.10)$$

In the lab frame this becomes:

$$\frac{E_4}{E_T} = A\left[\cos\zeta \pm \left(D/B - \sin^2\zeta\right)^{1/2}\right]^2 \qquad (C.11)$$

For elastic scattering
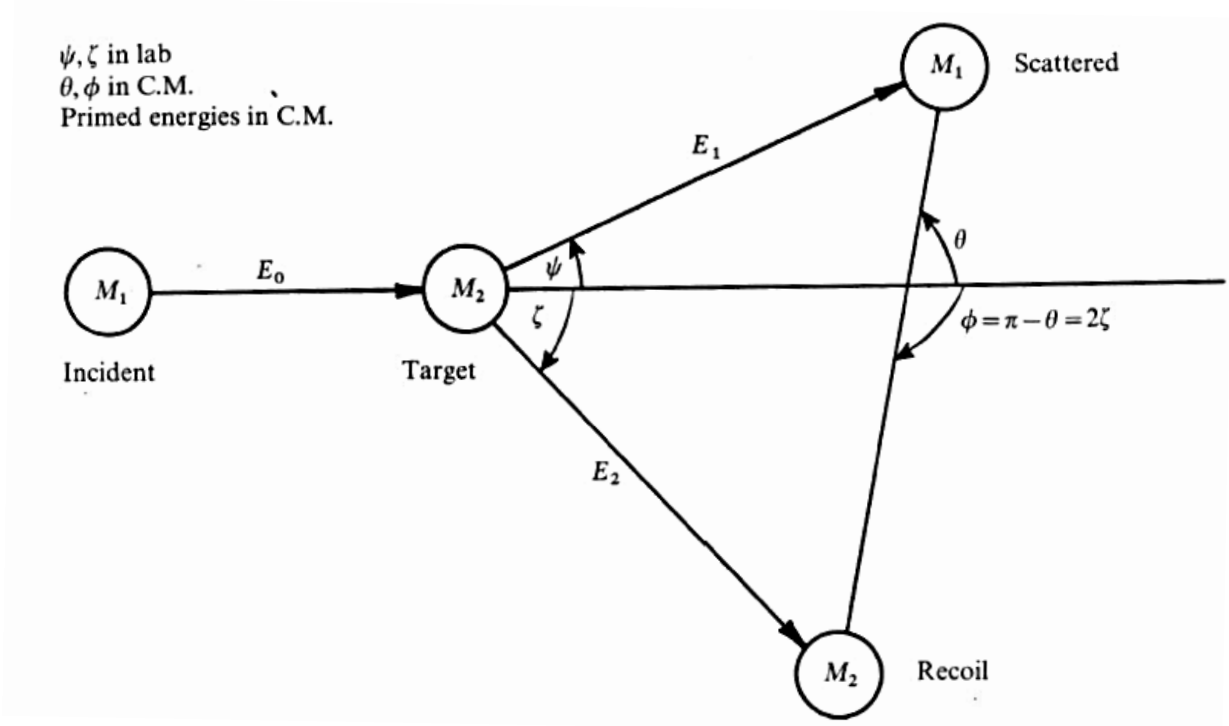
Figure C- 2: *Adopted from Marion and Young is the diagram representing elastic scattering [Marion & Young, 1968].*

For elastic scattering, all energy and angle ratios are independent of energy and reduce to:

$$E_1^{'} = \frac{M_2^2}{(M_1 + M_2)^2} E_0 \qquad (C.12)$$

$$E_2^{'} = \frac{M_1 M_2}{(M_1 + M_2)^2} E_0 \qquad (C.13)$$

Where E_1' and E_2' are in the centre of mass frame (CM). The energy of the scattered particle in the lab frame is given by:

$$\frac{E_1}{E_0} = 1 - \frac{2M_1 M_2}{(M_1 + M_2)^2} (1 - \cos\theta) \qquad (C.14)$$

This becomes:

$$\frac{E_1}{E_0} = \frac{M_1^2}{(M_1 + M_2)^2} \left\{ \cos\psi \pm \left[(M_2 / M_1)^2 - \sin^2\psi \right]^{1/2} \right\}^2 \qquad (C.15)$$

The energy of the recoiling nucleus in the lab frame is given by:

$$\frac{E_1}{E_0} = 1 - \frac{E_1}{E_0} = \frac{4M_1 M_2}{(M_1 + M_2)^2} \cos^2\zeta \qquad where\ \zeta \leq \frac{1}{2}\pi \qquad (C.16)$$

125

REFERENCES

[Adams, 2010] Adams, B. A. S., 2010. *Monte Carlo simulation of the iThemba LABS neutron beam facility,* s.l.: Unpublished.

[Adams, et al., 2010] Adams, B. A. S. et al., 2010. Monte Carlo simulations of the production of neutrons at iThemba LABS. *Radiation Measurements,* Volume 45, pp. 1193-1196.

[Agostinelliae, et al., 2003] Agostinelliae, S. et al., 2003. GEANT4-a simulation toolkit. *Nuclear Instruments and Methods in Physics Research,* Volume A 506, pp. 250-303.

[Alevra, 1999] Alevra, A. V., 1999. Neutron Spectrometry. *Radiation Protection,* 34(3), pp. 305-333.

[Apostolakis, et al., 2009] Apostolakis, J. et al., 2009. Geometry and physics of the Geant4 toolkit for high energy and medium energy applications. *Radiation Physics and Chemistry,* Volume 78, pp. 859-873.

[Baba, 1999] Baba, M. et al., 1999. Characterization of a 40-90 MeV 7-Li(n,p) neutron source at TIARA using a proton recoil telescope and a TOF method. *Nuclear Instruments and Methods in Physics Research,* Volume A 428, pp. 454-465.

[Barry & Kuyatt, 1994] Barry, N. T. & Kuyatt, C. E., 1994. *Guidelines for Evaluating and Expressing the Uncertainty of NIST Measurement Result,* Gaithersburg: National Institute of Standards and Technology.

[Barlett, et al., 2003] Bartlett, D. T. et al., 2003. Concepts and quantities in spectrometry and radiation protection. *Radiation Protection Dosimetry,* 107(1-3), pp. 25-35.

[Becchetti, et al., 2013] Becchetti, F. D., febbraro, M., Torress-Isea, R. & Ojaruega, M., 2013. 252-Cf fission-neutron spectrum using a simplified ToFsetup: An advanced teaching laboratory experiment. *American Journal of Physics,* 81(2), pp. 112-119.

[Benck, et al., 2002] Benck, S. et al., 2002. In-phantom spectra and dose distributions from a high energy neutron therapy beam. *Nuclear Instruments and Methods in Physics Research,* Volume A 476, pp. 127-131.

[Bertl, et al., 1972] Bertl, W., Breunlin, W., Chalipka, A. & Tagesen, S., 1972. Response of the liquid scintillators NE230 to deuterons and NE213 to protons. *Nuclear Instruments and Methods,* Volume 104, pp. 205-207.

[Bevington & Robinson, 2003] Bevington, P. R. & Robinson, K. D., 2003. *Data Reduction and Error Analysis for the Physical Sciences.* 3rd ed. New York: McGraw-Hill.

[Bildstein, et al., 2013] Bildstein, V. et al., 2013. Comparison of deuterated and normal liquid scintillators for fast-neutron detection. *Nuclear Instruments and Methods in Physics Research,* Volume A 729, pp. 188-197.

[Birks, 1964] Birks, J. B., 1964. *The Theory and Practice of Scintillation Counting.* London: Pergamon Press.

[Bohm, 1999] Bohm, T. et al., 1999. Monte Carlo calculations to characterize the source for neutron therapy facility. *Medical Physics,* 26(5), pp. 783-792.

[Brooks, 1979] Brooks, F. D., 1979. Developments of organic scintillators. *Nuclear Instruments and Methods,* Volume 162, pp. 477-505.

[Brooks, et al., 2004] Brooks, F. D. et al., 2004. Measurements of neutron fluence spectra up to 150 Mev using a stacked scintillator neutron spectromenter. *Radiation Protection Dosimentry,* 110(1-4), pp. 151-155.

[Brooks & Klein, 2002] Brooks, F. D. & Klein, H., 2002. Neutron spectrometry-historical review and present status. *Nuclear Instruments and Methods in Physics Research,* Volume A 476, pp. 1-11.

[Buffler, 1991] Buffler, A., 1991. *The response of organic scintillators to neutrons of energy 14-63 MeV,* s.l.: Unpublished.

[Buffler, et al., 2002] Buffler, A. et al., 2002. Measurements of neutron energy spectra from 15 to 150 MeV using stacked liquid scintillator. *Nuclear Instruments and Methods in Physics Research,* Volume A 476, pp. 181-185.

[Cecil, et al., 1979] Cecil, R. A., Anderson, B. D. & Madey, R., 1979. Improved predictions of neutron detection efficiency for hydrocarbon scintillators from 1 MeV to about 300 MeV. *Nuclear Instruments and Methods,* Volume 161, pp. 439-447.

[Copley & Udovic, 1993] Copley, J. R. D. & Udovic, T. J., 1993. Neutron ToFspectroscopy. *Journal of Research of the National Institute of Standards and Technology,* 98(1), pp. 71-87.

[Cornelius & Rosenfeld, 2004] Cornelius, I. & Rosenfeld, A. B., 2004. Verification of Monte Carlo calculations in fast neutron therapy using silicon microdosimetry. *IEEE Transactions on Nuclear Science,* 51(3), pp. 873-877.

[Crane & Baker, 1991] Crane, T. W. & Baker, M. P., 1991. *Neutron Detectors-Los Alamos National Laboratory.* [Online] Available at: www.lanl.gov/orgs/n/n1/panda/00326408.pdf [Accessed 22 February 2013].

[Craun & Smith, 1970] Craun, R. L. & Smith, D. L., 1970. Analysis of response data for several organic scintillators. *Nuclear Instruments and Methods,* Volume 80, pp. 239-244.

[Crout, et al., 1989] Crout, N. M. J., Fletcher, J. G. & Scott, M., 1989. Calibration of an NE213 scintillator up to 60 MeV for in situ spectrometry in a neutron cancer therapy facility. *Nuclear Instruments and Methods in Physics Research,* Volume A 277, pp. 664-668.

[Dickens, 1988] Dickens, J. K., 1988. *SCINFUL: A Monte Carlo Based Computer Program to Determine a Scintillator Full Energy Response to Neutron Detection for En Between 0.1*

and 80 MeV: User's Manual and FORTRAN Program listing, Ork Ridge: Ork Ridge National Laboratory.

[Dickens, et al., 1985] Dickens, J. K. et al., 1985. *An NE213-Scintillator-Based Neutron detection System for Diagonostic Measurements of Energy Spectra for Neutrons Having Energies greater than 0.8 MeV Created During Plasma Operations at the Princeton Tokamak Fusion Test Reactor,* Oak Ridge: Oak Ridge National Laboratory.

[EJ-301] EJ-301,n.d. *EJ-301.* [Online] Available at :http://www.eljentechnology.com/index.php/products/liquid-scintillators/71-ej-301 [Accessed 18 October 2013].

[EJ-315] EJ-315,n.d. *EJ-315.* [Online] Available at: http://www.eljentechnology.com/index.php/products/liquid-scintillators/75-ej-315 [Accessed 18 October 2013].

[ENDF] ENDF,n.d. *ENDF Data.* [Online] Available at: https://t2.lanl.gov/nis/data/endf/index.html [Accessed 8 August 2013].

[Gagnon-Moisan, et al., 2012] Gagnon-Moisan, F., Reginatto, M. & Zimbal, A., 2012. *Results for the response function determination of Compact Neutron Spectrometer.* Ein Gedi, IOP publishing for SISSA medilab.

[Graham, et al., 2012] Graham, J. et al., 2012. Neutron flux characterization techniques for radiation effects studies. *Journal of Radioanalytical and Nuclear Chemistry,* Volume 291, pp. 503-507.

[GUM, 2008] GUM, 2008. *Evaluations of measurements-Guide to the expression of uncertainty in measurement,* s.l.: s.n.

[Herbert, 2009] Herbert, M., 2009. *Determination of energy spectra inside a water phantom irradiated by neutrons of energy up to 64 MeV,* s.l.: Unpublished.

[Herbert, 2014] Herbert, M., 2014. Measurements and simulation of neutron beam fluence energy distrubutions at the neutron ToFfacility of iThemba LABS. *Radiation Protection Dosimetry,* pp. 1-6.

[Herbert, et al., 2014] Herbert, M. et al., 2014. Measurements and simulations of scattered neutrons in a water phantom. *Progress in Nuclear Science and Technology,* Volume 4, pp. 643-647.

[Herbert, et al., 2007] Herbert, M. S. et al., 2007. Determination of neutron energy spectra inside a water phantom irradiated by 64 Mev neutrons. *Radiation Protection Dosimetry,* 126(1-4), pp. 346-349.

[Howard, et al., 1974] Howard, V. J. et al., 1974. Differential cross sections for np and nd elastic scattering near 130 MeV. *Nuclear Physics,* Volume A 218, pp. 140-150.

[Hughes, et al., 1997] Hughes, H. G., Prael, R. E. & Little, R. C., 1997. *MCNPX-THE LAHET/MCNP code merger X-Division Research Note,* s.l.: Los Alamos National Laboratory.

[Karlsson, 1997] Karlsson, M., 1997. *Absolute efficiency calirbration of a NE213 liquid scintillator using a 252-Cf source,* Sweden: s.n.

[Kinnison, 2003] Kinnison, J. D., Maurer, R. H., Roth, D. R. & Haight, R. C., 2003. High-Energy Neutron Spectroscopy with Thick Silicon Detectors. *Radiation Research,* Volume 159, pp. 154-160.

[Klein, 2003] Klein, H., 2003. Neutron spectrometry in mixed fields: NE213/BC501A Liquid scintillation spectrometers. *Radiation Protection Dosimetry,* 107(1-3), pp. 95-109.

[Klein & Brooks, 2006] Klein, H. & Brooks, F. D., 2006. *Scintillation detectors for fast neutrons.* Cape Town, Proceedings of Science.

[Knoll, 2000] Knoll, G. F., 2000. *Radiation detection and Measurement.* 3rd ed. New York: John Wiley & Sons.

[Koohi-Fayegh, et al., 2000] Koohi-Fayegh, R., H, A. M., Green, S. & Scott, M. C., 2000. Neutron spectrum measurements from 1-16 MeV in beryllium assemblies with a central D-T neutron source. *Annals of Nuclear Energy,* Volume 27, pp. 959-967.

[Laustriat, 1968] Laustriat, G., 1968. *the luminescence decay of organic scintillators.* New York, Gordon and Beach, pp. 127-145.

[Lee & Yang, 1964] Lee, Y. & Yang, Y., 1964. A fast neutron Spectrometer by the ToFMethod. *Chinese Journal of Physics,* 2(2), pp. 57-62.

[Leo, 1987] Leo, W. R., 1987. *Techniques for Nuclear and Particle Physics Experiments.* Berlin: Springer.

[Makupula, 2003] Makupula, S. A., 2003. *Measurements of neutron fluence at En=20-100 MeV using a stacked scintillator spectrometer,* s.l.: Unpublished.

[Marion & Young, 1968] Marion, J. & Young, F., 1968. *Nuclear reaction analysis.* Amsterdam: North-Holland publishing CO.

[Matze, 2003] Matzke, M., 2003. Unfolding Procedures. *Radiation Protection Dosimetry,* 107(1-3), pp. 155-174.

[Meigo, 1997] Meigo, S., 1997. Measurements of the response function and the detection efficiency of an NE213 scintillator for neutrons between 20 and 65 Mev. *Nuclear Instruments and Methods in Physics Research ,* Volume A 401, pp. 365-378.

[Mosconi, et al., 2010] Mosconi, M. et al., 2010. Characterisation oh the high energy neutron beam at iThemba LABS. *Radiation Measurements,* Volume 45, pp. 1342-1345.

[Nagadi & Naqvi, 1998] Nagadi, M. M. & Naqvi, A. A., 1998. Measurements of Deuteron and Proton Response Function of Deuterated-cyclohexane and Cyclohexane Scintillators. *Applied Radiation and Isotopes,* 49(4), pp. 397-403.

[Negoita, 2004] Negoita, C. C., 2004. *Measurements og Neutron Flux Spectra in a Tungsten Bencmark by neutron Foil Activation Method,* s.l.: s.n.

[NNDC] NNDC,n.d. *National Nuclear Data Center.* [Online] Available at: http://www.nndc.bnl.gov/ [Accessed 20 May 2013].

[Ojaruega, 2009] Ojaruega, M. I., 2009. *Fast Neutron Measurements using Deuterated Liquid Scintillator,* Michigan: Ojaruega, M I.

[Pauletta & Brooks, 1975] Pauletta G, Brooks, F. D., 1975. cross sections for the n+d breakup reactions. *Nuclear Physics,* Volume A 255, pp. 267-274.

[Pauletta, 1973] Pauletta, G., 1973. *The neutron-deuteron breakup cross section between 8 and 22 MeV,* s.l.: Unpublished.

[Peurung, 2000] Peurung, A. J., 2000. Recent developments in neutron detection. *Nuclear Instruments and Methods in Physics Research,* Volume A 443, pp. 400-415.

[Roberts, et al., 1990] Roberts, D. A. et al., 1990. Energy and flux limits of cold-fusion neutrons using a deuterated liquid scintillator. *Physical Review,* 42(5), pp. 1809-1813.

[Rose, 1991] Rose, P. F., 1991. *ENDF-201 ENDF/B-VII sammary documantation,* New York: Brookhaven National Laboratory.

[Sanami, et al., 2009] Sanami, T. et al., 2009. A Bragg curve counter with an internal production target for the measurement of the double-differential cross-section of fragment production induced by neutrons as energies of tens of MeV. *Nuclear Instruments and Methods in Physics Research,* Volume A 610, pp. 660-668.

[Satoh, et al., 2011] Satoh, D. et al., 2011. Experimental Method for Neutron Elastic Scattering Cross-section Measurement in Intermediate Energy Region at RCNP. *Progress in Nuclear Science and Technology,* Volume 1, pp. 20-23.

[Sisterson, et al., 2005] Sisterson, J. M. et al., 2005. Cross-section measurements for the neutron-induced reactions in copper at neutron energies of 70.7 and 110.8 MeV. *Nuclear Instruments and Methods in Physics Research ,* 240 (B), pp. 617-624.

[Stepan & Bull, 2014] Stepan, G. M. & Bull, J. S., 2014. MCNP6 Simulation of Quasi-Monoenergetic 7-Li(p,n) Neutron Sources below 150 MeV. *Nuclear Data Sheets,* Volume 118, pp. 323-325.

[Tajik, et al., 2013] Tajik, M., Ghal-Eh, N., Etaati, G. R. & Afarideh, H., 2013. Modeling NE213 scintillator response to neutrons using MCNPX-PHOTRACK hybrid code. *Nuclear Instruments and Methods in Physics Research,* Volume A 704, pp. 104-110.

[Takada, et al., 2011] Takada, M., Yajima, K., Kamada, H. & Nakamura, T., 2011. Simulated Neutron Response Functions of Phoswich-Type Neutron Detector and Thin Organic Liquid Scintillator. *Progress in Nuclear and Technology,* Volume 2, pp. 274-279.

[Takeda, et al., 2000] Takeda, N. et al., 2000. *Response Function of a NE213 Liquid Scintillation Retector Simulated by EGS4/PRESTA Code for a Collimated gamma-ray Beam.* Japan, s.n., pp. 168-175.

[Taniguchi, et al., 2003] Taniguchi, S. et al., 2003. Neutron energy and ToFbehind the lateral shield of a high energy electron accelerator beam dump. Part I: Measurements. *Nuclear Instruments and Methods in Physics research,* Volume A 503, pp. 595-605.

[Travernier, 2010] Tavernier, S., 2010. *Experimental Techniques in nuclear and Particle Physics.* Berlin: Spinger.

[Thomas, et al., 2011] Thomas, D. J., Nolte, R. & Gressier, V., 2011. What is neutron metrology and why is it needed. *Metrologia,* Volume 48, pp. S225-S238.

[Verbinski, et al., 1968] Verbinski, V. V. et al., 1968. Calibration of an organic scintillator for neutron spectrometry. *Nuclear Instruments and Methods,* Volume 65, pp. 8-25.

[Zimbal, et al., 2006] Zimbal, A. et al., 2006. *High resolution neutron spectrometry with liquid scintillation detectors for fusion applications.* Cape Town, Proceedings of Science.